X-ray Observations of Accreting Magnetic White Dwarfs

質量降着を受ける強磁場白色矮星のX線観測

東京大学大学院 理学系研究科 物理学専攻 博士課程

石田 学

X-ray Observations of
Accreting Magnetic White Dwarfs

Manabu ISHIDA

Department of Physics, Faculty of Science, University of Tokyo

7-3-1, Hongo, Bunkyo-ku, Tokyo 113, Japan

A thesis submitted in partial fulfillment
of the requirements for the degree of
DOCTOR OF SCIENCE (Physics)
at the
UNIVERSITY OF TOKYO

December, 1991

Contents

i

Chapter 1

Introduction

Cataclysmic Variables (CVs) are binary systems composed of a white dwarf and a late type main sequence (typically M spectral type) star. Mass accretion onto the white dwarf via Roche lobe overflow of the secondary star is the main source of the strong radiation in CVs. CVs have been observed in quite a wide energy band, from radio to hard X-rays, showing characteristics of "cataclysmic intensity variation" typically over several orders of magnitude. A new subclass, Magnetized Cataclysmic Variables (MCVs) has been widely recognized since S. Tapia (1977) discovered polarized optical emission from AM Herculis. From the polarization in the optical band, he estimated that the white dwarf in the system has a strong magnetic field of $\sim 10^8$ gauss, although this value was later found to be considerable overestimation.

X-ray observational data have been accumulated mainly by the three satellites, *HEAO-1*, *Einstein* and *EXOSAT*. These data indicate that MCVs should be further divided into two subgroups, polars and intermediate polars. Polars, mainly soft X-ray sources, show strong optical polarization, and the white dwarf rotation period and the orbital period are synchronized due to the strong magnetic field of the white dwarf. Intermediate polars, mainly hard X-ray sources, on the other hand, show no optical polarization and the rotatoinal period is always shorter than the orbital period. Observations made with these satellites supplied us with useful clues to understanding the nature of X-ray emission, origin of spin modulations, and others in MCVs.

Ginga, the third Japanese X-ray astronomy satellite, has observed a number of MCVs since its launch on February 5. 1987. The Large Area proportional Counter (LAC) on board the *Ginga* satellite has high sensitivity up to ~ 35 keV. Sensitivity up to around 40 keV is needed to investigate the hard X-ray emission from MCVs since it corresponds roughly to the average gravitational energy per particle of accreting matter on the white dwarf surface. As a matter of fact, a substantial fraction of total accretion luminosity is radiated in this hard X-ray band. In the past, only the *HEAO*-A2 and A4 experiments could observe X-rays up to this energy (2–60 keV and 15–150 keV, respectively). Their sensitivity were, however, substantially lower than that of *Ginga*. Observations with the previous Japanese satellites, *Hakucho* and *Tenma*, were difficult due to their energy coverage. Although *Einstein* and

1

EXOSAT carried instruments more sensitive, their energy range was limited up to ~4 keV and ~10 keV, respectively. *Ginga*, therefore, provides a chance of systematic investigation of hard X-ray emission from MCVs with a much larger number of samples and with a significantly improved accuracy.

One of the most important characteristics of MCVs seen in hard X-rays is that the light curve is strongly modulated at the rotatinal period of the white dwarf due to the funneling of the accreting matter to the magnetic poles. The origin of this spin modulation has generally been attributed to the occultation of the hard X-ray emission region by the white dwarf through its rotation. Recent optical observations of intermediate polars, however, suggest that the absorption and/or scattering by the accreting matter also plays an important role on this. It is, thus, highly important to observe MCVs in the energy range above ~10 keV in which the absorption effect is mostly negligible, in order to distinguish between the occultation and the absorption effect. Owing to its high sensitivity and wide energy range, *Ginga* is expected to give a definitive answer to this probrem.

Another important observational characteristic of MCVs is that their X-ray spectra usually involve a very hard component. A number of theoretical works have so far predicted that a standing shock is formed in the accretion stream near the white dwarf surface. The accreting matter is abruptly heated at the shock front, forms plasma with a high temperature comparable to the gravitational potential energy (= a few tens of keV), and emits hard X-rays via optically thin thermal bremsstrahlung. In a few bright MCVs, observed spectra have actually been fitted well with thermal bremsstrahlung model. *Ginga* is able to examine this theoretical prediction for a large number of sources with a much improved accuracy, and advance our knowledge on the X-ray emission mechanism of MCVs. The other important prediction of the theory is that the shock-heated plasma will cool down via radiation, thermal conduction, *etc.* as it descends the accretion column down to the white dwarf surface. This phenomenon is expected to be detectable with *Ginga* for a few bright MCVs during the ingress and egress of the occultation of the emission region with the white dwarf.

This thesis intends to improve our understanding of MCVs through hard X-ray observations made with *Ginga*. Chapter 2 reviews the observational and theoretical work on MCVs made so far. Chapter 3 describes the instrumentation on board the *Ginga* satellite. The observed targets are listed up in Chapter 4, together with a description about how observations were performed. Chapter 5 is dedicated to the description of data analysis and the results derived. Through the analysis, it is clarified that the cause of the spin modulation is considerablly different for polars and intermediate polars. Spectra of all the sources used in this thesis are well explained basically by optically thin thermal bremsstrahlung. Most of the observed spectra of MCVs undergo considerable amount of absorption, and this absorption cannot be explained by a single column density. Moreover, it is discovered that temperature of the thermal bremsstrahlung varies with the spin phase of the white dwarf in AM Herculis. Based on these results, physical properties of the shock-heated plasma and the environment around it is discussed in Chapter 6. Finally, conclusions are summarized in Chapter 7.

Chapter 2

Reviews

2.1   Overview

Cataclysmic variables are binaries of a white dwarf and a late type main sequence star, and radiations from CVs are driven mainly by the mass accretion from the secondary[1] via Roche lobe overflow. In 1976, Tapia found circularly-polarized optical emission from AM Herculis which varied at a period of ~3.1h. The degree of polarization is an order of magnitude higher than that of any other cerestial objects ever observed. Figure 2.1 shows the variation of optical circular and linear polarization of AM Herculis. Such a strongly polarized light in optical wave band was thought at that time to be due to cyclotron radiation from the magnetic polar region of the white dwarf with a surface magnetic field strength of $\sim 10^8$ gauss. This idea is qualitatively true, although the magnetic field strength is later found to be of order 10^7G. Just after the discovery, three more stars which showed the same characteristics were found— AN UMa (Krzeminski & Serkowski 1977), VV Pup (Tapia 1977) and EF Eri (Tapia 1979). Since then, a subclass called "Magnetized Cataclysmic Variables (MCVs)" has generally been recognized, and those which show strong polarization in optical wave band are classified as "polars" or "AM Her type sources". Table 2.1 shows the list of polars now catalogued. A remarkable property of the polars, besides the strong optical polarization, is that the magnetic field of the white dwarf is so strong ($B \sim 10^7$ gauss; see subsection 2.2.4) that the rotational period of the white dwarf (P_S) and the orbital period (P_{orb}) of the binary system are synchronized, presumably through magnetic coupling between the two stellar components.

In addition to the polars, intermediate polars are now regarded as another subclass of MCVs. The white dwarf in the intermediate polar systems rotates faster than the binary revolution ($P_S < P_{orb}$). Unlike polars, intermediate polars do not show polarization in optical wave band. Nevertheless intermediate polars are believed to include a magnetized white dwarf since *EXOSAT* found a dozen of intermediate polars which emit hard X-rays modulated at the white dwarf rotational period (Norton & Watson 1989 and references therein). This has been interpreted as due to funneling of accreting matter near the white

---

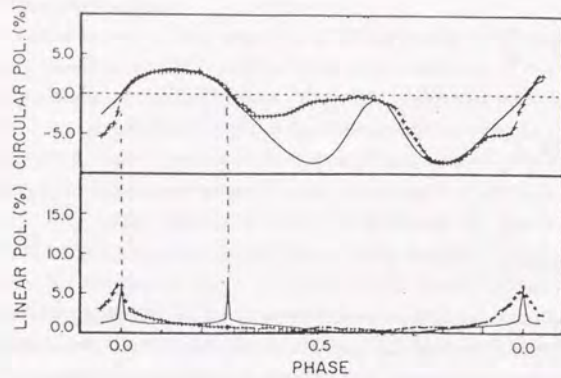[1]In this thesis, we call the main sequence star a secondary star.

Figure 2.1:
Circular and linear polarization of AM Her in optical wave band as a function of spin phase (from Tapia 1977). The phase origin is set at the time when the degree of linear polarization is maximum.

dwarf. Table 2.2 lists intermediate polars now catalogued.

Polars and intermediate polars are usually referred to as "AM Her" stars and "DQ Her" stars, respectively. Some intermediate polars (the last three sources in table 2.2), however, show appreciably different characteristics in comparison with the other intermediate polars. First, these three sources are not the hard X-ray sources. Secondly, the rotational period of the white dwarf (less than 100s) is shorter than the others by an order of magnitude. With these reasons, the sources with $P_S < 100$s are sometimes classified as "DQ Her" stars, and are discriminated from intermediate polars in which $P_S > 100$s, although this classification is not completely established. We do not deal with "DQ Her" stars ($P_S < 100$s) in this thesis since they are not the hard X-ray sources.

Table 2.1: Basic properties of polars

Name of Sources	Period (h)	Spectral type[a] of Secondary	distance[b] (pc)	B_Z [c] (MG)	B_C [d] (MG)	i [e] (°)	β [e] (°)
EF Eri	1.350 [1]		≥89			58±12	27±18
DP Leo (1E1114+182)	1.497 [2]		≥380 [18]		44.0±1.4 [27]	76±10	103±5
VV Pup	1.674 [3]	M4	145		31.7 [28,29]	76±6	152±6
E1405-451 (V834 Cen)	1.692 [4]	M6.5	86, 50-150	22±2 [21]		45±9	25±5
Grus V1	1.81 [5]						
MR Ser (PG1550+191)	1.893 [6]	M5-6	112		24.6±0.6 [27]	43±5	38±5
BL Hyi (H0139-68)	1.894 [7]	M3-4	128	30 [22]		70±10	153±10
CW1103-254 (ST LMi)	1.898 [8]	M5-6	128	19 [23]		64±5	141±4
EK UMa (1E1048+542)	1.908 [9]				47±3 [30]	56±19	56±19
AN UMa	1.914 [10]		≥270		35.8±1.0 [27]	65±5	20±5
EXO 0234-5232 (WW Hor)	1.925 [11]	M6	500				
EXO 0333-2554 (UZ For)	2.109 [12]	M4.5	250		56 [31,32]		
AM Her	3.094 [13]	M4.5	75	13 [24,25,26]		30±5	61±5
H0538+608 (BY Cam)	3.322 [14]				40.8±1.5 [27]		
V1500 Sgr	3.351 [15]		1200±200 [19]				
E2003+225 (QQ Vul)	3.708 [16]	M2-4	≥400 [20]			60±14	19±9
EXO 0329-2606	3.806 [17]	M4.5					

a: see Ritter (1990) and references therein. b: Calculated with eq.3(a) of Warner (1987) and K-magnitude unless indicated. c: Magnetic field strength with Zeeman splitting. d: Magnetic field strength with cyclotron line emissions. e: inclination of the system (i), and collatitude of the magnetic pole (β); Cropper (1988b), Meggitt & Wickramasinghe (1989).

References: [1] Boley, private communication in Griffiths *et al.* (1979); [2] Biermann *et al.* (1982); [3] van Gent (1931); [4] Mason *et al.* (1982); [5] Tuohy *et al.* (1987); [6] Stockman *et al.* (1981); [7] Cropprer (1982); [8] Stockman *et al.* (1982); [9] Morris *et al.* (1987); [10] Mumford (1976); [11] Beuermann *et al.* (1986); [12] Giommi *et al.* (1987); [13] Tapia (1976); [14] Bradt *et al.* (1988); [15] Patterson (1979); [16] Nousek *et al.* (1982); [17] Beuermann *et al.* (1988a); [18] Biermann *et al.* (1985); [19] Lance *et al.* (1988); [20] Mukai *et al.* (1988); [21] Beuermann *et al.* (1989); [22] Wickramasinghe *et al.* (1984); [23] Schmidt *et al.* (1983); [24] Schmidt *et al.* (1981); [25] Latham *et al.* (1981); [26] Wickramasinghe & Martin (1985); [27] Cropper *et al.* (1988); [28] Wickramasinghe & Meggitt (1982); [29] Barrett & Chanmugam (1985); [30] Cropper *et al.* (1989); [31] Ferrario *et al.* (1988); [32] Beuermann *et al.* (1988).

Table 2.2: Basic properties of intermediate polars and DQ Her stars

Name of	Period		Spectral type [a]	distance
Sources	Rotational (sec)	Orbital (h)	of Secondary	(pc)
SW UMa	954	1.364		140
	[1]	[1]		[22]
EX Hya	4021.62	1.638	M5.5	76-190, $\geq$60, $\geq$130
	[2]	[2]		[23], [24], [25]
3A0729+103	913.49	3.235		800
(BG CMi)	[3]	[3]		[26]
V1223 Sgr	745.8	3.366		600±60
	[4]	[15]		[27]
AO Psc	805.20	3.591		100-250, $\geq$320
(H2252-035)	[5]	[16]		[28], [29]
FO Aqr	1254.45	4.849		$\geq$640, $\geq$200
(H2215-086)	[6]	[17]		[17], [30]
KO Vel	4086	4.94		
(1E1013-477)	[7]	[7]		
TV Col	1911	5.487	K1-5	160, 500
(2A0526-328)	[8]	[18]		[31], [32]
TX Col	1910.9	5.718		180^{+180}_{-90}
(H0542-407)	[9]	[9]		[33]
TW Pic	7560	6.5		
(H0534-581)	[7]	[7]		
GK Per	351.34	47.923	K0	525
	[10]	[19]		[34]
RE0751+14	833.4			
	[11]			
DQ Her	71.0745	4.647	M3	400±100
	[12]	[12]		[35]
V533 Her	63.63	5.035		680±250
	[13]	[20]		[34]
AE Aqr	33.06	9.880	K5	150, 53±25, 70, $\geq$90
	[14]	[21]		[14], [36], [37], [38]

a: Ritter (1990) and references therein.

References: [1] Shafter *et al.* (1986); [2] Gilliland *et al.* (1982); [3] McHardy *et al.* (1984); [4] Osborne *et al.* (1985); [5] Warner & O'Donoghue (1980); [6] Shafter & Targon (1982); [7] Ritter (1990); [8] Shrijver *et al.* (1987); [9] Buckley & Tuohy (1987); [10] Watson *et al.* (1986); [11] this volumn; [12] Walker (1956); [13] Patterson (1979a); [14] Patterson (1979b); [15] Warner & Cropper (1984); [16] Patterson & Price (1980); [17] Osborne & Mukai (1988); [18] Hutchings *et al.* (1981); [19] Crampton *et al.* (1983); [20] Hutchings (1987); [21] Payne-Gaposhkin (1969); [22] Patterson (1984); [23] Sherrington *et al.* (1980); [24] Wade (1982); [25] Berriman *et al.* (1985); [26] McCardy *et al.* (1986); [27] Bonnet-Bidaud *et al.* (1982); [28] Hassall *et al.* (1981); [29] Berriman (1987); [30] Berriman *et al.* (1985); [31] Patterson (1984); [32] Bonnet-Bidaud *et al.* (1985); [33] Buckley & Tuohy (1987); [34] Duerbeck (1981); [35] Young & Schneider (1981); [36] Berriman (1987); [37] Wade (1982); [38] Berriman *et al.* (1985).

2.2   Components, Sizes and Structures of MCV Systems

2.2.1   Mass of the Secondary

The secondary star in CV fills its Roche lobe. In this case, a well-known relation between the orbital period and mean density of the lobe-filling star is derived with the aid of Kepler's third law and the approximate formula for the radius of Roche lobe. Kepler's third law is expressed as

$$\left(\frac{2\pi}{P_{orb}}\right)^2 = \frac{G(M_1 + M_2)}{a^3},\tag{2.1}$$

where M_1 and M_2 are the masses of the primary and the secondary stars, and a means the orbital separation which is

$$a = 5.6 \times 10^{10} \left(\frac{M_1 + M_2}{M_\odot}\right)^{1/3} \left(\frac{P_{orb}}{2hr}\right)^{2/3}.\tag{2.2}$$

On the other hand, the approximate formula for the radius of Roche lobe R_L is

$$\frac{R_L}{a} = \frac{2}{3^{4/3}} \left(\frac{M_2}{M_1 + M_2}\right)^{1/3}\tag{2.3}$$

(Paczyński 1971). Combining these eqs.(2.1) and (2.3) with setting $R_L = R_2$ to eliminate a, we obtain

$$\frac{243\pi}{8G} \frac{1}{P_{orb}^2} = \bar{\rho}_2,\tag{2.4}$$

where $\bar{\rho}_2$ represents the mean density of the secondary star. We are thus able to calculate the mass of the secondary star assuming an appropriate mass-radius relation. Adopting an empirical mass-radius relation for main-sequence stars derived by Patterson (1984);

$$\frac{R}{R_\odot} = \left(\frac{M}{M_\odot}\right)^{0.88} (0.1 \leq \frac{M}{M_\odot} \leq 0.8),\tag{2.5}$$

the mass of the secondary is calculated as

$$M_2 = 0.07 M_\odot \left(\frac{P_{orb}}{1hr}\right)^{1.22}.\tag{2.6}$$

From this equation, we see that the mass of the secondary star in EF Eri, whose orbital period is the shortest, is only $0.10 M_\odot$ and that in TW Pic, whose orbital period is the longest, is $0.68 M_\odot$. As none of ~30 MCVs contains a secondary star with the mass less than the lower mass limit for hydrogen burning stars $(0.08 M_\odot)$, the secondary star is probably a low mass main-sequence star. This is verified by measuring the spectral type of the secondary stars (Mukai & Charles 1986). The only exception is GK Per whose orbital period is ~48h, although it contains K spectral type star. The secondary in GK Per is now believed to be a rather evolved star —a (sub)giant.

2.2.2 Mass of the White Dwarf

Determination of the white dwarf mass is more difficult since it does not fill the Roche lobe. Here we briefly describe recent developments in this field.

So-called mass function of the secondary, f, is expressed as

$$f(M_1, M_2, i) = \frac{(M_1 \sin i)^3}{(M_1 + M_2)^2} = \frac{P_{orb}K^3}{2\pi G}, \tag{2.7}$$

where i is the inclination of the binary system defined as the angle between the axis of the orbital plane and the line of sight, and K is the orbital velocity of the secondary. Notice that the right hand side of this equation is written only with the observable quantities. Once we know i, M_2, and K, we can estimate the mass of the white dwarf, M, from the orbital period P_{orb} which is obtained relatively easily from optical observations.

As will be described in subsection 2.4.4, the optical spectra of MCVs are characterized by strong hydrogen and singly-ionized helium lines. Some of them originate from the X-ray illuminated face of the secondary. Therefore, the orbital velocity of the secondary is estimated from the Doppler velocity measurements of them. As will also be mentioned in subsection 2.2.5, the inclination angle of the system can be estimated with optical polarimetry for polars. Finally, the mass of the secondary can also be obtained with spectral type measurements of the secondary. With these methods, Mukai & Charles (1987) derived mass of the white dwarf in four polar systems, MR Ser ($0.66M_\odot$), ST LMi ($0.38M_\odot$), AM Her ($0.99M_\odot$) and QQ Vul ($0.58M_\odot$). The error associated with these mass determination is $\sim 0.2M_\odot$, and comes mainly from determination of i.

2.2.3 Accretion Disk

Since the accreting matter from the secondary has appreciable angular momentum, it forms an accretion disk around the primary in non-magnetized CVs. The disk is believed to reach the surface of the primary, and so-called boundary layer is formed in which accreting matter is decelerated to the surface angular velocity of the primary and heated via shear viscosity. In MCVs, on the other hand, the magnetic field controls the mass flow from the secondary, so that the accretion disk ends up far above the surface of the primary even if it is formed.

The magnetic pressure is defined as

$$P_{mag} = \frac{B^2}{8\pi}.$$

The magnetic field starts to control accreting matter at the radius defined by the following equation.

$$P_{mag} = \rho v^2. \tag{2.8}$$

Here ρ and v are the mass density and the velocity of the accretion flow. Assuming that the field is dipolar ($B = \mu/r^3$) and the mass accretion occurs in a spherically-symmetric

manner, we obtain

$$r_A = 2.7 \times 10^{10} \left(\frac{M}{M_\odot}\right)^{-1/7} \left(\frac{\mu}{10^{33}\mathrm{G\,cm^3}}\right)^{4/7} \left(\frac{\dot{M}}{10^{16}\mathrm{g\,s^{-1}}}\right)^{-2/7}, \tag{2.9}$$

where r_A is so-called Alfvén radius. Here we have assumed spherically-symmetric mass accretion onto the primary. This simplification is permissible for a rough order estimation of the Alfvén radius because of the strong dependence of P_{mag} on r ($P_{mag} \propto r^{-6}$). As for polars, the magnetic field strength is of order of 10^7G (subsection 2.2.4) and most systems have orbital periods smaller than 2 hours (table 2.1). For $1M_\odot$ white dwarfs ($R = 5 \times 10^8$cm), we obtain r_A to be around a (eq(2.2)). This means there is no accretion disk in polars. In intermediate polars, on the other hand, there is a reason to believe that the magnetic field is weaker than in polars by an order of magnitude, and/or the mass accretion rate is an order of magnitude larger than in polars (subsection 2.2.4). In addition, most system have $P > 3$hr (table 2.2). Therefore, r_A is expected to be substantially smaller for intermediate polars. Accreting matter spilt over the Roche lobe first forms a thin ring around the primary and gradually transforms into a disk under shear viscosity. Comparing the circulation radius of the ring and the Alfvén radius, Hameury, King & Lasota (1986) concluded that no accretion disk is formed in intermediate polars with orbital period greater than ~ 5 hours, although this number is sensitive to the parameters of individual systems. On the contrary, Lamb & Melia (1986) discussed that the accretion disk formed while the system is on the early stage ($P_{orb} \sim 10$hr) continues to exist when the system evolves into a shorter period stage. Existence of the accretion disk in intermediate polars is still a matter of debate.

2.2.4 Measurements of Magnetic Field Strength

Magnetic field strength of polars has been measured either through the Zeeman splitting or cyclotron harmonics in the optical wave band. The splitting energy due to the Zeeman effect, the interaction between the magnetic moment of the electron and the magnetic field of the white dwarf, is

$$\begin{aligned}
\Delta E &= \frac{e}{mc}\vec{s} \cdot \vec{B} \\
&= 5.8 \times 10^{-2} \left(\frac{B}{10^7\mathrm{G}}\right) \quad (\mathrm{eV}).
\end{aligned} \tag{2.10}$$

Therefore, the splitting becomes some hundreds of Angstroms for the emission and absorption lines and the photoelectric absorption edge in the optical wave band. In figure 2.2, we show an example of observed Zeeman splitting. So far, the magnetic field strengths of four polars, AM Her, BL Hyi, E1405–451 and ST LMi have been measured (table 2.1). The Zeeman splitting method, however, has two inherent difficulties. First, unpolarized light from the accretion column usually disturbs the measurements in the bright state. Therefore, observation should be carried out during the so-called low state, when mass accretion rate is significantly lower than in the bright state (see Feigelson et al. (1978), for example).
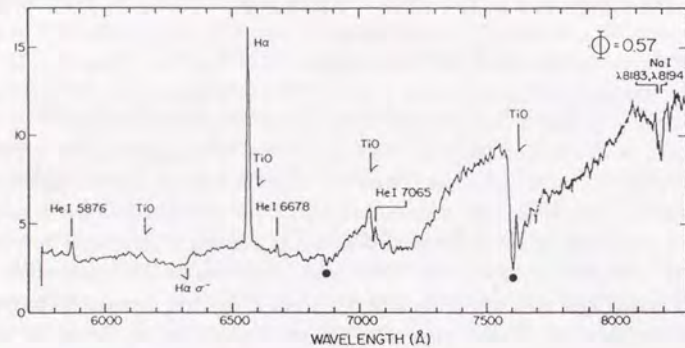
Figure 2.2: Optical Spectra of AM Her showing Zeeman absorption features (indicated with filled circles) at the linear polarization phase of 0.57 (from Schmidt *et al.* 1981).

Secondly, measured Zeeman splitting is a mean weighted by flux over observed photosphere. Therefore, we have to know flux distribution on the photosphere in order to deduce the field strength at the magnetic pole.

The cyclotron harmonics appear when free electrons are placed in the magnetic field. The kinetic energy of electrons perpendicular to the magnetic field lines are quantized into so-called Landau levels, and polarized light is emitted from transition of electrons between different Landau levels. Landau levels are expressed with the following equation.

$$
\begin{aligned}
E &= \hbar\omega_B \left(n + \frac{1}{2}\right) \\
&= \hbar\frac{eB}{m_ec}\left(n + \frac{1}{2}\right) \\
&= 0.116\left(\frac{B}{10^7G}\right)\left(n + \frac{1}{2}\right) \quad (eV),
\end{aligned} \tag{2.11}
$$

where n is the principal quantum number. For the magnetic field of 30MG, the lowest harmonics corresponds to $\lambda = 3.6\mu$m, and higher harmonics come into the optical wave band. Cyclotron emission lines was first found in the optical spectrum of VV Pup (Visvanathan & Wickramasinghe 1979). Recently, Cropper *et al.* (1988) show that, if the observation is performed with high sensitivity and resolution, cyclotron harmonics can generally be found from polars. An example of observed cyclotron harmonics is shown in figure 2.3. This method allows us to measure the field in accretion region itself, since the harmonics are
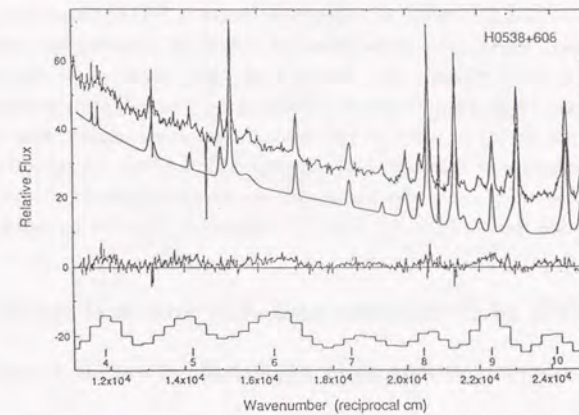
Figure 2.3:
The spectrum of H0538+608 from 4000 to 9100 Å(from Cropper *et al.* (1988)). The top curve shows the raw spectrum. The second one is the best fit spectral model composed of a continuum approximated by polynomials and emission lines. The model curve is shifted below by a factor of 1.5 for clarity. The third one is the fit residuals. The bottom one is the same as the third but after appropriate binninig. Harmonics numbers are show below.

usually observed as emissions only when the region is not behind the limb of the white dwarf. The field strength thus obtained are also listed in table 2.1.

We remark that these methods cannot be used for intermediate polars since they do not generally show appreciable polarization in the optical wave band. This might be attributed to a relatively weaker field strength of intermediate polar, so that cyclotron harmonics shifts to infra-red wave band. Alternatively, mass accretion rate from the secondary is usually larger in the system of longer orbital period (Patterson 1984). Therefore, mass accretion rate of intermediate polar is believed to be larger than of polar (see table 2.1, and 2.2). This might render the emission region optically thick for cyclotron emissions, even if the field strength of intermediate polar is of the same order as of polar.

2.2.5   Geometry of the White Dwarf

As depicted in figure 2.1, polars show linear or circular polarizations in optical wave band which varies at the rotational period of the white dwarf. The polarized light is probably emitted through circularization of accreting electrons. Therefore, assuming a simple dipo-

lar field configuration, we can deduce the orbital inclination (i) and the colatitude of the magnetic pole (β) by examining linear and circular polarization curve. Qualitatively, linear polarization is seen as a pulse when we observe the magnetic field of the accreting pole from the side. So-called 'linear polarization phase' is defined by adopting the epoch of linear polarization pulse as the phase origin. On the other hand, degree of circular polarization, which is zero at the origin of the linear polarization phase, gradually increases with the white dwarf rotation, and decreases when we look down the accretion column along the field line because of the reduction of emissivity (Chanmugam & Dulk 1981). An example of the fit to the observed polarization curve with the model characterized by i and β is already shown in figure 2.1 for AM Her. In table 2.1, i and β of polar thus obtained are listed.

2.3   Models of Emissions and Accretion Region of MCVs

2.3.1   Geometry and Emission Mechanisms of the Accretion Region

A schematic view of the accretion region is shown in figure 2.4. Since the matter from the secondary is considered to accrete at the free fall velocity in the gravitational potential of the white dwarf, the flow becomes highly supersonic near the surface of the white dwarf. Therefore, it has been believed that the shock wave occurs near the surface of the white dwarf, and the gravitational energy of the accreting matter is abruptly converted into thermal energy. Below the shock front, hot plasma with a temperature of a few tens of keV is formed. Due to a deep graviational potential, bulk of the emission from MCVs comes from this post-shock region. Three important emission mechanisms have so far been identified in the emissions from the accretion region (Lamb 1985 and references therein); hard X-ray emission represented with optically thin thermal bremsstrahlung with temperature of a few tens of keV; soft X-ray emission with blackbody spectrum with temperature of a few tens of eV; cyclotron emission in the optical and infra-red wave bands due to strong magnetic field of the white dwarf. The latter two emissions are, however, not found from any intermediate polar systems. Reason for this is unclear.

2.3.2   Models of the Accretion Region

Detailed calculation of the physical processes in the accretion region was performed first by Hoshi (1973) and Aizu (1973). Aizu (1973) treated the accretion process hydrodynamically in one fluid, 1-dimensional regime, and calculated the variation of temperature, density, and velocity of the flow along the accretion column, taking free-free cooling into account. The results are shown in figure 2.5. Since free-free emissivity is proportional to n^2, the accreting matter rapidly cools down as it approaches the surface of the white dwarf. Later, Frank, King & Lasota (1983) calculated the structure of the accretion region by taking the electron heat
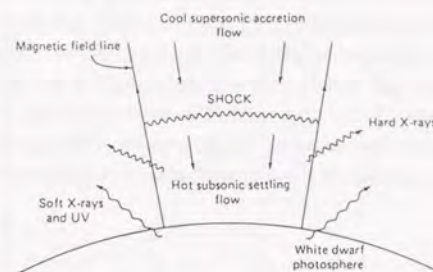
Figure 2.4: Schematic view of the accretion region.
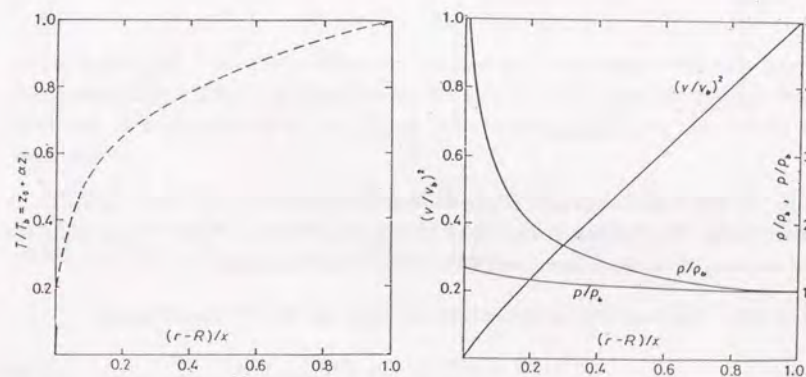
Figure 2.5:
Behaviour of (a) the temperature and (b) the mass density, the velocity of the flow, and the pressure of the accreting plasma in the postshock accretion column as a function of the distance from the white dwarf surface (from Aizu 1973). All these quantities are normalized by values just below the shock front, and the distance is normalized by the shock height.

conduction in the post-shock region into consideration. The behaviour of all the quantities

are qualitatively the same as those of Aizu (1973).

More practical calculation in which cyclotron cooling is also considered was presented by Fabian, Pringle & Rees (1976) follewed by Masters (1978) and Lamb & Masters (1979). Masters (1978) and Lamb & Masters (1979) calculated the efficiency of the free-free cooling and the cyclotron cooling, and showed their relative strength in the plane of L/f versus B (figure 2.6a), where f means the fractional area of the white dwarf over which mass accretion occurs, together with model spectra under the assumption of homogeneous emission region (figure 2.6b). Assuming that the soft X-ray is emitted as the reprocessed emission of free-free
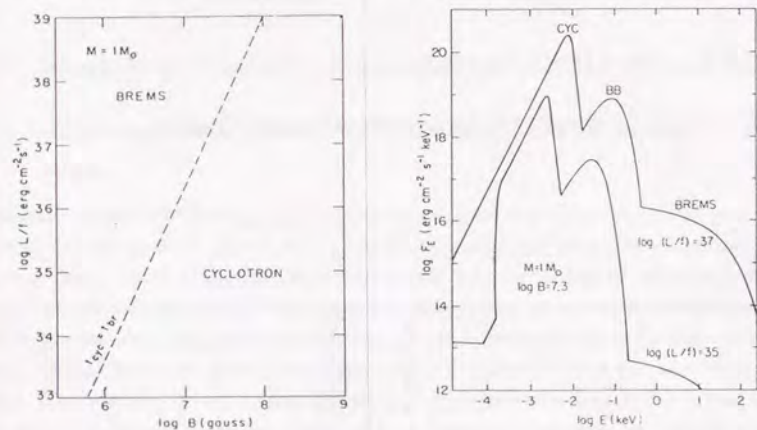
Figure 2.6: (a) Relative strength of the free-free cooling and the cyclotron cooling (from Masters 1978). (b) Calculated spectra of MCVs (from Masters 1978). f represents the fractional area of the white dwarf over which mass accretion occurs.

and cyclotron emission, they predicted that the soft X-ray flux F^{bb} should satisfy

$$F^{bb} = F^{cyc} + (1 - H)F^{br}, \qquad (2.12)$$

where F^{cyc} and F^{br} are the flux of cyclotron emission and thermal bremsstrahlung, respectively, and H represents the reflectivity of the hard X-ray emission. These results will be compared with observations in the following section.

Imamura et al. (1987) calculated the structure of the accretion region by taking into account the electron heat conduction as well as the free-free and the cyclotron cooling in the two fluid regime. They found that, although the behaviour of physical quantities in the postshock region are qualitatively the same as those of Aizu (1973), the preshock electrons are somewhat heated via the heat conduction due to high energy electrons in the postshock
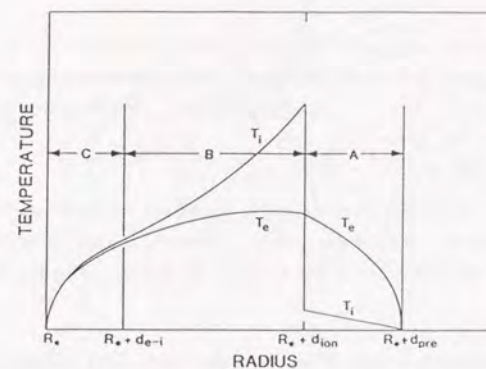
Figure 2.7: Behaviour of the temperatures of electrons and ions as a function of the distance from the white dwarf surface (Imamura et al. 1987).

region (figure 2.7). It is remarked, however, that the hard X-ray luminosity of the preshock region is roughly $\sim 10\%$ of that of the postshock region because of significantly lower density. Therefore, they conclude that the hard X-ray emission from the preshock region is generally negligible.

In summary, all the theoretical models of the emission region so far presented predict that the temperature is lower in the lower part of the accretion column, and the hard X-ray emission is weighted by this lower temperature region.

2.3.3 Size of the Emission Region

Although it is difficult to estimate the shape of the emission region, we can make simple estimate for the height and the area of it. The size of the emission region along the surface of the white dwarf is estimated by simple geometrical consideration. In the regime shown in figure 2.8, a magnetic field line satisfies the following equation in polar coordinate (r, θ) with respect to the magnetic axis.

$$r = C \sin^2 \theta,$$
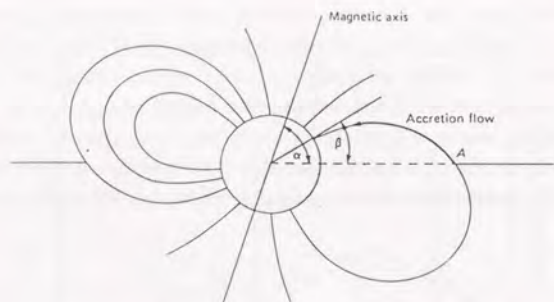
Figure 2.8: Accretion geometry of MCVs (from Frank, King & Raine (1985)).

where the value of C is different among different field lines. Since $r \sim r_A$ and $\theta = \alpha$ at point A (Alfvén point), $C = r_A \sin^{-2} \alpha$ and

$$\sin^2 \beta = \frac{R}{C} = \frac{R}{r_A} \sin^2 \alpha.$$

Therefore, the fraction of the area of the white dwarf over which accretion occurs is

$$
\begin{aligned}
f &= \frac{\pi R^2 \sin^2 \beta}{4\pi R^2} \\
&\simeq \frac{R \sin^2 \alpha}{4 r_A} \\
&\simeq \frac{R}{2 r_A} \sim 5 \times 10^{-2}
\end{aligned}
\tag{2.13}
$$

for $1 M_\odot$ white dwarf. We remark that since the accretion region may have a shape of a hollow cylinder, or even more, an arc, the fractional area derived above gives a rough upper limit. Observationally, f has been estimated from the intensity of the soft X-ray emission for polars. The soft X-ray emission has been believed to have blackbody spectrum, so that the its area can be estimated given the distance to the source. In AM Her, f is of order $10^{-4 \sim 5}$ (Tuohy et al. 1981, Heise et al. 1984).

On the other hand, the size of the emission region perpendicular to the white dwarf surface is estimated based on the calculation of Aizu (1973) (see below). The height of the emission region is estimated by the multiplication of the free fall velocity in the postshock region and the cooling time scale. Denoting the height as h, he obtained

$$h = 0.605 \, v_{ff} \, t_{ff}$$

$$= 0.605 \frac{1}{4} \sqrt{\frac{2GM}{R}} \frac{3kT}{2\mu m_H \epsilon_{ff}},$$

$$\tag{2.14}$$

where v_{ff} and t_{ff} are the free-fall velocity and the cooling time scale via free-free emission, and μ, m_H, and ϵ_{ff} represent mean molecular weight, mass of hydrogen, and free-free cooling rate per unit mass, respectively. With this equation,

$$\frac{h}{R} = 0.052 \left(\frac{M}{M_\odot}\right) \left(\frac{R}{5.5 \times 10^8 \mathrm{cm}}\right)^{-1} \left(\frac{n}{10^{16} \mathrm{cm}^{-3}}\right)^{-1}.$$

$$\tag{2.15}$$

This gives the upper limit for the height of the emission region, since, as described below, cyclotron emission is another important cooling mechanism. In addition, although Aize (1973) assumed complete cooling ($T = 0$) at the white dwarf surface, this may not be correct.

2.4 Observations

2.4.1 Hard X-ray Observations

As mentioned in subsection 2.3.1, the hot plasma with temperature comparable with the white dwarf potential energy ($\sim$ a few tens of keV) is expected to be formed below the shock front. A detector with sensitivity up to this energy is necessary to obtain complete spectral information. Before the launch of Ginga, only HEAO-A2 and A4 experiments can manage up to this energy. In figure 2.9, we show the observed spectra of AM Her in hard X-ray energy band as well as the soft X-ray component (Rothschild et al. 1981). From these experiments, it was found that spectra of AM Her and EF Eri are basically explained with optically thin thermal bremsstrahlung with temperatures of 30.9 ± 4.5keV (Rothschild et al. 1981) and 18.1 ± 3.5keV (White 1981). Nevertheless, MCVs are too weak in hard X-rays for HEAO-A2 and A4 experiments to obtain enough spectral information from other MCVs. Results of Ginga has, therefore, long been waited for.

Hard X-ray spectra of intermediate polars are systematically measured with EXOSAT, and the resutls are summarized in Norton & Watson (1989). Although the continuum spectra were approximated with a simple power-law (subsection 5.2.2) due to a restricted energy range of the EXOSAT-ME detector (up to $\sim$10keV), they found that the observed spectra undergo strong photoelectric absorption with effective hydrogen column density of order $\sim 10^{23}$cm^{-2}, and the photoelectric absorption is stronger in the minimum of the hard X-ray intensity than in the maximum.

2.4.2 Soft X-ray Observations

The soft X-ray emission from MCVs were first detected with HEAO-1 LED in AM Her (Tuohy et al. 1978, 1981). Since then, the soft X-ray emission has been regarded as a common feature
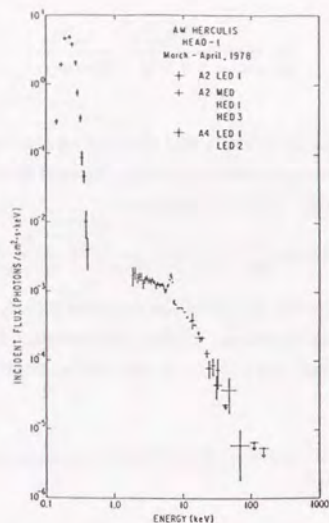
Figure 2.9: Observed photon spectrum of AM Her in the energy range between 0.1 and 100keV (Rothschild *et al.* (1981).

among polar. Determining the spectral shape of the soft X-ray emission is, however, difficult because strongly energy-dependent photoelectric absorption due to interstellar matter affects the observed spectra in this energy band. Therefore, the blackbody spectrum has usually been assumed. The blackbody temperatures are measured either with *HEAO*-1 LED or with *Einstein* OGS, or with *EXOSAT* LE for AM Her (between 27 and 55eV; Tuohy *et al.* 1978, 1981), VV Pup (between 17 and 50eV; Patterson *et al.* 1983), and E2003+225 (between 18 and 29eV; Osborne *et al.* 1986).

2.4.3   Soft X-ray Problem

In figure 2.10, composite spectrum of AM Her is shown (Lamb 1985). Among three emission mechanisms of MCVs, the flux of cyclotron emission is approximately consistent with that predicted by Masters (1978) and Lamb & Masters (1979). On the other hand, the relative intensity of the soft and hard X-rays are problematic. Although soft X-ray flux is expected to be of the same order as hard X-ray flux from eq.(2.10), Tuohy *et al.* (1978) originally claimed that the soft X-ray flux is ∼50 times as large as the hard X-ray flux based on the *HEAO*-1 observation. This soft X-ray excess is observationally established later with *EXOSAT* observations. For example, $F^{bb}/F^{br} \sim 10$ for AM Her (Heise *et al.* 1985) and ≥ 4.5 for E2003+225 (Osborne *et al.* 1986). This is so-called the 'soft X-ray problem'.
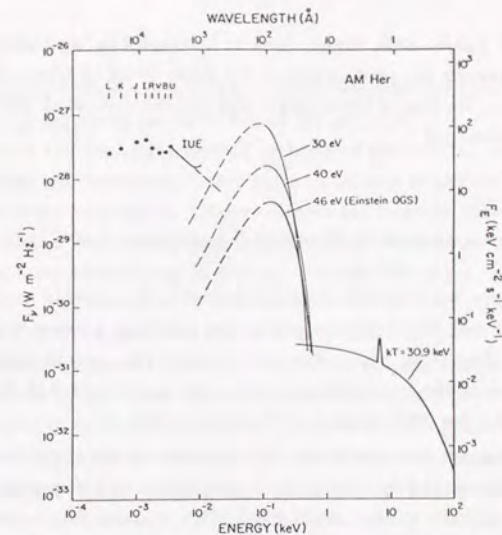
Figure 2.10: Composite energy spectrum of AM Her (Lamb 1985).
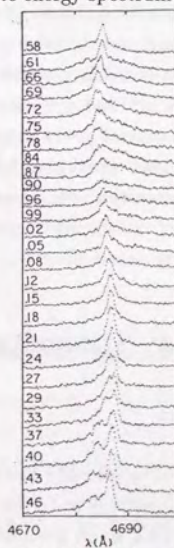
Figure 2.11: Orbital modulation of HeII emission line in AM Her (Crosa *et al.* 1981). Numbers indicated in the left mean the linear polarization phase.

To cope with this problem, various approaches have so far been made such as electron heat

conduction (King & Lasota 1980, Frank, King & Lasota 1983), high density blobs in the
accretion flow penetrating the photosphere of the white dwarf (Kuijpers & Pringle 1982),
and nuclear burning at the base of the accretion column (Fabbiano et al. 1981). The problem
is, however, not resolved yet.

2.4.4 UV, Optical and Infra-red Spectra

UV, optical and IR spectra of MCVs are characterized by a number of high excitation lines
such as HeII λ 4686 and NV λ 1240 as well as the cyclotron harmonics and the Zeeman
splitting structures. Examining ratios of various emission lines, we can estimate the density
and the temperature of the line emitting region. For example in AM Her, $10^{13} < n_e <
10^{14} \mathrm{cm}^{-3}$ and $T = 1 - 2 \times 10^4 \mathrm{K}$ (Liebert & Stockman 1985).

Important information also comes from measurements of the Doppler velocity modula-
tions of the center energies of these lines. In figure 2.11 shown is the orbital modulation of
HeII line profile of AM Her (Crosa et al. 1981). The emission lines are usually made up
with multi-components, and at least two components with different widths are identified in
a number of MCVs; one is the broad line component which probably originates from the ac-
cretion column far above the shock front, and the other is the narrow line component which
probably originates from the X-ray-irradiated face of the white dwarf. Utilizing the velocity
and the intensity of these lines, we can infer the configuration of the binary components and
the accretion stream as a function of orbital phase in polars. In intermediate polars, the
high excitation lines are modulated at the white dwarf rotational period, so that they are
utilized to infer the geometry of the accretion column near the surface of the white dwarf
(section 2.5.2).

2.5 Variations of X-ray Intensity

2.5.1 Aperiodic Variations

Cataclysmic Variables are characterized by intensity flickering by a factor of several with the
timescale ranging between a few tens of seconds and a few tens of minutes in the energy range
from IR to hard X-ray. In addition to this, quasi-periodic oscillations in the soft X-ray band
have so far been detected from six polars with periods ranging between 30s and 10m (Tuohy
et al. 1981; Patterson, Williams & Hiltner 1981; Singh, Atrawall & Riegler 1984; Beuermann
& Stella 1985; Osborne et al. 1986, 1987). These aperiodic intensity variations is generally
considered to be from due to variation of the mass accretion rate and/or inhomogeneities in
the accretion stream.

2.5.2 Spin Modulations

The spin modulation of the X-ray intensity is undoubtedly caused through the funneling of
accreting matter by the strong magnetic field of the white dwarf.

In polars, either the rise or the decline, or both, of the hard X-ray light curve occurs
simultaneously with the linear polarization pulse (Stockman & Liebert 1985, Mason 1985).
The linear polarization pulse occurs when we observe the magnetic field line of the emission
region perpendicularly. Therefore, the spin modulation of the hard X-ray intensity of polars
is caused by the X-ray emission region passing over the limb of the white dwarf, i.e. self-
eclipse.

King & Shaviv (1984) applied this idea also to intermediate polars. They assumed that
mass accretes onto one magnetic pole and forms a coin-shaped hard X-ray emission region
with negligiblly small height. They calculated the profile of the spin modulation of the hard
X-ray intensity with the inclination (i), the magnetic colatitude (β) and the fractional area
of the white dwarf (f) as free parameters. They concluded that the spin modulation of the
intermediate polars can be reasonablly explained if $f \sim 0.1$. In this model, the flux minimum
of the hard X-rays occurs when the accreting pole points away from the observer.

An alternative model is proposed by Rosen, Mason & Córdova (1988) and Hellier et
al. (1989, 1990, 1991). They found that the velocity of HeII and hydrogen emission lines
of several intermediate polars are modulate at the white dwarf rotation period, and are
maximally blueshifted when the X-ray intensity is maximum. They considered that these
lines originate mainly from the accretion flow bound for the upper magnetic pole of the
white dwarf (the pole in the same side of the observer with respect to the orbital plain), and
concluded that the maximum of the hard X-ray intensity occurs when the upper pole points
away from the observer. In this model, the minimum of the hard X-ray intensity is caused
by the absorption and/or scattering by the matter in the accretion column.

The origin of the hard X-ray spin modulation of intermediate polar is still a matter of
debate.

2.5.3 Orbital Modulations of Intermediate Polar

It is natural to consider that there can be no orbital modulation in hard X-ray intensity
since hard X-rays are emitted near the surface of the white dwarf. Norton et al. (1990),
however, found that there is a significant orbital modulation in the hard X-ray intensity
of FO Aqr observed with Ginga, and the profile of the spin-modulated hard X-ray light
curves significantly change with orbital phase (see also Norton et al. 1991). This reflects the
distribution of the accreting matter in the binary system, and may be useful to understand
the geomertrical structure in the binary system such as the accretion disk. Investigation of
the orbital modulation of the hard X-ray light curve has just started, and future development
is expected with Ginga data.

Chapter 3

The X-ray Observatory GINGA

3.1   The Ginga Satellite

Ginga, the third Japanese cosmic X-ray observatory, was launched by the M–3SII–3 rocket from Kagoshima Space Center at 15:30(JST) on February 5, 1987. It was thrown into a slightly elliptical ($e = 0.01$) orbit with the perigee of 520km and the apogee of 670km, and the orbital inclination of 31°. The orbital period of *Ginga* is 96 minutes, which means 15 revolutions per day. The ground station (at Uchinoura, Kagoshima) can contact the satellite only for about 10 minutes each in 5 consecutive orbits out of the fifteen. These orbits are usually called "contact orbits", and the other ten "remote orbits". *Ginga* carries three instruments; the large area proportional counter (LAC; Turner *et al.* 1987), the all sky monitor (ASM; Tsunemi *et al.* 1987), and the gamma-ray burst detector (GBD; Murakami *et al.* 1987). Figure 3.1 shows the configuration of these three instruments.

Figure 3.2 shows the definition of the satellite coordinates. The spacecraft has a momentum wheel to stablize the attitude of the spacecraft and control the attitude around the Z-axis (slew), and three magnetic torquers to control the Z-axis direction (maneuver). The speed of the slew and the maneuver is 14°/min and 5°/h, respectively. Therefore, maneuvability around the Z-axis is ∼170 times more efficient than that around X and Y-axis. In addition to the ordinary pointing mode, the spacecraft is operated in the scanning mode in which the field of view of the LAC scans a part of a great circle including a source. The great maneuvability around the Z-axis is utilized to rotate the Y-face on which the LAC is mounted. The scanning mode is used (i) to determine the source position precisely to compare with information in different wave bands, (ii) to see if there are any contamination sources in the field of view of the LAC, (iii) to confirm existence of a faint source, (iv) to examine surface brightness distribution of an extended source, and (v) to survey a wide sky region. The attitude of the spacecraft is controled in reference to four gyros to an accuracy of ∼ 0.1°. The final attitude of the spacecraft and the aspect of the LAC are obtained later on the ground with a typical accuracy of ∼ 0.02° based on data from the gyros and two star sensors.

The data obtained with the LAC, ASM, GBD, attitude, house keeping *etc.* are formatted
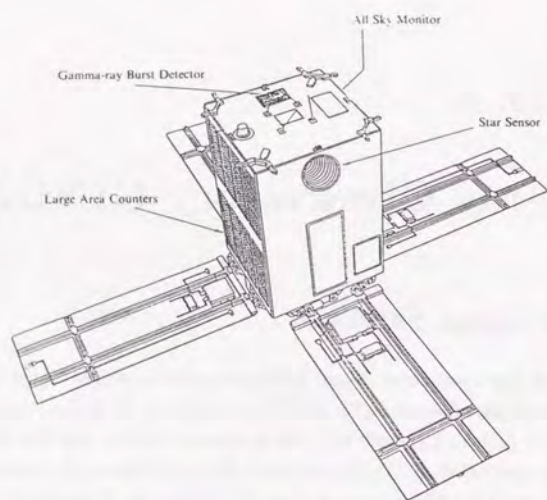
Figure 3.1: Configuration of the instruments of the *Ginga* satellite (taken from Turner *et al.* 1987).

by the on-board data processor (DP) for transmission and stored in the bubble data recorder (BDR; capacity of 41.9 Mbits) while the satellite is out of contact. These stored data are transmitted while the satellite is in contact with the ground station. Table 3.1 shows the recording time to fill up the BDR for each recording bit rate.

Table 3.1: Bit rates and the data recording time.

Bit rate		Recording time
High	(16 kbps)	43 min
Medium	(2 kbps)	5 h 42 min
Low	(512 bps)	22 h 45 min

3.2   The Large Area Proportional Counter

The LAC (Large Area proportional Counter) is the primary instrument of the *Ginga* satellite developed under a Japan–UK (United Kingdom) collaboration. The LAC has the highest
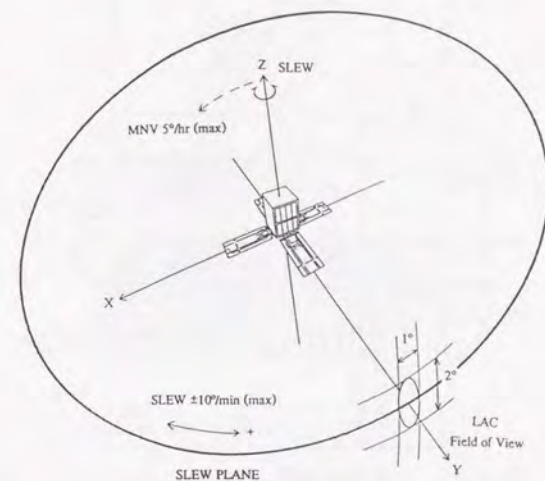
Figure 3.2: The satellite three axis. The LAC is mounted on the Y-face of the spacecraft. (Taken from Turner *et al.* 1987).

sensitivity so far achieved for cosmic X-rays in the 2–37 keV energy band and has been built to observe faint objects, from nearby stars to remote AGNs (active galactic nuclei), and to study the fast time variability of galactic compact objects. The LAC consists of 8 identical proportional counters with a total effective area of 4000 cm^2. Each proportional counter has its own high voltage supply operated normally at $\simeq$1830 volts. The counter is filled with gas composed of 75% argon, 20% xenon and 5% carbon-dioxide at a pressure of 1.86 atm (at 273K). The energy resolution is 18.0% at 6 keV and scales as $E^{-1/2}$ throughout the full energy range. The sensitivity of the LAC is shown in figure 3.3. There are abrupt sensitivity increases corresponding to the argon K-edge (3.0keV) as well as the xenon K and L-edges (29.6keV and 4.8keV, respectively). Decrease of the efficiency in lower energy is due to absorption in the beryllium window of 62μm thick. In front of the beryllium window, there are collimators made of 25μm steinless steel with hexagonal cross section divided in half to ensure the elliptical field of view (1.1° FWHM in azimuthal direction and 2.0° in longitudinal direction: see figure 3.2). The collimator acts also as a support for the beryllium window.

Each proportional counter is further devided by ground wires into 52 equivalent cells, each having an anode wire (figure 3.4). Among them, the bottom layer (V1) and the side layer (V2) form the counters which guard each proportional counter from non-X-ray background

Figure 3.3: The sensitivity of the LAC

from three sides. The remaining two sides of the counter corresponding to both ends of the anode wires are guarded by square-plate readout electrodes called end-veto (EV). The other layers are used as the signal layers; they are composed of the top layers (L1 and R1) and the middle layers (S23). These layers are electrically connected as shown in figure 3.4, and for the purpose of background reduction, these three signals are processed in mutual anti-coincidence. An event in each counter is accepted as a valid X-ray signal if it gives signal in only one of the three signal layers (L1, R1, or S23), but not in the guard layers (V1, V2 and EV). Otherwise, the event is discarded as a charged particle event. Furthermore, 0.2mm thick tin foils placed around the counters prevent hard X-rays (mostly of cosmic diffuse X-ray background) from penetrating the counter walls and producing spurious background. With these methods, the internal background of the LAC (see the next section) is reduced by factor of 20, to the level of 3.5×10^{-4} counts s^{-1}cm^{-2}keV^{-1}.

Each proportional counter has an independent electronics system. The block diagram of on-board electronics is shown in figure 3.5. An X-ray event is pulse-height analysed by a 6-bit ADC into 64 energy channels covering 0–37 keV. The on-board data processor (DP) counts the number of events in each pulse-height channel using on-board memory during a fixed time interval, and formats the resultant spectrum into telemetry. Depending upon how the spectra of different layers and detectors are combined and how the original 64 pulse-height

Figure 3.4: Schematic view of the LAC detector

channels are re-binned, following four formatting modes are available for the LAC data.

- MPC–1 mode: Events are accumulated separately for the top (L1+R1) and the middle (S23) layers of the 8 detectors, thus producing 16 separate spectra simultaneously. Among the 64 channels, the higher 32 channels are binned up into 16 channels. Thus each spectrum consists of 48 energy channels. The energy corresponding to the lowest two channels are below the lower discriminator (LD). Therefore, the lower 30 channels cover 1.2–18.6 keV and the higher 16 channels covers 18.6–37.2 keV. This mode is mainly used for spectral study of faint sources.

- MPC–2 mode: Sixteen 48-channel spectra in the MPC-1 mode are summed to two spectra. One is the summation over the two layers of the first 4 detectors, and the
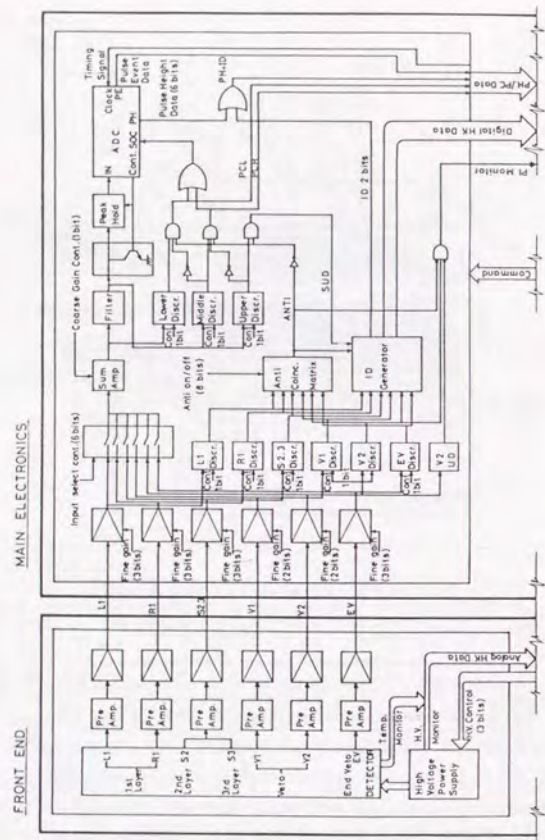
Figure 3.5: A block diagram of the on-board electronics.

other over the remaining 4 detectors. This means 8 times compression of the MPC-1 mode.

- MPC–3 mode: Events from the two layers of the 8 detectors are accumulated into a single 12-channel spectrum. Each energy channel corresponds to 4 consecutive channels in the MPC–1 and MPC–2 modes. The data are compressed further by 8 times compared with MPC-2 mode. This mode is used mainly for fast timing studies with intermediate energy resolution.

- PC mode: This mode is used only for fast timing observations of the bright galactic

objects. To reduce the dead time, the ADC is not used. The X-ray energy is binned into 2 energy channels by using 3 (lower, middle and upper) discriminators. The levels of discriminators can be set independently for two groups of four detectors.

Table 3.2 lists the number of energy channels and the maximum time resolution of these four DP modes for three recording bit rates.

Table 3.2: Time resolution of the LAC data.

Mode	number of PH Channel	Bit rate High	Medium	Low
MPC–1	48	500ms	4 s	16s
MPC–2	48	62.5ms	500ms	2s
MPC–3	12	7.8ms	62.5ms	250ms
PCᵃ	2	0.98ms	7.8ms	31.3ms
		(1.9ms)	(15.6ms)	(62.5ms)

a: The higher energy channel has twice worse time resolution (numbers in parenthesis).

3.3   Background in the LAC

The X-ray spectrum obtained with the LAC contains not only X-rays from celestial objects but also from background sources. It is highly important to evaluate the background intensity, since there is no way to obtain background data simultaneously. In this section, the nature of the background in the LAC is described, and methods to remove it from the on-source data are presented. The LAC background is divided into aperture diffuse X-ray component and internal detector background.

3.3.1   Internal Background

The internal background which is generated by non-X-ray events is about 50 counts s^{-1} in the remote orbits and becomes as much as $\sim$100 counts s^{-1} in the contact orbits. The internal background originates from;

1. Cosmic-ray charged particles such as protons and electrons, and secondary atmospheric γ-rays produced by them. Their contribution increases in regions of low geomagnetic rigidity and in the South Atlantic Anomary (SAA), where the earth magnetosphere becomes as low as the satellite orbits. Because of the orbital inclination of 31°, the satellite passes the SAA in 7 orbits including all of the contact orbits. To protect the detector against excessive counting rate, the LAC high voltage is turned off during the

SAA passage, both manually by a programmed command and automatically by the RBM (a part of the GBD) which monitors the particle flux.

2. Cosmic diffuse X-rays. Cosmic diffuse X-rays above ~35keV penetrating the tin shield generate "X-ray" events in the detector with energies > 5keV through xenon K-escape.

3. Radio-active isotopes. Material of and/or around the LAC is activated during the passage of the satellite through the SAA and shows residual radio activity, presumably γ-decay. At least two different components are involved; one with a decay life time of ~ 41min, and the other with that of ~ 8h. They have not been identified with particular nuclear species.

4. Geomagnetically trapped charged particles.

5. Solar X-ray and its reflection from the illuminated limb of the earth. If the LAC points the direction within 90° from the sun, solar X-ray intrudes the LAC detecter due to scattering in the collimator of the LAC. Observations are usually scheduled so that the sun is at an angle greater than 90°. The limb of the earth illuminated by the sun causes a contamination via reflection. This effect is usually negligible, provided that the LAC points away from the illuminated limb by more than ~ 6°.

Figure 3.6 shows the background behavior during an observing day. Variation of the components 1 and 3 listed above are clearly seen. The contribution from the SAA strongly depends upon the altitude of the satellite in the SAA. Therefore, in addition to the variation within one day, the internal background varies with a 37d period, coincident with the rotation period of argument of perigee of the satellite orbit.
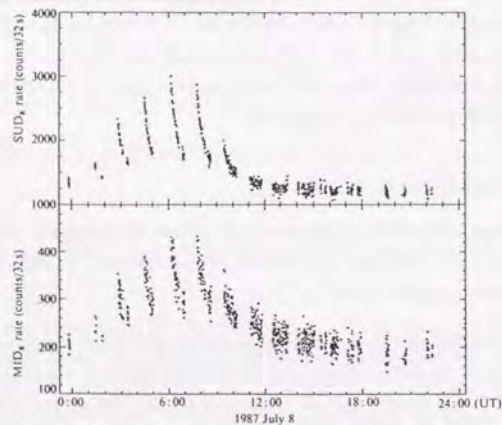

Figure 3.6: The background behavior during an observing day (taken from Hayashida *et al.* 1987). For SUD and MID, see subsection 3.3.2.

3.3.2   Background Reproduction

To estimate the LAC background during on-source observations, the following sets of information can be used as background monitor counts.

1. SUD: The count rate of the LAC above 37keV. Since the X-ray efficiency is less than ~3% (figure 3.3), the SUD count rate mainly represents the flux of high-energy particles and γ-rays.

2. RIG: The geomagnetic rigidity. It is defined as the minimum momentum per elementary unit charge to penetrate the earth magnetosphere at a given point of the orbit.

3. MID: The count rate of the middle layer (S23) of the LAC. This is a good monitor of the background below 8keV since in this band most of the true X-rays are absorbed in the top layer. This monitor is available only in the MPC–1 mode.

4. PIM: The count rate of the LAC wires which are screened from direct illumination of aperture X-rays but are otherwise similar to the other wires.

5. SOL2: The count rate of a solid-state detector, a component of the GBD experiment.

To reproduce the LAC background, Hayashida *et al.* (1989) first investigated correlations between the LAC count rate from blank skies and the background monitor counts described above. They decomposed background spectrum into different components with respect to the counts of each background monitor. Finally they constructed the background spectrum as a linear combination of these components, referring to count rates of the background monitors during the on-source observation.

Among the background monitors, the SUD count rate correlates well with the LAC count rate for blank sky observations (see figure 3.7), and the background in the remote orbits can be represented solely with this SUD-dependent component. This way of background reproduction is called "SUD-sorting method". To utilize the data taken in contact orbits, it is necessary to introduce a RIG-dependent component and two radioactive decay components in addition to the SUD-dependent component. This way of background reproduction is called "Method I" in Hayashida *et al.* (1989). With these methods, the background can be subtracted from the on-source data by referring to the background monitor counts. Notice that the background observation should be performed at a similar phase (preferably very close in time) of the 37d period as the on-source observation.

Even if no appropriate background data are available, it is now possible to produce model background data with enough accuracy from a large data base. In this case, one more parameter, the argument of the perigee of the satellite orbit, is necessary to reproduce the 37 day periodicity. The count rate of the middle layer is additionally used in the MPC–1 mode. This way of background estimation is named "Method II" in Hayashida *et al.* (1989).
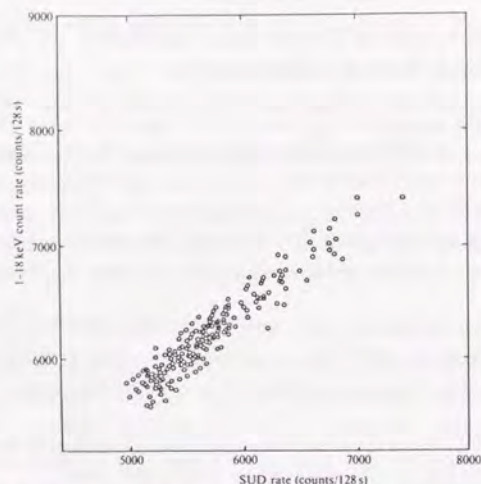
Figure 3.7: Relation between the SUD count rate and the LAC count rate for a blank sky.

For all the three methods of background reproduction presented above, 1σ error of the internal background estimation is less than 0.04 counts s^{-1} keV^{-1} in 2–10 keV for an observation of 10,000 seconds.

3.3.3   Fluctuation of Diffuse X-ray Background and Detection Limit of the LAC

The cosmic diffuse X-ray background (CXB) within the LAC field of view is 18 counts s^{-1} in 2–10keV on the average. At least a fraction of the CXB count rate is known to come from point sources which are below the detection limit of the LAC. The number of these sources within a field of view statistically fluctuates from sky to sky. As a result, the count rate in the "off-source" sky varies by 0.68 counts s^{-1} (1σ) in 2–10 keV, which is by a factor of 2–3 larger than the error of the internal background presented in the previous section. Therefore, the detection limit of the LAC is ultimately determined by the fluctuation of the number of unresolved sourced within the LAC field of view. At 3σ level, the fluctuation amounts to 2.6 counts s^{-1} in 2–10 keV (Hayashida *et al.* 1989), which is quoted as a nominal detection limit of the LAC. This count rate corresponds to an incident energy flux 6×10^{-12} erg $s^{-1}cm^{-2}$ (=0.3mC) in 2–10keV if the source has a spectrum like the Crab nebula. Notice that this limit is reduced by a factor of a few in scanning observations or if a target shows pulsation.

Chapter 4

Observations

4.1   Overview

As described in the previous chapter, the LAC energy range extends up to $\sim$40keV, which is essential for investigating hard X-ray emission from MCVs. In addition, the LAC has a sensitivity high enough to observe sources as weak as 0.5 mC. This limit is a few times as low as that of the *HEAO*–A2, A4, and the *EXOSAT* ME detectors. Therefore, *Ginga* has enabled us to study hard X-ray emission from MCVs systematically for much larger number of samples, and a number of MCVs have been observed by many investigators with various scientific objectives. Observations have been aimed at searches for QPOs (quasi-periodic oscillations), studies of hard X-ray emission mechanism in terms of spectral analysis, investigations of the binary structure and accretion stream utilizing simultaneously with other energy bands. Some of these data have already been published. These publications, however, concern a rather detailed modeling of a single source. This thesis, on the other hand, intends to establish a unified description of the hard X-ray emission mechanism and the origin of the spin modulation of MCVs by comparing many sources. All the data that meet this purpose have been reanalysed from a unified point of view under permission of individual PIs (Principal Investigators). To begin with, details of the observations are explained in this chapter.

Table 4.1 lists all the MCVs observed with *Ginga* from 1987 February to 1991 May. Most sources were expected to be strong, so that the observations were performed basically in the pointing mode. The LAC pointing observation is interrupted by the passage of the spacecraft through high background regions (section 3.2) or by the earth occultation of the source. Therefore, total exposure time of the pointing observation in a day is limited to $(1-3) \times 10^4$ seconds. Off-source background observations were performed for each source for 1 day either just before, just after, or in the middle of the on-source observations. The source intensities are presented in the counting rate of the LAC (counts s^{-1}) in 1.2–37.4keV for 8 detectors with a total effective area of 4000cm^2. The counting rate for the Crab nebula with the LAC is $\sim 11,000$ counts s^{-1}. Therefore, the intensity of the observed MCVs ranges a few milli-Crab or less according to the conventional Crab unit.

Table 4.1: Observation log of MCVs

Name of Source	Date of Observation(UT)	DP[a] Mode	Exposure Time (sec)	Average[b] Intensity	PI[c]	Ref.
Polars						
AM Her	'89 Sep 17.9–19.6, 20.8–21.5	MPC-1	99,500	42.3	Osborne	
EF Eri	(1)'88 Nov 30.8–Dec 2.8	MPC-1	29,100	32.5	Watson	Watson *et al.* '90
	(2)'91 Jan 23.7–24.4	MPC-1 (MPC-3)	21,200	24.3	LJO	
H0538+608 (BY Cam)	'88 Feb 7.8–10.7	MPC-1	86,300	(PS) 14.0 (FS) 22.3	Bradt	Silber *et al.* '90 Ishida *et al.* '91
E1405-451 (V834 Cen)	'90 Feb 10.0–10.6, 12.9–13.5	MPC-1 (MPC-2)	51,800	7.1	Ishida	
E2003+225 (QQ Vul)	'91 Apr 9.2–10.4	MPC-1	24,400	3.1 (> 4keV)	LJO	
CW1103+254 (ST LMi)	'90 May 7.4–7.8	MPC-1	10,800	< 3	Watson	
Intermediate Polars						
GK Per	(1)'87 Sep 22.7–24.5	MPC-2	46,200	11.4	PV	Ishida *et al.* '91
	(2)'90 Sep 7.4[d]	MPC-1	100	144.0	Koyama	
TV Col	'87 Sep 21.5–22.3	MPC-2	18,900	21.0	PV	
EX Hya	'88 Jun 16.3–17.0	MPC-1	20,200	49.6	Rosen	Rosen *et al.* '91
FO Aqr	(1)'88 Oct 29.4–31.0	MPC-1	47,000	14.3	Norton	Norton *et al.* '90
	(2)'90 Jun 27.2–Jly 2.0	MPC-3 (MPC-1)	55,000	17.6	Osborne	
AO Psc	'90 Jly 10.8–11.5	MPC-1	21,500	17.0	Watson	
3A0729+103 (BG CMi)	'88 Nov 28.8–29.8	MPC-1	27,100	7.3	McCardy	
RE0751+14	'91 May 4.5–5.7	MPC-1	28,200	12.4	TOO	

a: Data modes in contact orbits are shown in parenthesis in case it is different from that in remote orbits.
b: counts s^{-1} in 1.2-37.4 keV for the 8 detectors with 4000cm^2.
c: Principal Investigator (LJO = Latter-phase Joint Observation, PV = Performance Verification phase, TOO = Target Of Opportunity).
d: Data were taken during a single scan only.

In principle, all the data listed in table 4.1 are used in this thesis. However, observations carried out in the MPC–3 mode are not suitable since the present purpose requires full spectral information. Therefore, the observation of FO Aqr in 1990 is excluded from the

analysis. Details of the rest of observations are explained in the following two sections.

At the end of this chapter, X-ray light curves after background subtraction and aspect correction are presented in figure 4.3. Used energy range for the light curves of polars and intermediate polars are 1.2–37.4keV and 1.2–18.6keV, respectively, although the lower boundary is set at 4.6keV for a E2003+225 and RE0751+14 which are contaminated by solar X-rays. Rotational period of the white dwarf is indicated by a line with arrows at both ends. The background subtraction was performed with the Method II (section 3.2) in order to utilize the data taken in contact orbits as well.

4.2   Observations of Polars

4.2.1   AM Her

The observation was performed for four days in 1989 September 17–21 and the background data were taken on the third day. There was no earth occultation of AM Her during the observation, so that the total exposure time of 100,000 s was obtained from the three days of on-source observation. The observed flux was consistent with that obtained with *HEAO*-1 (Rothschild *et al.* 1981). It is well known that AM Her shows two different states. One is "normal state" when the soft and hard X-ray light curves are in phase and the other is "reversed state" in which the hard and soft X-ray light curves are 180° anti-phased. Although no information is available about the soft X-ray light curve, the shape of the light curve (figure 4.3) resembles that of the normal state (Swank 1979) rather than the reversed state (Heise *et al.* 1985).

4.2.2   EF Eri

EF Eri was observed twice with *Ginga*, in 1988 December and in 1991 January for two days and one day, respectively. There was a simultaneous *ROSAT* coverage in the 1991 observation. *ROSAT*, a joint Germany–UK–US satellite, was launched with the Delta II rocket from Cape Kennedy on 1990 June 1, carrying an imaging X-ray telescope (XRT) and an XUV telescope (WFC) jointly covering wave bands between 700 and 6 Å. The light curve (figure 4.3) shows beat perodicity of ~8h between the rotational period of the white dwarf (81min) and the orbital period of *Ginga* (96min). The spin phase average intensity was about 1.5 times stronger in 1988 than in 1991.

4.2.3   H0538+608 (BY Cam)

The three day on-source observation of H0538+608 was performed in 1988 February 7–10. Simultaneous optical photometry and spectroscopy were carried out at MDM Observatory, Kitt-peak (Silber *et al.* 1990). H0538+608 is known as a peculiar source among polars since it shows aperiodic variation so strongly that periodic variations sometimes disappear both

in optical and X-ray (Remillard *et al.* 1986, Shrader *et al.* 1988). The *Ginga* observation encountered a sudden change in the source behaviour. As shown in figure 4.3, the intensity modulation at the spin period (3.33±0.05h) of the white dwarf is clearly seen in the first half of the observation, whereas it completely disappears in the latter half. These two states are named "pulsing state" and "flaring state", respectively (Ishida *et al.* 1991a). The average intensity in the flaring state is ∼1.5 times higher than in the pulsing state.

4.2.4   E1405-451 (V834 Cen)

The observation was carried out for four days in 1990 February 10–13 of which three days are for on-source pointing. The background data were taken on the third day. Unfortunately, the drift rate of the gyro around the Z-axis became unpredictably unstable, so that the source gradually drifted from the center of the field of view in the first two days. As we discarded the data with transmission less than 60% to avoid large error in aspect correction, only about half of the data remained. During the observation, the behavior of E1405-451 was fairly steady, and clear pulsations were seen as in figure 4.3. The average intensity is in agreement with the *EXOSAT* observation (Osborne *et al.* 1984).

4.2.5   E2003+225 (QQ Vul)

The observation of E2003+225 was planned as a simultaneous observation with *ROSAT* on 1991 April 10. At that time, however, the angle between the LAC pointing direction and the sun was less than 90°, and the *Ginga* data were severely contaminated by solar X-rays below 4keV (subsection 3.3.1). Since almost all the data were taken during the day time of the satellite, no information was available below 4keV. The source was as expected very weak, only a few counts above 4keV.

4.2.6   ST LMi (CW1103+254)

The observation was performed for 1 day on-source pointing on 1990 May 7. From the *EXOSAT* observation, it was known that ST LMi is bright during a very small fraction of a spin cycle of the white dwarf (Osborne 1988). The expected count rate at the pulse peak is about 10 counts s^{-1} for *Ginga*. As shown in figure 4.3, however, the data coverage was very poor. We could obtain only the upper limit of the intensity as ∼3 counts s^{-1} (3σ) in 1.2–37.4keV. We therefore exclude this source from the subsequent data analysis.

4.3   Observations of Intermediate Polars

As introduced in chapter 1, intermediate polar shows two coherent periodicities related with the orbital motion and the white dwarf rotation. Since X-ray is emitted at the base of the accretion column, its intensity is mainly modulated in synchronization with the white

dwarf rotational period, and the orbital modulation of the hard X-ray intensity has been found from only a few intermediate polars (for example, EX Hya and FO Aqr; see below). Therefore, we concentrate on the X-ray intensity modulation at the white dwarf rotational period in this thesis.

4.3.1   GK Per in quiescence

The observation was carried out for two days on 1987 September 23–24 in MPC–2 mode as a part of the PV(Performance Verification) phase program (Ishida *et al.* 1991b). The background data was taken on September 22. The average source intensity was consistent with the *EXOSAT* observations in quiescence (Norton *et al.* 1988).

4.3.2   GK Per in outburst

GK Per showed an optical outburst behaviour in 1989 July, lasting for about 50 days. On September 7, *Ginga* detected GK Per in outburst by chance during the hot bubble survey in the Perseus region (Ishida *et al.* 1991b). Figure 4.1 shows the scan profile of GK Per. Although the quality of the data is poor since GK Per passed the field of view only once with the maximum transmission of 40%, we found them to be available for spectral analysis after proper aspect corrections. The average intensity after the aspect correction was about 140 counts s^{-1}. The exposure time was, however, shorter than the rotational period of the white dwarf (351.341 sec), so that we could not study the pulsation.

4.3.3   TV Col

The observation was carried out on 1987 September 21. The background data were shared with the observation of GK Per in quiescence. The observation was frequently interrupted by the SAA and the earth occultation one after another, so that the efficiency of data taking was low. Although the pulsation of 1911s was detected in the *EXOSAT* observation, it was not found with the *Ginga* data.

4.3.4   EX Hya

The observation was carried out on 1988 June 16. In EX Hya, there is a well-know orbital dip caused by the eclipse of the emission region by the secondary (Rosen, Mason & Córdova 1988). The observation was scheduled so as to maximize the coverage of the predicted eclipsing dip, and we have detected totally 7 dips. The expected dip positions are indicated with arrows in figure 4.3. EX Hya is know as one of the brightest MCVs, and as expected, the average intensity was about 4.5 mC.
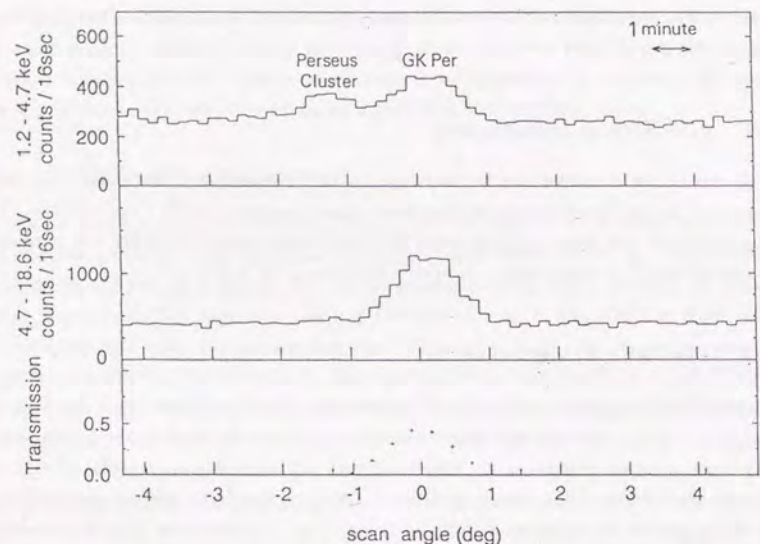
Figure 4.1: The scan profile of the GK Per. In the lower energy band, Perseus cluster is also detected.

4.3.5   FO Aqr

FO Aqr was observed for two days on 1988 October 29–30. Unlike other intermediate polars, FO Aqr shows clear orbital modulation of X-ray intensity, and the profile of the rotational intensity modulation significantly varies at the orbital period of 4.85h (Norton *et al.* 1990; see also Norton *et al.* 1991).

4.3.6   AO Psc

The observation was performed for a day on 1990 July 11. The rotatinal intensity modulation is stable compared with other intermediate polars.

4.3.7   3A0729+103 (BG CMi)

The observation was performed for one day on 1988 November 29. 3A0729+103 is the only intermediate polar that shows polarization in optical wave band (Penning, Schmidt & Liebert 1986), which indicates that the white dwarf in intermediate polar is really magnetized.

4.3.8   RE0751+14

RE0751+14 was first detected with the WFC on board *ROSAT* (see 4.2.2) during the un-biased all sky survey phase. Therefore, it was difficult for *ROSAT* to study time variability at that time. A periodicity of 13.8 min was found with an IR observation, suggesting that the source is a new intermediate polar. Intermediate polar is generally a strong hard X-ray source, although RE0751+14 had not been catalogued in X-rays. Therefore, we performed scanning observations with *Ginga* on 1991 May 1 and we obtained totally 4 scans just before the pointing observation. Figure 4.2 shows the scan profile over the RE0751+14 region. A clear peak is found at the position of RE0751+14, and as will be described later, an X-ray periodicity consistent with that of the IR observaiton was detected in the *Ginga* data. A detection of persistent X-ray pulsation suggests that the white dwarf in the system is magnetized. The periodicity at $\sim 10^3$s is typical of rotational periods of white dwarfs in intermediate polar systems (table 2.1), and it is a little too short for an orbital period. It is, therefore, suggested that RE0751+14 is a new intermediate polar. After the scanning observation, ordinary pointing observation was performed for 1 day on May 4–5. About two-thirds of the pointing data were, however, contaminated by solar X-rays (subsection 3.3.1) as they were taken during daytime of the satellite under unfavourable sun angles. Therefore the energy channels below 4keV of these data are not available.
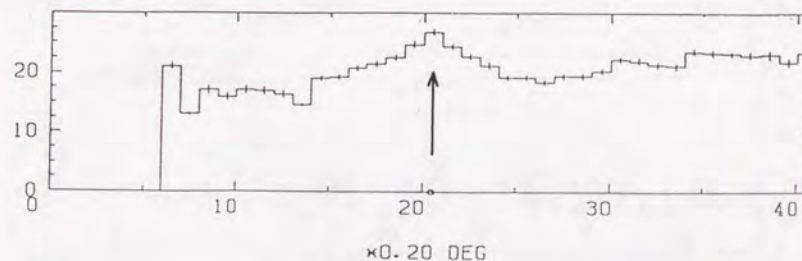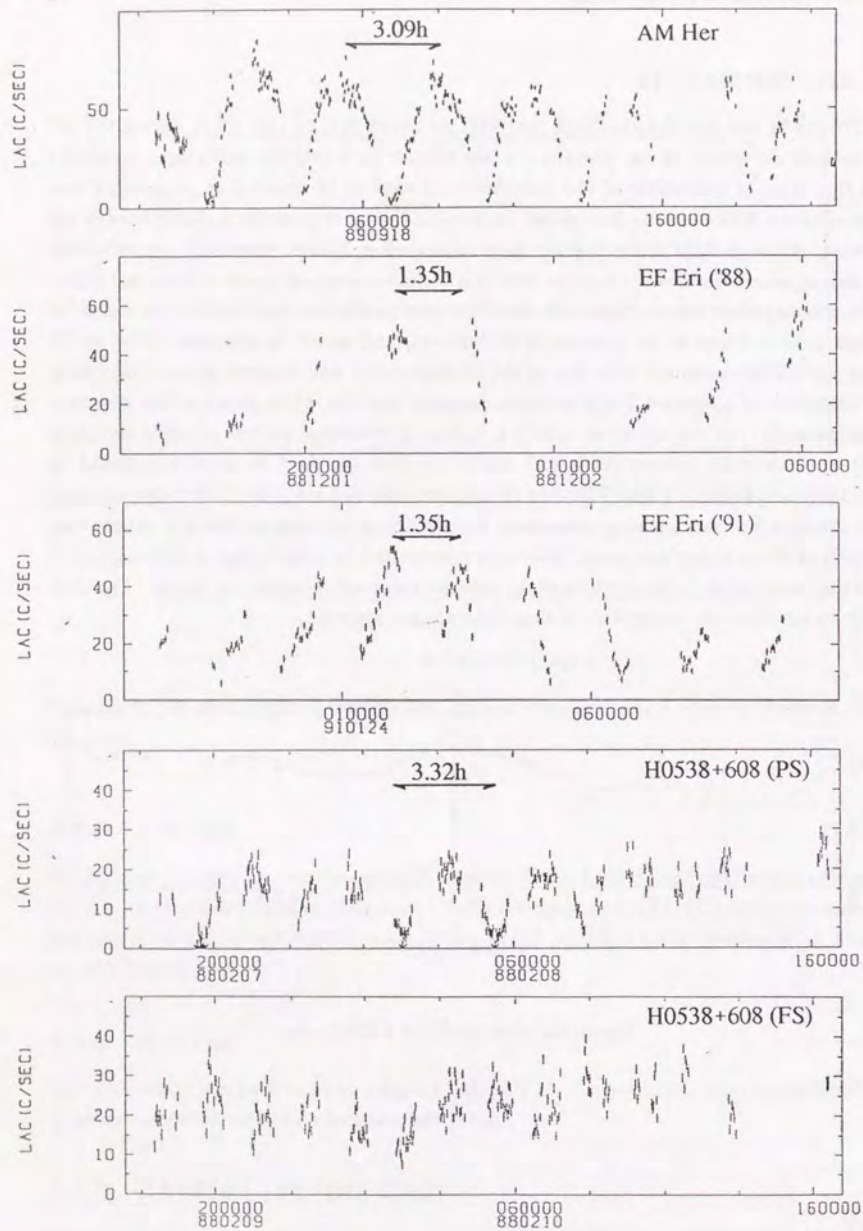

Figure 4.2: Scan profile of RE0751+14
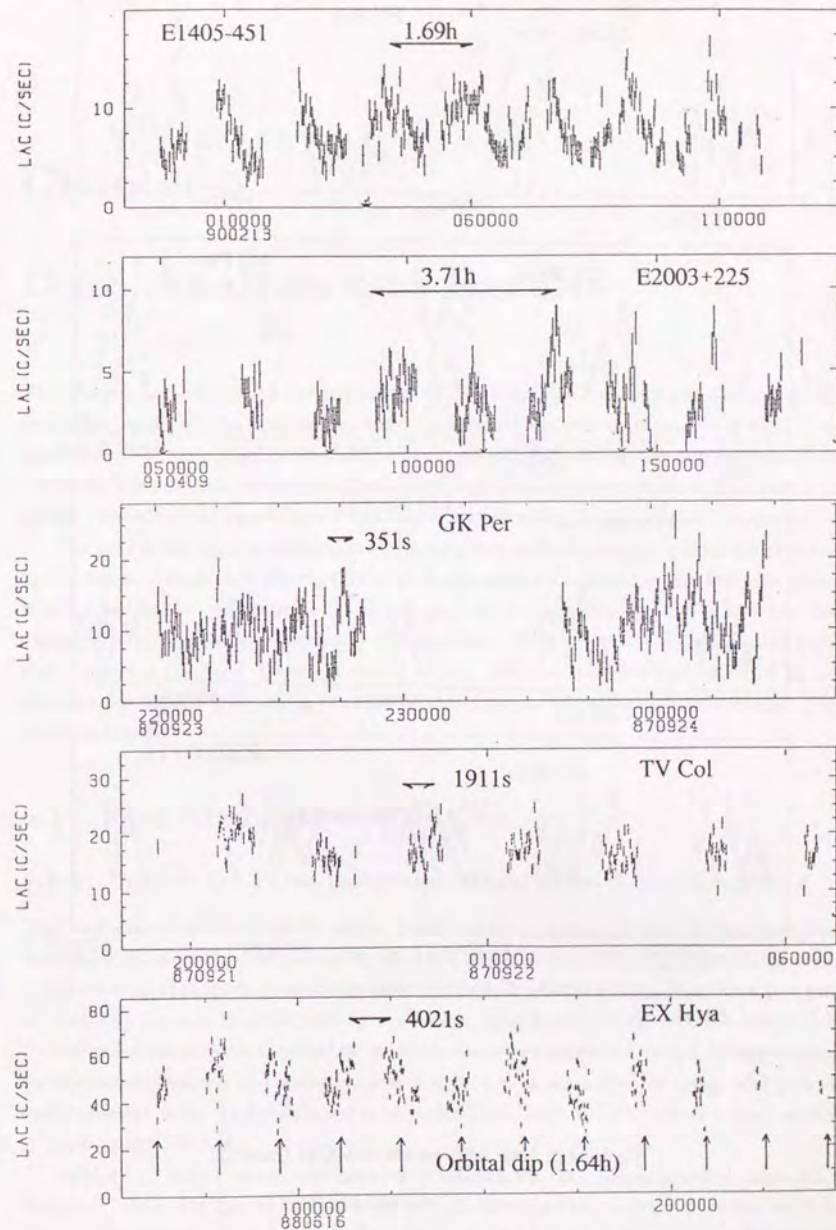
Figure 4.3: Raw light curves of MCVs.
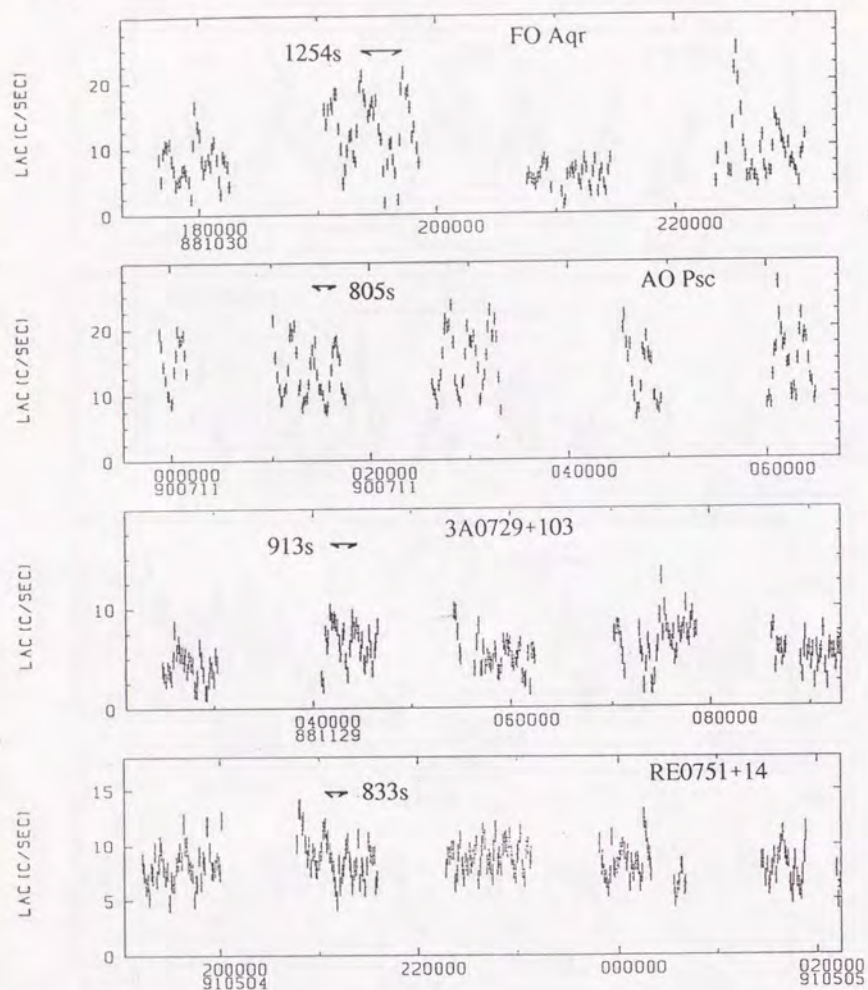
Figure 4.3: Raw light curves of MCVs (cont'd).

Figure 4.3: Raw light curves of MCVs (cont'd).

Chapter 5

Data Analysis and Results

This chapter is dedicated to the description of the *Ginga* data analysis and derived results. From the period-folding analysis, we have reconfirmed the modulations of the hard X-ray intensity at the rotational period of the white dwarf. Examining the energy dependence of the modulation light curves, we have found that there are appreciable differences in the energy dependence of modulation amplitudes between polars and intermediate polars.

The hard X-ray spectra above 10keV of both polars and intermediate polars are explained by the emission from optically-thin thermal plasma with a temperature of a few tens of keV, which confirms the existence of the shock wave in the accretion column which has been expected from the standard accretion shock model. We propose a unified spectral model which explains the hard X-ray spectra of MCVs. We also examine properties of an iron emission line from MCVs, which provides us with information of the structure around X-ray emission region.

5.1   Spin Modulation of MCVs

5.1.1   Search for Periodicity and Modulation Light Curves

The intensity modulations at the white dwarf rotational period in hard X-rays have been established through the observations by *HEAO–1*, *Einstein* and *EXOSAT*. The precise period is measured by optical observations for most MCVs with relatively longer base lines (see table 2.1 and 2.2). It may, however, still be worthwhile reconfirming them with the *Ginga* data. To determine the rotational period of the white dwarf, we adopt the period folding method; background-subtracted and aspect-corrected light curves are folded at many trial periods, and deviations from the flat light curve are calculated. Most MCVs showed a clear reduced χ^2 peak except TV Col.

Reduced χ^2 values versus trial periods are shown for the sources listed in table 4.1 in figure 5.1. Both AM Her and H0538+608 were observed in the on-source pointing mode for 3 days. The pulsation was, however, detectable only during the first 1.5 day for H0538+608 and its averaged intensity was 4 times weaker than that of AM Her, which reduced the
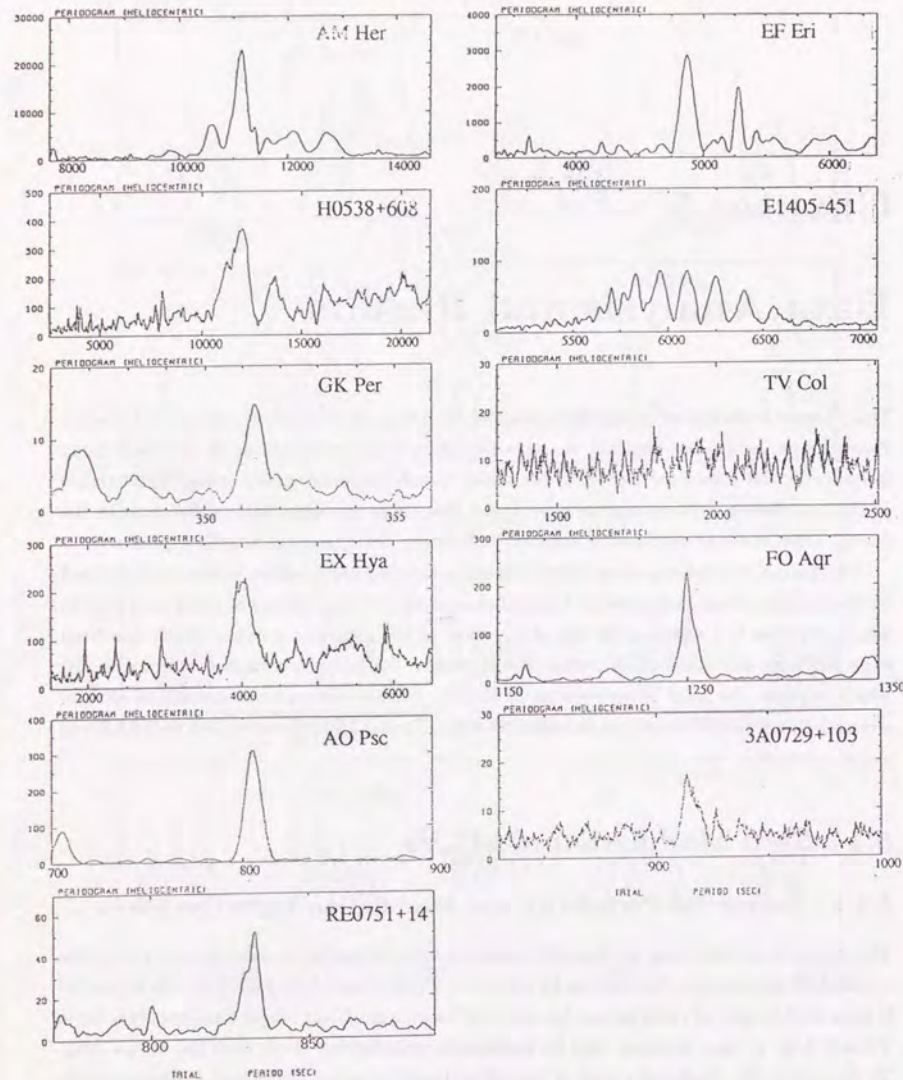
Figure 5.1: Reduced χ^2 values versus trial periods with the *Ginga* data. Light curves in 1.2–37.4 keV are used except RE0751+14 (3.5–37.4 keV) due to contamination of solar X-ray.

accuracy of the period determination of H0538+608. There are several χ^2 peaks of similar

heights in the diagram of E1405–451. These are cycle count aliases of the true rotation period due to a large data gap lasting nearly 2 days in the middle of the observation.

The derived rotational periods are listed in table 5.1 in comparison with the optical periods. The way of error estimation of the period, together with examination against spurious period detection with *Ginga* observations, is summarized in appendix A. The *Ginga* periods agree with the optical periods within errors.

Table 5.1: Rotational period of the white dwarf determined with *Ginga* and optical observations

Source	X-ray period (s)	Rotatinal period (s)
Polars		
AM Her	11150±70	11139.3
EF Eri	4870±30	4861.4
H0538+608	12000±190	11959.8
E1405–451	6090±20	6090.9
Intermediate Polars		
GK Per	351.3±0.1	351.34
TV Col	········	~1911
EX Hya	4020±50	4021.62
FO Aqr	1254.8±2.0	1254.45
AO Psc	805.9±1.9	805.20
3A0729+103	913.7±1.7	913.49
RE0751+14	833.2±1.2	~830

A periodic modulation at 13.89±0.02 minutes has been detected from RE0751+14 for the first time in hard X-rays, which strongly suggests that the source is an intermediate polar. In figure 5.2, the light curves folded at the optical rotational periods are shown for two spin cycles for 4 polars (AM Her, EF Eri, H0538+608, E1405–451) and 7 intermediate polars (GK Per in quiescence, TV Col, EX Hya, FO Aqr, AO Psc, 3A0729+103, RE0751+14) in three broad energy bands. In order to indicate spectral changes with the pulse phase, the ratios of the soft-band to the middle-band light curves are also shown.
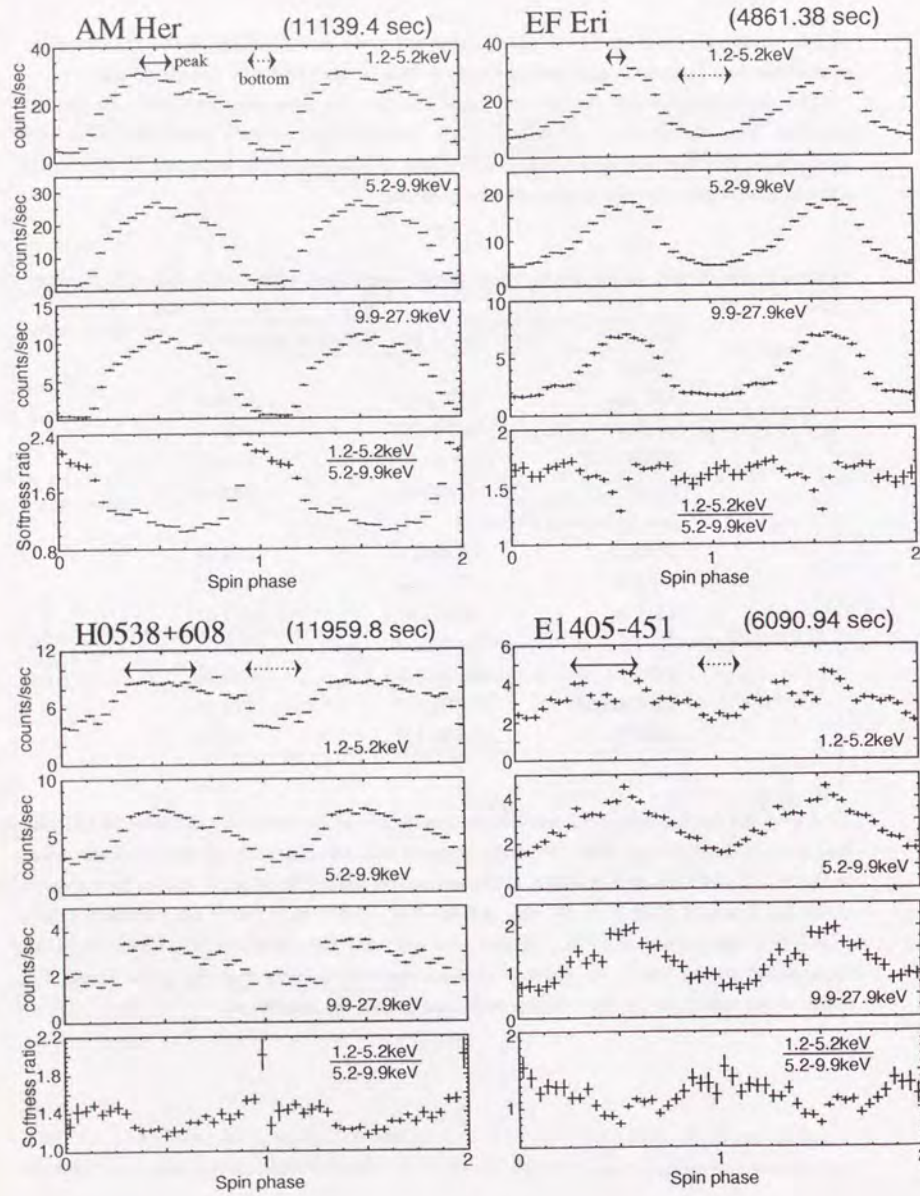
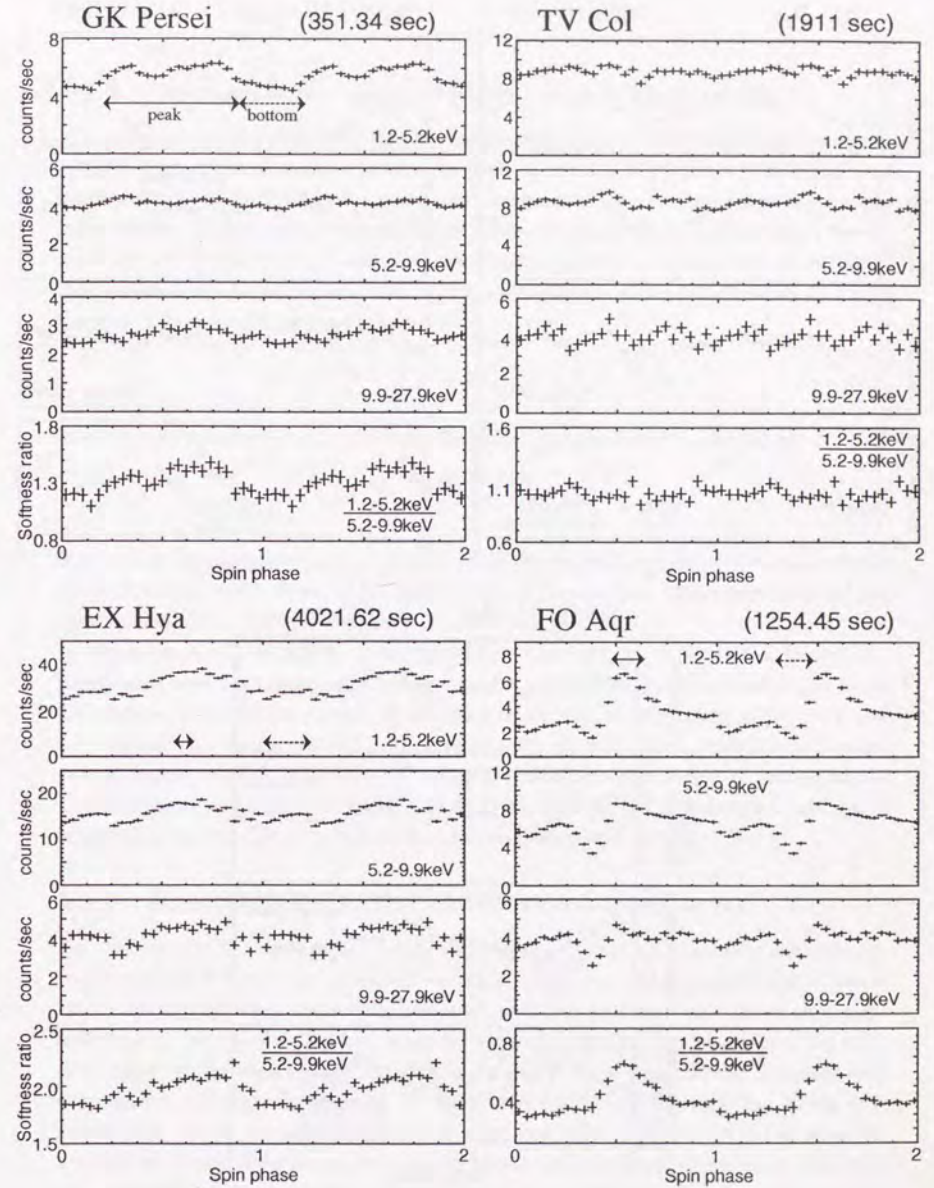Figure 5.2: Folded light curves of polars

Figure 5.2: Folded light curves of intermediate polars

AO Psc   (805.20 sec)

3A0729+103   (913.49 sec)

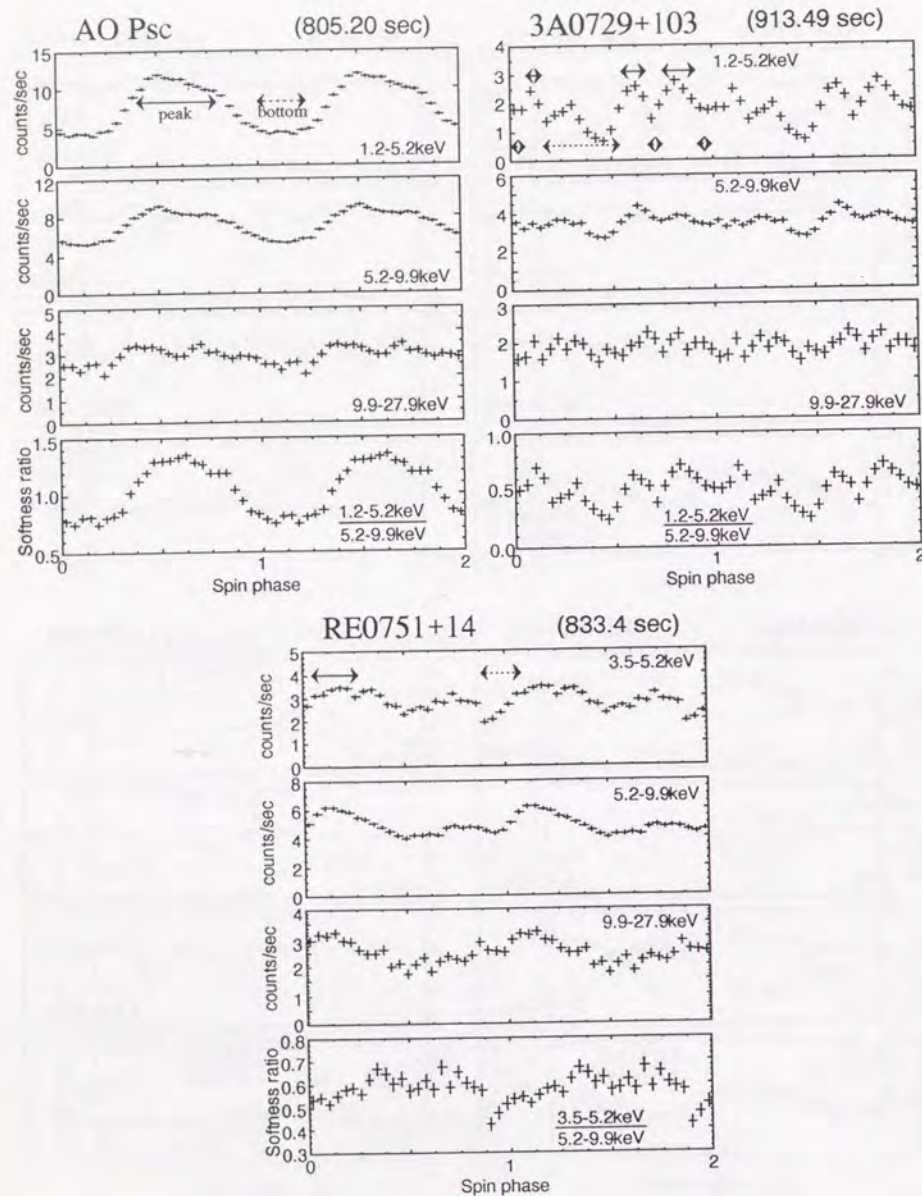RE0751+14   (833.4 sec)

Figure 5.2: Folded light curves of intermediate polars (cont'd)

5.1.2 Energy Dependence of Modulation Light Curves

It is easily noticed from figure 5.2 that the light curves of polars are basically single-peaked, whereas there are considerable variations in those of intermediate polars. In addition, it is suggested from figure 5.2 that the modulation amplitude of intermediate polars is generally larger in lower energy bands, whereas that of polars are rather energy independent or somewhat larger in higher energy bands. To evaluate these features quantitatively, we introduce Modulation Amplitude (MA) in terms of Fourier amplitudes. A periodic function $f(t)$ with a period P is expanded by Fourier series as

$$f(t) = \frac{a_0}{2} + \sum_{n=1}^{\infty} \left(a_n \cos \frac{2\pi n}{P} t + b_n \sin \frac{2\pi n}{P} t \right). \tag{5.1}$$

With Fourier amplitudes $\{a_n\}$ and $\{b_n\}$, the Modulation Amplitude is defined as

$$MA = \frac{2\sqrt{\sum_{n=1}^{n=2} (a_n^2 + b_n^2)}}{a_0}. \tag{5.2}$$

Notice that the summation in eq(5.2) ends up at the second harmonic. This is to evaluate the complexity of the shape of the light curves of intermediate polars and to avoid the contribution from statistical and aperiodic variations.

Applying eq.(5.1) and (5.2) to the folded light curves shown in figure 5.2, Modulation Amplitudes have been obtained as a function of X-ray energy. Results are shown in figure 5.3. Figure 5.4 shows the relation of MAs in two different energy bands, 1.2–5.2 keV and 9.9–14.0 keV. As clearly revealed in these figures, the MAs of intermediate polars decrease toward higher energies, while those of polars are relatively independent of energy, with a slight increase toward higher energies. The MAs of polars are generally larger than those of intermediate polars. These results confirm the suggestion made above.

5.1.3 Interpretation of the Modulation Light Curves

Here we attempt to interpret the results obtained in section 5.1.2, especially the clear differences between polars and intermediate polars. The modulation amplitudes of polars are on the average larger than 50%, and show weak energy dependence. Such an energy-independent, large modulation has been most naturally explained by the eclipse of the emission region by the white dwarf. In addition to this, a narrow dip around the pulse-peak is recognized mainly in lower energy bands in three polars (AM Her, EF Eri, E1405–451) out of four. These narrow dips have been attributed to the photoelectric absorption, for example for EF Eri (Beuermann et al. 1987), because of their energy dependence, which will be confirmed later. From these two observational results, it is likely that the emission region comes nearest to the line of sight at pulse-peak phases, and the dip is due to photoelectric absorption along the accretion column.
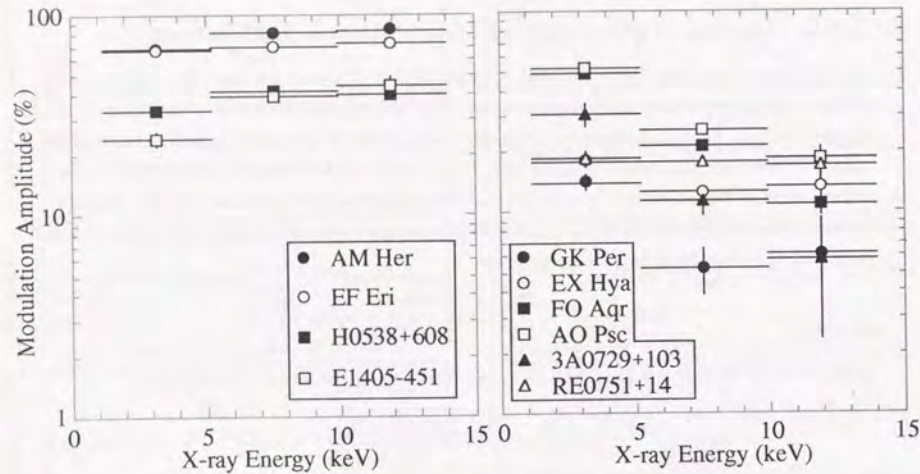
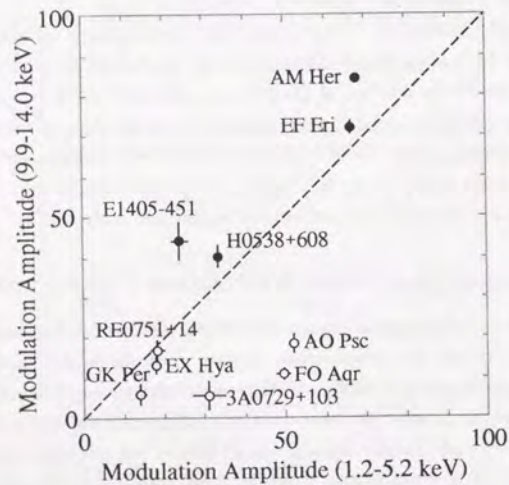Figure 5.3: Modulation Amplitude of polars and intermediate polars

Figure 5.4: Relation of Modulation Amplitude in 1.2–5.2 keV and 9.9-14.0 keV

In intermediate polars, on the other hand, the situation is a little more complicated. The modulation amplitude above 10keV is not more than 20%, which suggests relatively small

contribution to the spin modulation from the occultation of the white dwarf. Photoelectric absorption can qualitatively explain the energy dependence of the modulation of intermediate polars. In this case, the spectra are expected to undergo more absorption in the pulse-bottom phase, although there is no clear absorption dip in the light curves of intermediate polars. Notice that, however, this is not a unique possibility. For example, coexistence of a pulsating soft component and a stable harder component can also explain larger modulation amplitude in the lower energy band. Further investigation will be made through spin-phase spectral analysis in section 5.3.

5.2 Spin-phase Average Spectra of MCVs

5.2.1 Derivation of spectra

As we have background observations adjacent to the on-source observations for all the on-source observations listed in table 4.1, we can use Method I for background reduction from the on-source data. As explained in chapter 3, this method is in general reproduces accurate background counting rate. The spectra of MCVs are expected to be very hard, so that it is necessary to recover spectral information up to the highest possible energy band with enough reliability. Therefore, we exclude the data obtained in contact orbits from the spectral analysis because the LAC internal background is twice as high as in the remote orbits, and adopt SUD-sorting method for background subtraction. About one-fifth of the data is lost in this treatment. After background subtraction, the aspect correction is performed for the obtained spectra. To avoid large errors in this process, we discard the data with collimator transmission of less than 70%.

The spin-phase average spectra thus obtained are shown in figure 5.5 for all the sources listed in table 4.1. Throughout this thesis, we deal with photon spectra without deconvoluting the counter response function. These spectra have following qualitative characteristics. First, all these spectra are very hard. In fact, Ishida *et al.* (1991a, b) have already shown that the spectra of GK Per in quiescence and outburst and the spectra of H0538+608 are explained by the thermal bremsstrahlung model spectrum with temperature of 30–40keV. Second, most spectra shows a prominent line structure, probably the iron K-emission line, around 6–7keV. Finally, the shapes of the spectra below ∼6keV differ significantly source by source. Some spectra show clear low energy cutoff (GK Per in outburst and FO Aqr, for example) while others do not (EF Eri and GK Per in quiescence, for example). These features are quantitatively evaluated in the following subsections.
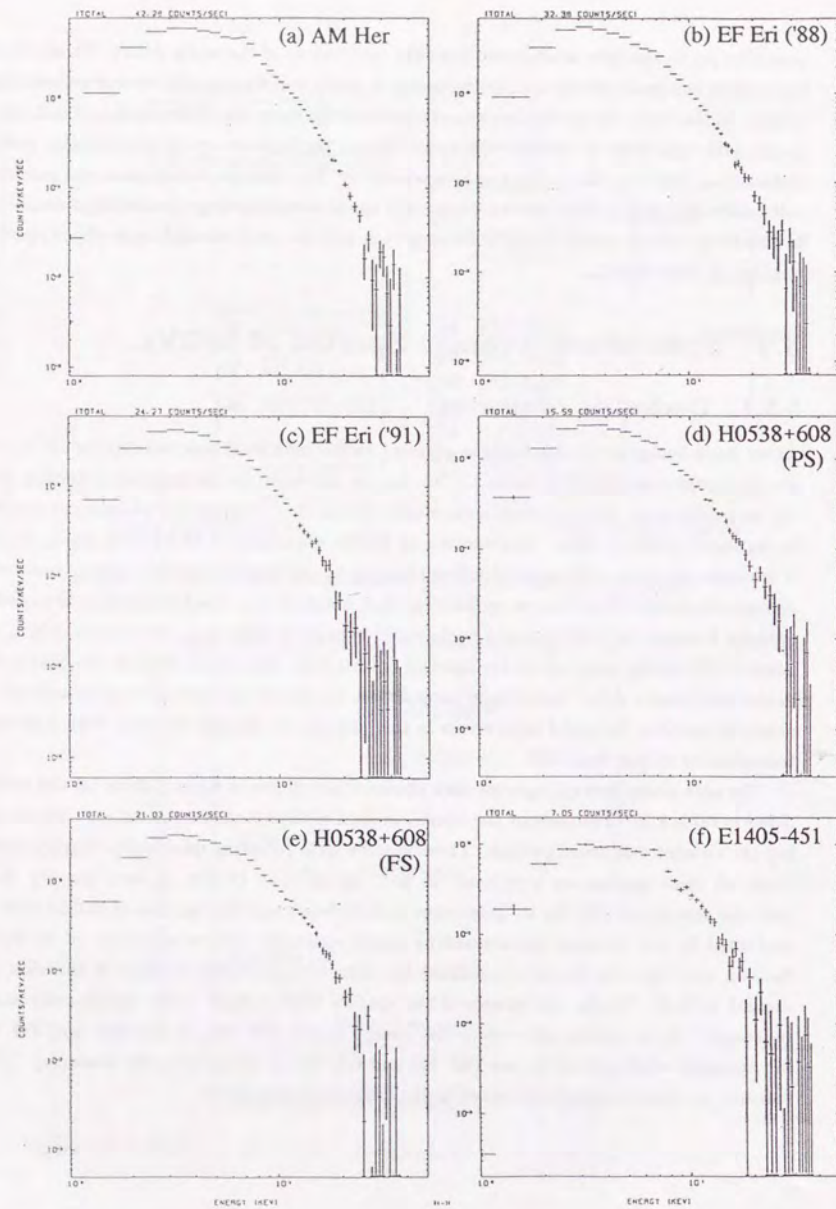
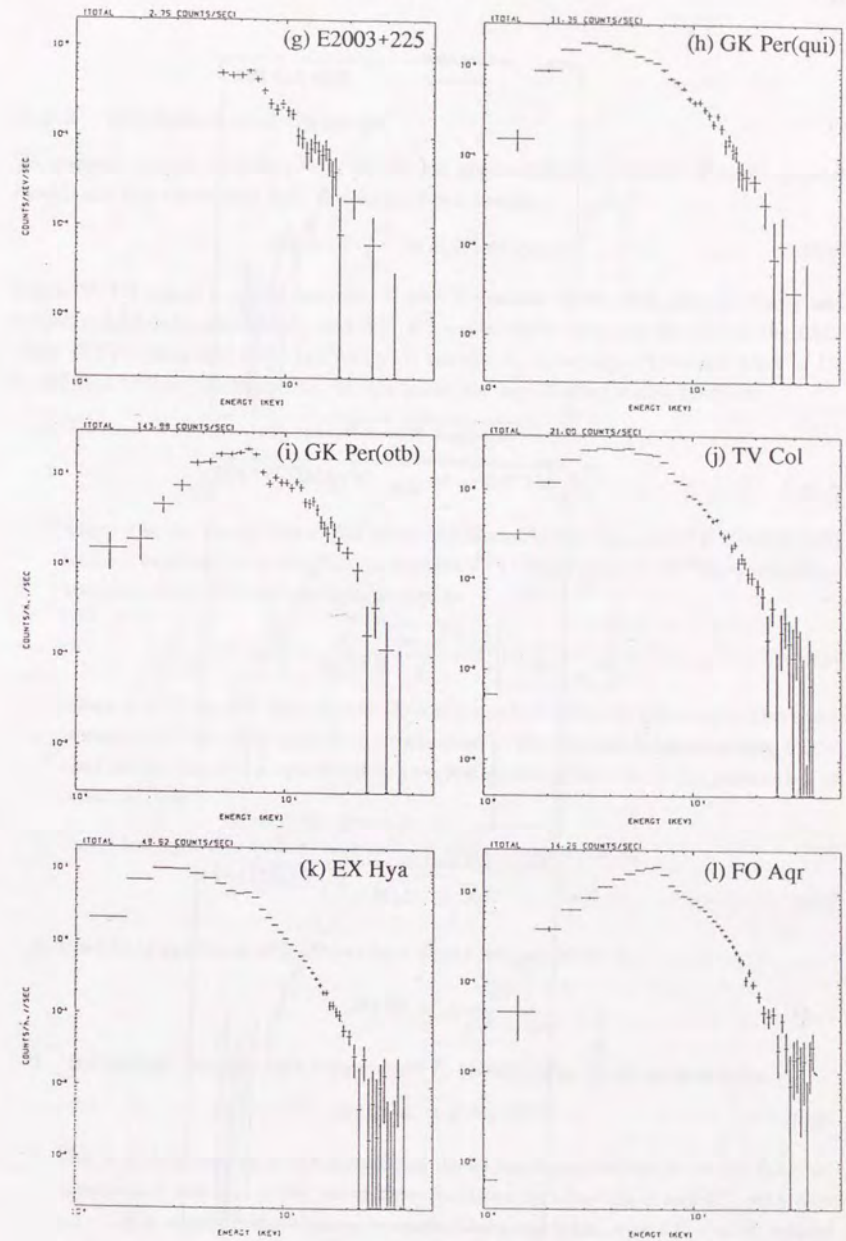Figure 5.5: Spin-phase averaged spectra of MCVs.

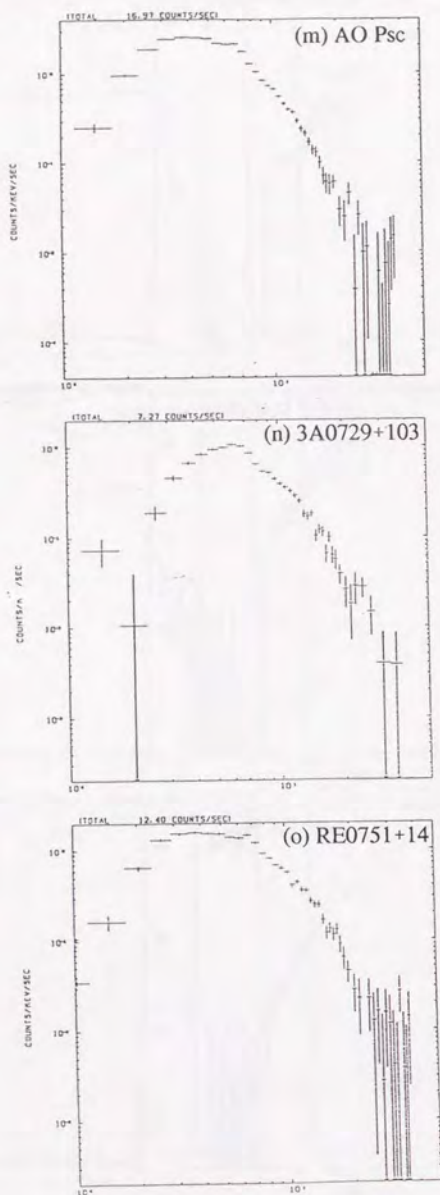Figure 5.5: Spin-phase averaged spectra of MCVs (cont'd).

Figure 5.5: Spin-phase averaged spectra of MCVs (cont'd).

5.2.2   Evaluation of Spectra

To evaluate spectra quantitatively, we use the spectral fitting method. Photon spectral models are first convoluted with the response function as

$$F(E) = \int_0^\infty R(E, E')\, M(E')\, dE', \tag{5.3}$$

where $M(E')$ means a model function, E' and E denotes the incident photon energy and output pulse height, respectively, and $R(E, E')$ represents the response function of the LAC. Then $F(E)$ is compared with data and χ^2 is calculated, including a systematic error of 1% in addition to the statistical error. In this thesis, we use following model functions.

1. Thermal bremsstrahlung spectrum with temperature T;

$$M(E) = A\, T^{-1/2}\, e^{-E/kT}\, \frac{g(E, kT)}{E}, \tag{5.4}$$

where g is the Gaunt factor. We adopt the Gaunt factor calculated by Gould (1980) which is expected to be accurate for plasmas with temperature of 10^{7-8}K. A represents the normalization factor and is expressed as

$$A = \frac{4}{3\pi D^2} \sqrt{\frac{2m_e c^4}{\pi}} \alpha^3 \Lambda^2 \left(n_e \sum Z^2 n_Z V \right), \tag{5.5}$$

where $\alpha = e^2/\hbar c$, $\Lambda = \hbar/m_e c^2$, and D represents the distance to the source. Therefore, it should be remarked that the normalization of the thermal bremsstrahlung model used in this thesis is proportional to so-called emission measure in the parenthesis of equation (5.5).

2. Power-law spectrum with photon index α and normalization A;

$$M(E) = A\, E^{-\alpha}. \tag{5.6}$$

3. Blackbody spectrum with temperature T and normalization A;

$$M(E) = A\, \frac{E^2}{e^{\frac{E}{kT}} - 1}. \tag{5.7}$$

4. "Boltzmann" function with temperature T, photon index α and normalization A;

$$M(E) = A\, E^{-\alpha}\, e^{-E/kT}. \tag{5.8}$$

This is mainly used as a rather empirical model for the continuum since this function approximate any one of the above three functions by adjusting α and kT; with $\alpha \sim 1.3 - 1.4$ it approximates thermal bremsstrahlung spectrum, with $kT = \infty$ it reduces to the power-law spectrum, and with $\alpha = -2$ it becomes the Wien spectrum which represents the blackbody spectrum in the $E \gg kT$ regime.

5. Gauss function with center energy E_0, standard deviation σ and normalization A;

$$M(E) = \frac{A}{\sqrt{2\pi}\sigma} e^{-\frac{(E-E_0)^2}{2\sigma^2}}, \tag{5.9}$$

This function is used for representing the iron line.

6. Photoelectric absorption with equivalent hydrogen column density N_H;

$$M(E) = e^{-N_H\sigma(E)}, \tag{5.10}$$

where $\sigma(E)$ means the cross section of photoelectric absorption calculated by Morrison & McCammon (1977) for material with solar abundances. A continuum function is multiplied by this function before convolution with the detector response.

5.2.3 Single Component Fits

To begin with, we try to evaluate the spectra shown in figure 5.5 with spectral models composed of a single continuum model with photoelectric absorption. We use the thermal bremsstrahlung model or the power-law model as a continuum component. Resultant χ^2 values are listed in the second and the third columns of table 5.2. As easily seen from this table, the thermal bremsstrahlung model generally gives better fits to the observed spectra. Resultant χ^2 values indicate, however, that the fits are not acceptable. In figure 5.6, some examples of fits with thermal bremsstrahlung model are shown. There is a clear hump around 6–7keV in the fit residuals, indicating presence of the iron emission line. We then include a narrow (0.1keV FWHM) Gaussian line in the fit with intensity and central energy set free. As listed in the last column of table 5.2, this thermal bremsstrahlung plus a Gaussian line model has given significantly improved fits for all the spectra. Hereafter we refer to this model as "Model-1". Reduced χ^2 value corresponding to the 90% confidence level is 1.33 for the degree of freedom of 30. Fits have therefore been acceptable for 6 out of 15 spectra at the 90% confidence level; EF Eri ('88) and ('91), H0538+608 in the flaring state (FS), E2003+225, GK Per in quiescence and 3A0729+103. These sources, with the spin-phase average spectrum represented well with Model-1, are hereafter referred to as "Group-1" sources, and the others as "Group-2" sources. (Notice that GK Per in quiescence and H0538+608 in FS are included in Group-1, whereas GK Per in outburst and H0538+608 in PS belong to Group-2.) In figure 5.7, the results of the fits with Model-1 are shown for all the spectra together with fit residuals. The fit parameters for the Group-1 sources are summarized in table 5.3.

A remark should be made here for EX Hya. A thin thermal bremsstrahlung with iron K_α line gives χ^2_ν value of 1.83 which is not acceptable. Inspecting the residuals of the fit (figure 5.7), a positive and sharp structure remains in a few energy bins around 8 keV. Therefore, we include another Gaussian line in the model. With this model, reduced χ^2 value is significantly reduced to 1.09. Therefore we include EX Hya in Group-1. The resultant

Table 5.2: Reduced χ^2 values with a single continuum models. The number in parenthesis gives degree of freedom.

Source	No iron line		With Iron line
	Th. Brems.	Power-law	Th. Brems
Polars			
AM Her	52.6 (34)	74.0 (34)	9.31 (32)
EF Eri ('88)	8.24 (34)	13.8 (34)	1.06 (31)
EF Eri ('91)	4.65 (34)	8.78 (34)	1.06 (31)
H0538+608 (PS)	4.10 (33)	5.68 (33)	1.45 (31)
H0538+608 (FS)	4.39 (33)	8.48 (33)	0.81 (31)
E1405–451	9.03 (33)	10.4 (33)	1.77 (31)
E2003+225	1.96 (30)	2.08 (30)	0.88 (28)
Intermediate Polars			
GK Per (Qui.)	1.32 (31)	1.67 (31)	0.74 (29)
GK Per (Outb.)	2.55 (31)	2.55 (31)	1.63 (29)
TV Col	9.07 (31)	10.7 (31)	2.49 (29)
EX Hya	31.0 (33)	50.4 (33)	1.83 (31)
FO Aqr	19.5 (34)	20.9 (34)	9.08 (32)
AO Psc	16.1 (29)	22.0 (29)	2.13 (27)
3A0729+103	3.28 (34)	3.34 (34)	1.12 (32)
RE0751+14	6.07 (33)	7.02 (33)	1.71 (31)

center energies of the two lines are 6.78 ± 0.04 keV and 8.20 ± 0.27 keV, and their line equivalent widths are ~ 640 eV and ~ 130 eV, respectively. These values are consistent with those of K_α and K_β line expected from the plasma in ionization equilibrium (Okumura *et al.* 1988). The result of the fitting including two Gaussian lines is shown in figure 5.8 for EX Hya. As a result, 7 spectra out of 15 can be fitted by Model-1 including EX Hya. On the other hand, fits for the spectra of Group-2 sources are not improved by including another line. Therefore, it seems that EX Hya is rather exceptional. We will return to this problem in section 5.6 after establishing a spectral model in section 5.3 and 5.4 which explains all the spectra of MCVs.
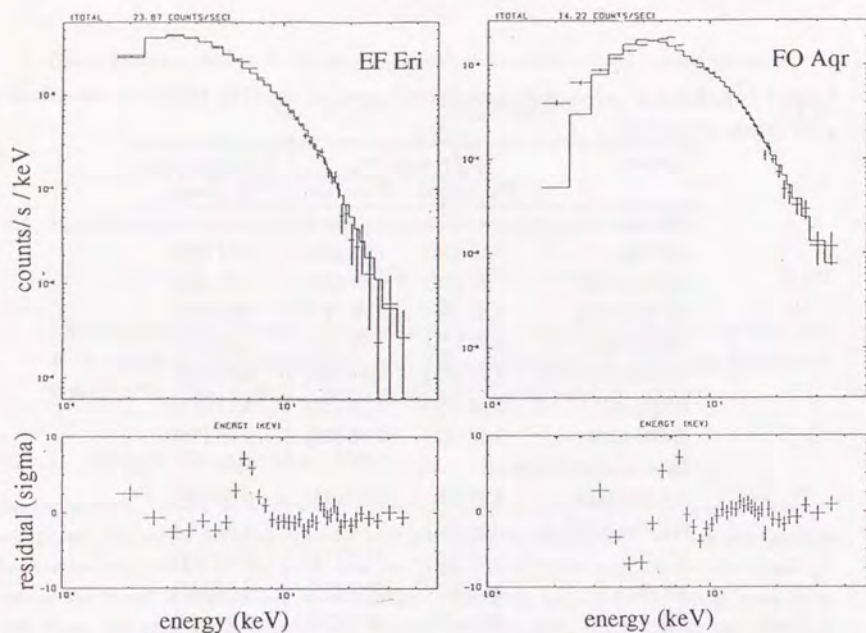
Figure 5.6: Examples of the fits with thermal bremsstrahlung model (without line). Bottom panels show fit residuals in units of standard deviation.

Table 5.3: Fit parameters with thermal bremsstrahlung model.

Name of Source	Continuum Parameters			Iron Line Parameters			χ^2_ν (dof)
	Norm.[a]	Temp.[b]	$\log N_H$ [c]	Int.[d]	Energy[e]	E.W.[f]	
EF Eri ('88)	1.17±0.02	16.9±0.6	21.7±0.08	2.1±0.2	6.76±0.07	310±30	1.06 (32)
EF Eri ('91)	0.86±0.02	16.9±1.0	21.5±0.15	1.6±0.2	6.71±0.09	320±50	1.06 (32)
H0538+608 (FS)	0.78±0.01	25.9±1.5	21.8±0.07	1.1±0.2	6.59±0.10	210±30	0.81 (26)
E2003+225	0.14±0.01	41.9±8.4	< 22.5	0.7±0.1	6.70±0.09	680±90	0.88 (22)
GK Per (quis.)	0.39±0.02	32.0±6.1	21.9±0.14	0.7±0.2	6.49±0.24	250±90	0.74 (29)
EX Hya	2.00±0.02	8.9±0.2	< 20.5	5.6±0.3	6.78±0.04	640±40	1.09 (29)
				0.8±0.3	8.20±0.27	130±40 [g]	
3A0729+103	0.41±0.03	28.9±5.8	23.1±0.04	1.0±0.2	6.50±0.10	410±80	1.12 (32)

a: Normalization in unit of 10^{-2}photons/sec/cm^2/keV

b: Temperature of thermal bremsstrahlung in keV

c: Unit of N_H is cm^{-2}

d: Line intensity in unit of 10^{-4}photons/sec/cm^2

e: Line center energy in keV

f: Line equivalent width in eV

g: Row for K_β line parameters

Figure 5.7: Spectral fitting with the thermal bremsstrahlung model including an iron line.

Figure 5.7: Spectral fitting with the thermal bremsstrahlung model including an iron line.

Figure 5.7: Spectral fitting with the thermal bremsstrahlung model including an iron line.
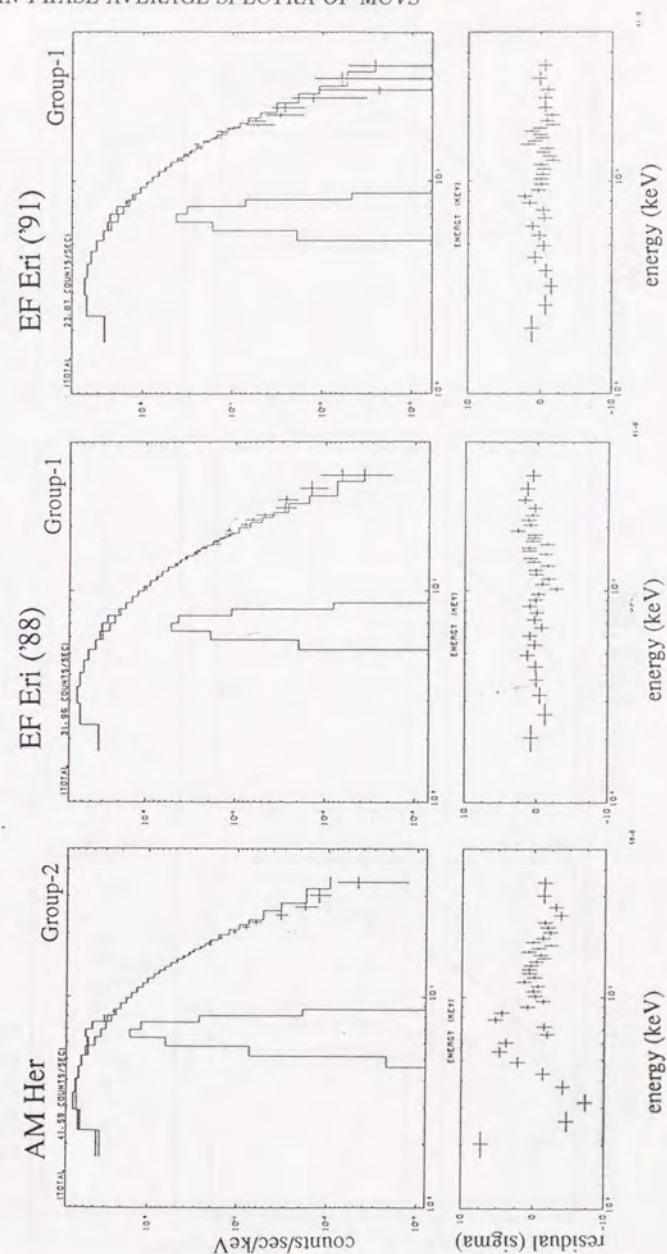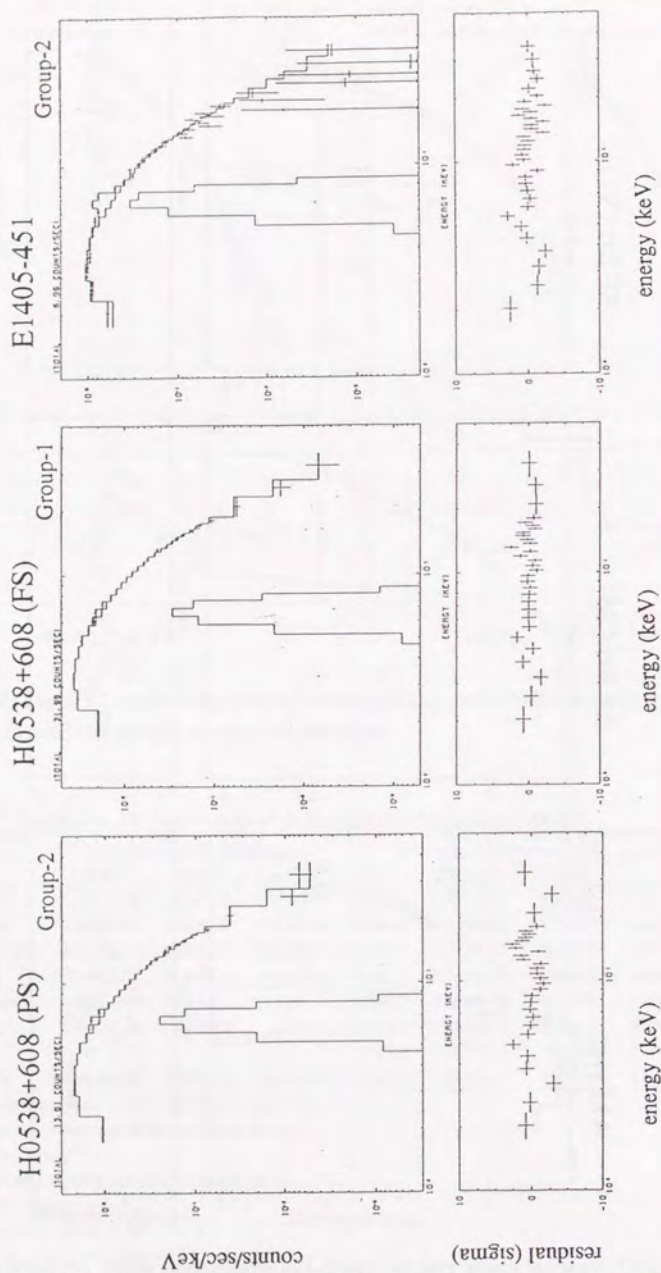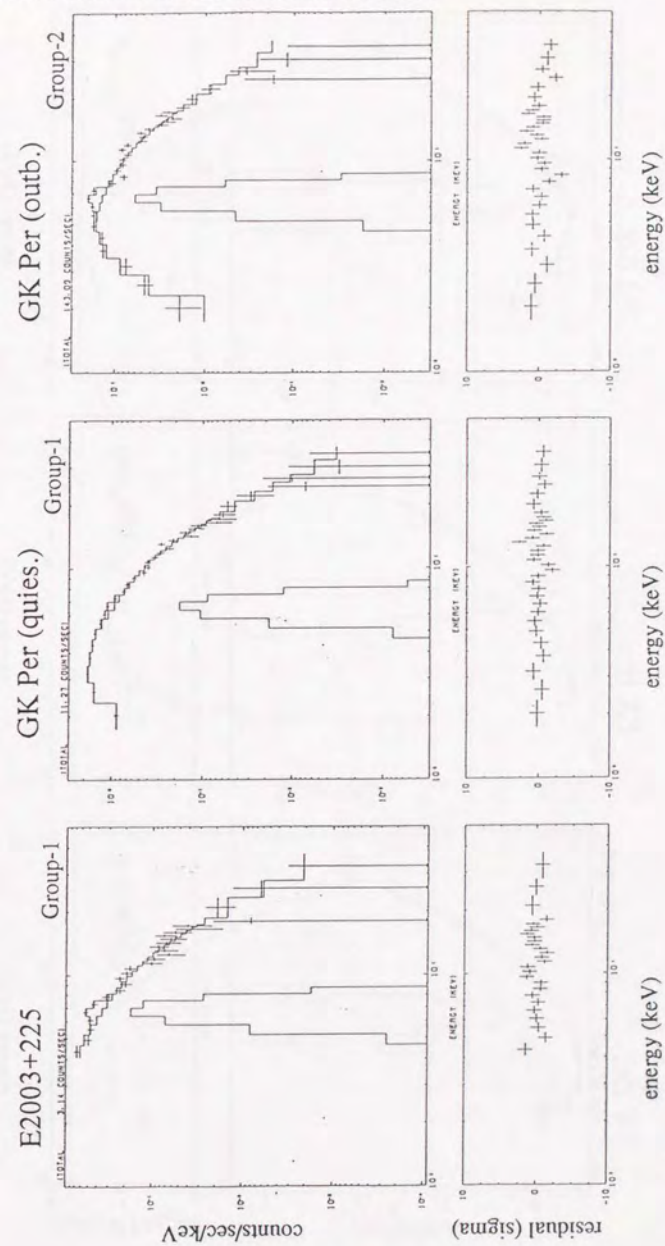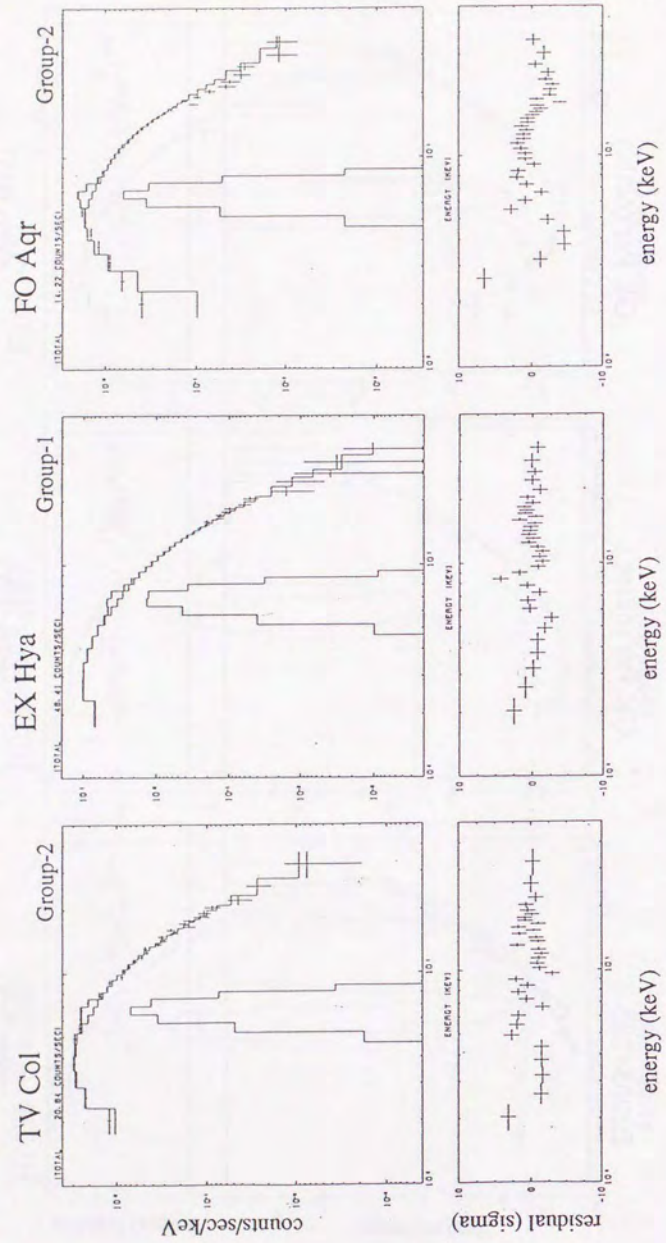
Figure 5.7: Spectral fitting with the thermal bremsstrahlung model including an iron line.

Figure 5.7: Spectral fitting with the thermal bremsstrahlung model including an iron line.
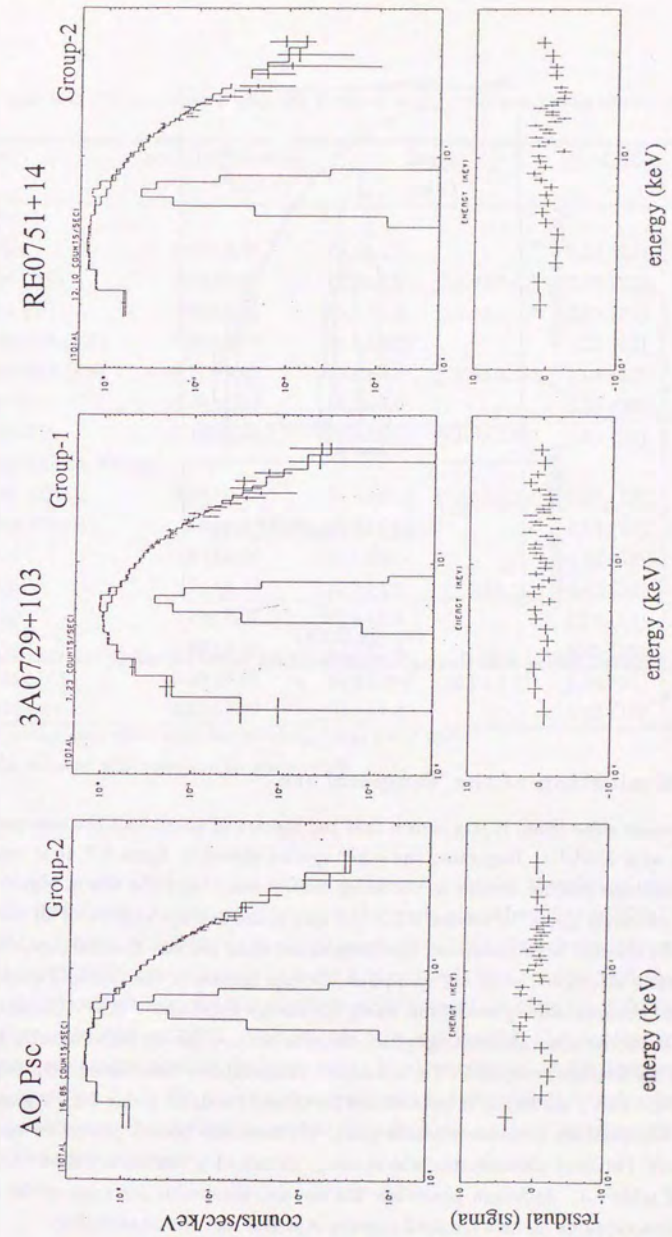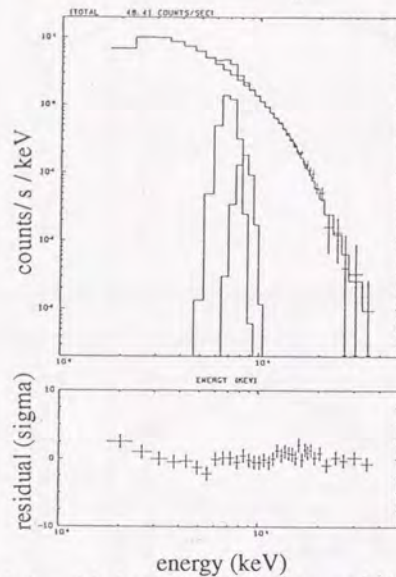
energy (keV)

Figure 5.8: Spectral fitting with thermal bremsstrahlung model including two Gaussian lines for EX Hya.

5.2.4   Evaluation of the Temperature

In the previous subsection, it was shown that the spectra of about half the sources can be fitted well with Model-1. Inspecting the other spectra shown in figure 5.7, it is recognized that the residuals mainly remain in the lower energy band, and the fits in higher energy range are relatively good. In section 5.2.3, the spin-phase average spectra of all the MCVs ex-favoured the thermal bremsstrahlung spectrum rather than the non-thermal power-law. We have therefore attempted to fit the spin-phase average spectra of the Group-2 sources with the thermal bremsstrahlung model but using the energy band above 10keV (in this energy band, photoelectric absorption is negligible). Results of these fits are listed in table 5.4. The fits are on the average acceptable. For references, temperatures determined with full energy range (1.2–37.4keV) are shown in parentheses for Group-1 sources (table 5.3). Agreement of these two temperature determinations is good. We have also tried a power-law continuum above 10keV (without photoelectric absorption). Obtained χ^2 values are listed in the last column of table 5.4. Although power-law fits are also acceptable for most of the sources, they are unacceptable for two Group-2 sources, AM Her and H0538+608(PS).

Results so far obtained strongly support the viewpoint that hard X-ray emission of MCVs is of thermal origin. Obtained temperatures range from 10 to 40keV, which roughly corre-

Table 5.4: Fit parameters with the thermal bremsstrahlung model above 10keV.

Source	Norm.(10^{-2}photons s^{-1} cm^{-2} keV^{-1})	Temp. (keV)		χ^2_ν (d.o.f.)	χ^2_ν (d.o.f) (PL)[b]
Polars					
AM Her	1.67±0.09	19.4±1.7		1.13 (18)	2.36 (18)
EF Eri ('88)	1.01±0.07	21.8±2.9	(16.9±0.6)[a]	0.69 (21)	0.79 (21)
EF Eri ('91)	0.90±0.11	15.3±3.0	(16.9±0.6)[a]	0.79 (21)	0.95 (21)
H0538+608 (PS)	0.50±0.05	39.5±10.9		1.22 (20)	1.39 (20)
H0538+608 (FS)	0.77±0.05	25.6±3.8	(25.9±1.5)[a]	1.05 (20)	1.54 (20)
E1405–451	0.32±0.13	16.9±6.0		0.88 (20)	0.92 (20)
E2003+225	0.15±0.05	31.4±55.9	(41.9±8.4)[a]	1.01 (21)	1.01 (21)
Intermediate Polars					
GK Per (Qui.)	0.38±0.07	34.3±21.2	(32.0±6.1)[a]	0.87 (18)	0.94 (18)
GK Per (Outb.)	8.0±1.6	53.6±85.7		1.04 (15)	1.07 (15)
TV Col	0.67±0.06	51.1±27.4		0.92 (18)	1.01 (18)
EX Hya	1.73±0.18	10.3±1.0	(8.9±0.2)[a]	0.42 (20)	0.76 (20)
FO Aqr	0.79±0.07	33.9±8.4		1.08 (18)	1.22 (18)
AO Psc	0.80±0.11	13.9±2.4		0.45 (16)	0.59 (16)
3A0729+103	0.39±0.08	36.3±15.8	(28.9±5.8)[a]	1.30 (21)	1.34 (21)
RE0751+14	0.62±0.15	20.4±7.8		1.09 (17)	1.13 (17)

a: Temperature determined using the full energy range 1.2-37.4keV.

b: Results obtained with power-law fits above 10keV.

spond to the graviational potential energy with matter of solar abundances accreting onto the white dwarf surface. There still remains, however, a problem that Model-1 cannot explain all the spectra in full energy band. As mentioned above, discrepancy between the data and the model prediction is mainly in lower energy band. It is possible that the absorbing column density exihibits significant distribution, as pointed out from the *EXOSAT* observations (Norton & Watson 1989). Alternatively, it is also possible that another independent continuum component exists in the lower energy band, reminiscent of the comments made at the end of section 5.1.3. We cannot give a conclusion to this problem by spin-phase average spectroscopy alone. We further proceed to the spin-phase-resolved spectroscopy, and later come back to this problem.

5.3   Spin-phase Spectroscopy of MCVs

5.3.1   Spectral Variation with Spin Phase of the White Dwarf

As mentioned in the previous two sections, spectral shape varies significantly with spin phase of the white dwarf especially in intermediate polars. It is important to examine this variation with spin-phase-resolved spectroscopy to clarify the origin of the spin modulations of MCVs and to explain the complexity of spin-phase average spectra. We have made the following data selection for spin-phase spectroscopy. We exclude TV Col from the analysis because pulsation is not detected. We also exclude E2003+225 because it is too faint for the data to be divided any further. As mentioned in section 4.3.1, only the quiescent data of GK Per is available for spin-phase spectroscopy. Also, only the data in the pulsing state (PS; see section 4.2.3) are used for H0538+608. As for EF Eri, the two sets of data (observation performed in 1988 and 1991) are merged in view of statistics because the two spin-phase average spectra show no difference in shape (figure 5.7 and table 5.3) in spite of a factor ∼1.5 intensity difference. As mentioned in section 4.3.8, about two-thirds of RE0751+14 data are contaminated by solar X-rays. To retain statistics, we use all the data but discard eneregy band below 4keV. After these selections, 10 sources remain for spin-phase spectroscopy.

As suggested in subsection 5.1.3, spectral shape changes with spin phase especially in intermediate polars, which may be attributed to the modulation in the low energy absorption or the appearence of additional soft component. As shown in figure 5.2, the softness ratio is maximum at the pulse-peak (pulse-bottom) and minimum at the pulse-bottom (pulse-peak) in polar (intermediate polar). Therefore, it is expected that essence of the intensity modulation is best investigated through comparison between the pulse-peak and the pulse-bottom spectra. In this thesis, we examine the pulse-peak and the pulse-bottom spectra for the 10 sources mentioned above, and possible from statistical point of view, we further examine the rise and decline phases for some particular sources.

In figure 5.2, phase intervals specifying the pulse-peak and the pulse-bottom are shown by arrows. Obtained spectra for these phase intervals are superposed in figure 5.9 together with the ratio of the count rates in each spectral channel of the two spectra (hereafter referred to as SC-ratio). The spectra are aspect-corrected after background subtraction by SUD-sorting method. Here we reconfirm the results derived in subsections 5.1.2 and 5.1.3 that

- the modulation amplitude of polars is on the average larger than that of intermediate polars,

- the modulation amplitude of polars is larger in higher energy bands whereas that of intermediate polars increases toward lower energies, or equivalently, the spectra of polars are softer in the pulse-bottom phases whereas those of intermediate polars are so in the pulse-peak phase.
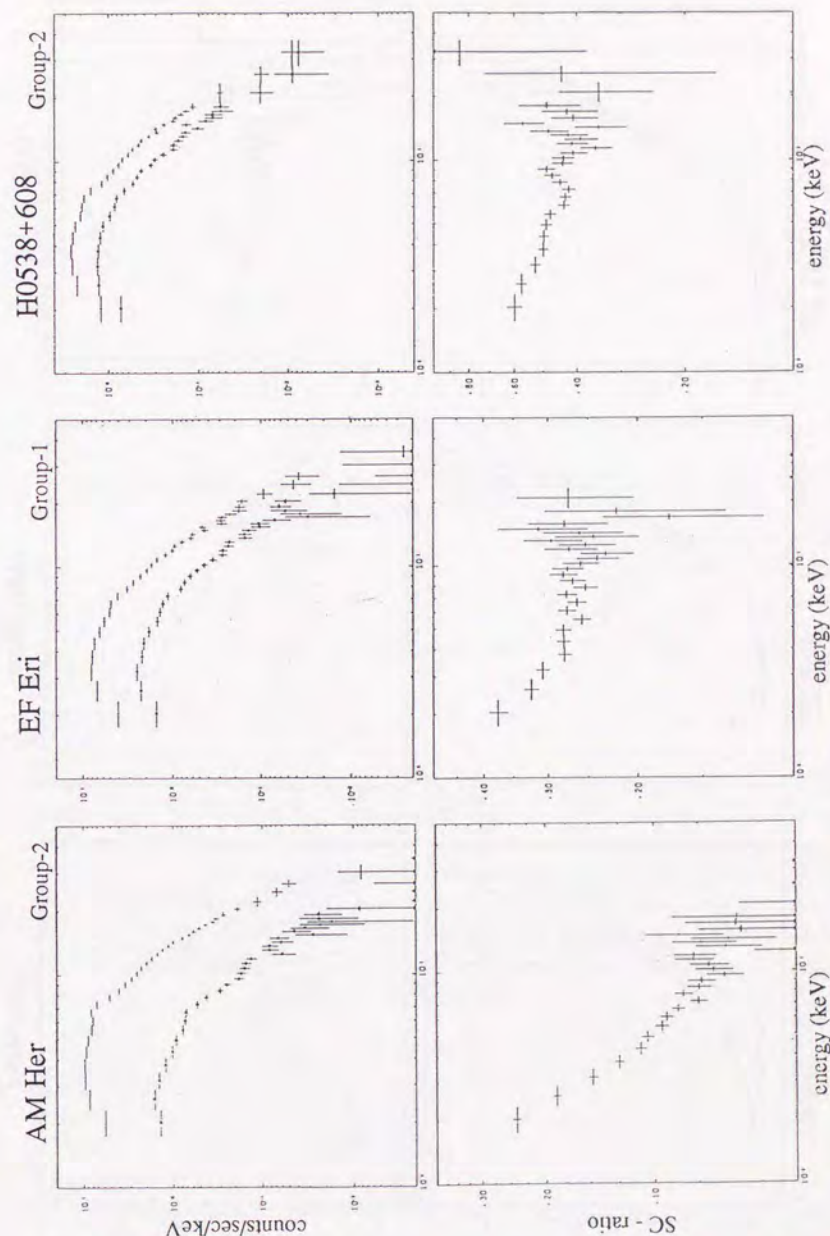
Figure 5.9: Pulse peak and pulse-bottom spectra, and the ratios of count rate in each spectral channel.
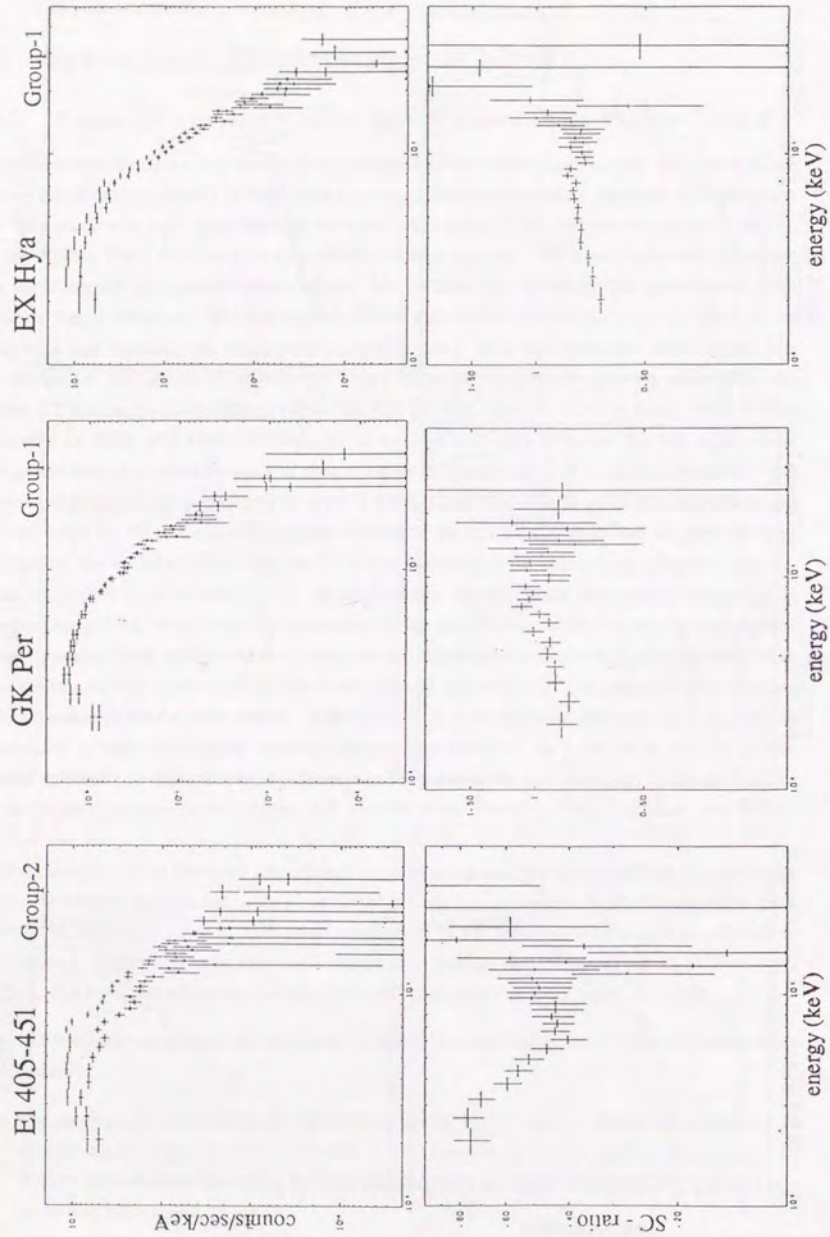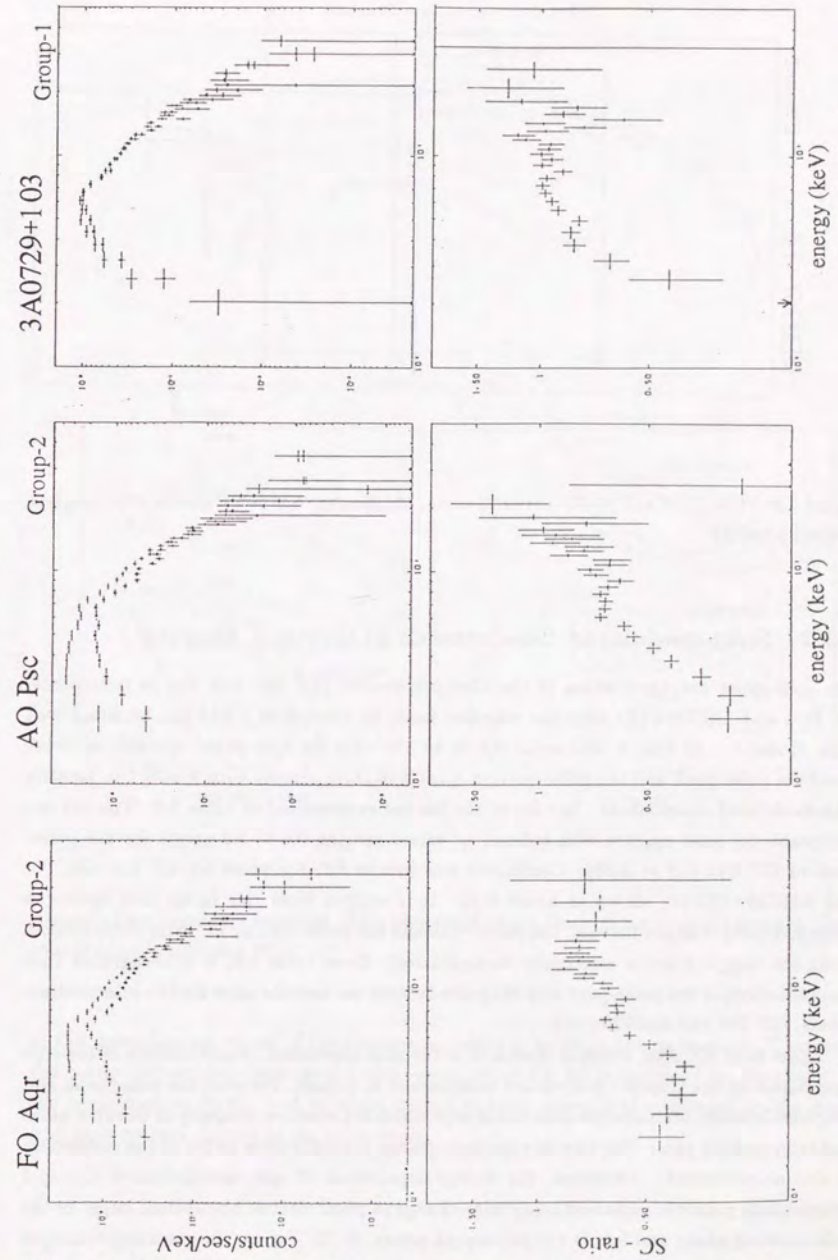
Figure 5.9: Pulse peak and pulse-bottom spectra, and the ratios of count rate in each spectral channel (cont'd).

Figure 5.9: Pulse peak and pulse-bottom spectra, and the ratios of count rate in each spectral channel (cont'd).
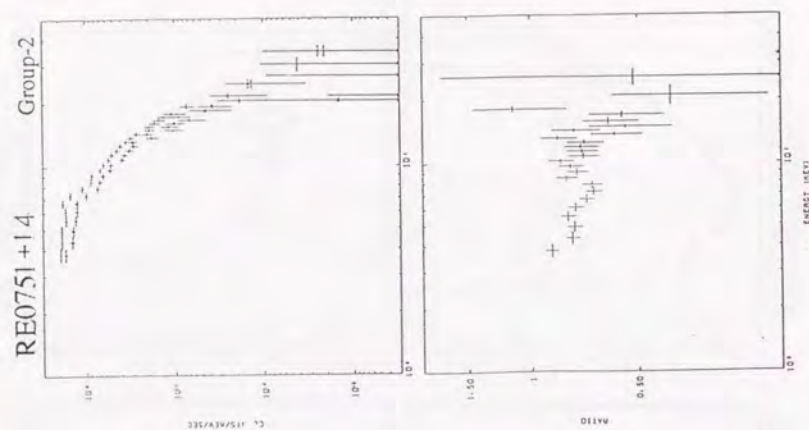
Figure 5.9: Pulse peak and pulse-bottom spectra, and the ratios of count rate in each spectral channel (cont'd).

5.3.2 Spin-modulated Components of Group-1 Sources

The spin-phase average spectra of the Group-1 sources (EF Eri, GK Per in quiescence, EX Hya and 3A0729+103 after the selection made in subsection 5.3.1) can be fitted well with Model 1. As this is also expected to be the case for spin-phase spectra, we have fitted the pulse-peak and the pulse-bottom spectra of these sources with Model 1 to identify spin-modulated components. Results of the fits are summarized in table 5.5. The fits are acceptable for most spectra with reduced χ^2 values ranging 0.6 to 1.2 except for the pulse-peak of EX Hya ($\chi^2_\nu = 1.56$). Confidence contours in kT–N_H plane for EF Eri, GK Per and 3A0729+103 are shown in figure 5.10. It is evident from this figure that hydrogen column density changes between the pulse-peak and the pulse-bottom for these three sources while the temperature is essentially unmodulated. From table 5.5, it is recognized that normalizations of the pulse-peak and the pulse-bottom are also the same for two intermediate polars, GK Per and 3A0729+103.

Apart from EX Hya, which is discussed in the next subsection, characteristics of the spin modulation of the Group-1 sources are summarized as follows. Between the pulse-peak and the pulse-bottom, temperature does not change which is a common property of Group-1 polar and intermediate polar. For two intermediate polars, normalization factor of the continuum is also unmodulated. Therefore, the energy dependence of spin modulation of Group-1 intermediate polars is explained solely with change in photoelectric absorption, larger in the pulse-bottom phase and less in the pulse-peak phase. In EF Eri, on the contrary, hydrogen column density is larger in the pulse-peak. This is, however, surpassed by a larger change
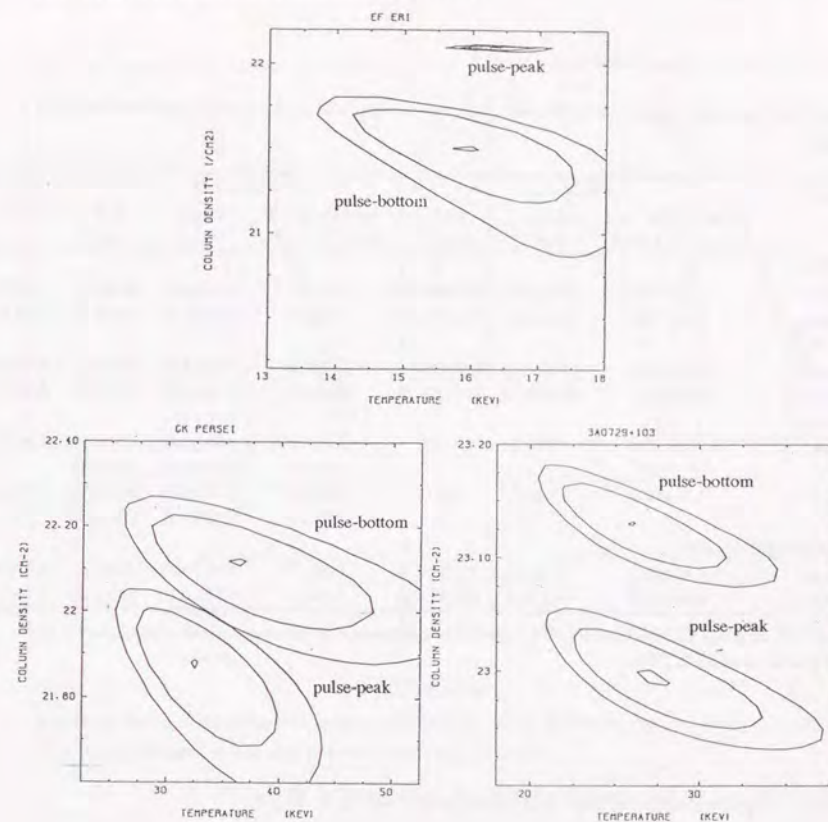
Figure 5.10: Confidence contours of the spectral fit with Model-1 for Group-1 sources. Contour levels are 68% and 90%.

in the normalization factor of the continuum, which is larger in the pulse-peak. Therefore, the energy-independent large modulation amplitude of EF Eri is explained by the change in the normalization factor, and its slight decline in lower energies is attributed to the larger hydrogen column density in the pulse-peak.

Table 5.5: Best fit paramaters for the pulse-peak and the pulse-bottom spectrum with Model-1.

Source	Continuum			Iron line			χ^2_ν
	Norm. (10^{-4}phs s^{-1} cm^{-2} keV^{-1})	Temp. (keV)	$\log N_H$ (cm^{-2})	Intensity (10^{-2} phs s^{-1} cm^{-2})	Energy (keV)	E.W. (eV)	(d.o.f.)
EF Eri							
(peak)	1.96±0.04	16.5±0.8	22.09±0.04	2.9±0.4	6.69±0.10	257± 40	1.27(32)
(bottom)	0.52±0.02	15.7±1.8	21.55±0.26	0.8±0.3	6.69±0.20	278± 90	0.82(32)
GK Per							
(peak)	0.39±0.02	32.5± 6.7	21.87±0.16	0.6±0.3	6.41±0.25	241± 90	0.63(29)
(bottom)	0.38±0.02	36.4±11.0	22.11±0.15	0.8±0.3	6.81±0.23	332±130	0.89(29)
EX Hya[a]							
(peak)	2.46±0.01	8.0±0.1	<20.5	6.0±0.2	6.82±0.03	618± 23	1.56(29)
				0.9±0.2	8.54±0.15	156± 30	
(bottom)	1.74±0.06	9.1±0.5	<20.5	4.8±0.8	6.74±0.12	620±100	1.02(29)
				1.1±0.7	7.83±0.47	199±130	
3A0729+103							
(peak)	0.42±0.03	27.4±6.1	22.99±0.05	0.9±0.2	6.38±0.13	363± 90	0.96(26)
(bottom)	0.42±0.03	26.2±5.0	23.13±0.04	1.0±0.2	6.50±0.10	440± 90	1.22(26)

a: Both K_α and K_β line are included. The upper row corresponds to the parameters for K_α line and the lower row to those for K_β line.

5.3.3 Spin-modulated Components of EX Hya

The best fit parameters for the pulse-peak and the pulse-bottom spectrum of EX Hya are also listed in table 5.5. Unlike spectra of the other Group-1 sources, the pulse-peak spectrum cannot be fitted with Model 1. In figure 5.11(a), we show the result of spectral fit to the pulse-peak with Model-1 (two iron lines). From this figure, it is noticed that residuals concentrate on the energy band below 6keV. We have carefully checked the contamination of solar X-rays and the reflection from the earth illuminated by the sun, but these possibilities are rejected. Therefore, this component is intrinsic to EX Hya. Utilizing the flat SC-ratio in higher energies, it is expected that we can extract a soft component responsible for this residual by taking difference between the pulse-peak and the pulse-bottom spectra after normalizing count rates in higher energy channels. We have normalized both spectra so that 9.3–37.2keV count rates become equal, and made a difference spectrum. Since the soft component is prominent only in several lowest energy bins, it is fitted well with various models, for example, thermal bremsstrahlung, blackbody with temperature less than 1keV, or power-law with photon index of ~ 3, with almost the same reduced χ^2 values of ~ 0.5.

Therefore we have fitted the pulse-peak spectrum of EX Hya with Model-1 plus black-
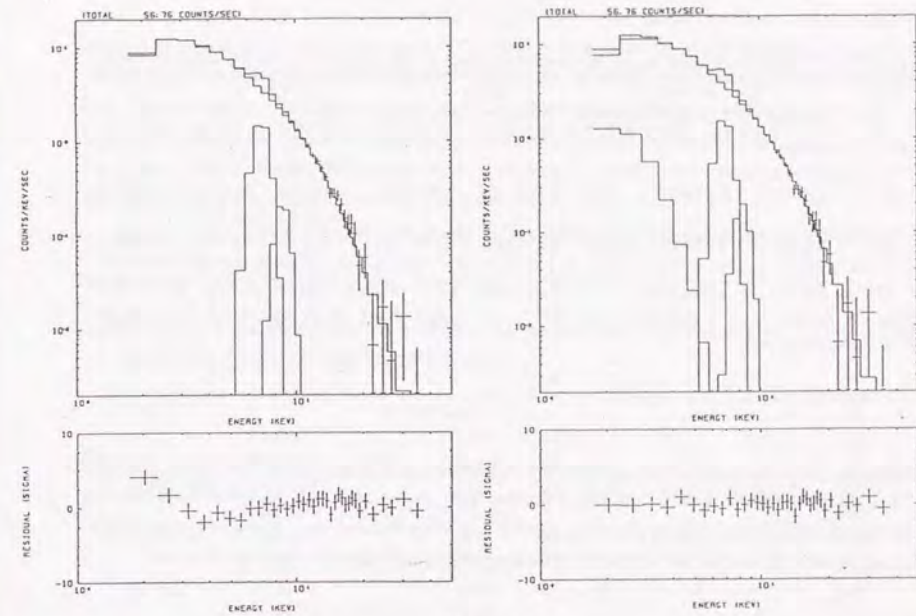
Figure 5.11:

Results of the fit of the pulse-peak spectrum of EX Hya. (a) Model-1 with two iron lines (χ^2_ν =1.59). (b) Two thermal bremsstrahlung continua with two lines (χ^2_ν =0.46).

body, thermal bremsstrahlung or power-law including two iron lines. Results of the fit by assuming the thermal bremsstrahlung as soft component is shown in figure 5.11(b) and the best fit parameters are listed in table 5.6. Resultant χ^2 values are almost the same for these three fits, and temperatures of the hard bremsstrahlung component is unaffected by the particular soft component model used in the fit.

As in the other three Group-1 sources described in the previous subsection, the pulse-peak temperature of EX Hya thus obtained is not different from that of the pulse-bottom. In addition, we have obtained only the upper limits for hydrogen column densities both in the pulse-peak and the pulse-bottom spectra. Therefore, energy-dependence of the modulation amplitude of EX Hya cannot be attributed to photoelectric absorption. Alternatively, unlike in the other Group-1 sources, the soft component in the pulse-peak spectrum is responsible for the larger modulation amplitude in lower energies. In addition, normalization of the hard continuum significanly changes between the pulse-peak and the pulse-bottom. This resembles EF Eri (a Group-1 polar), and completely different from the two Group-1 intermediate polars. This is responsible for energy independent modulation amplitude of $\sim$10% in higher

Table 5.6: Fit parameters of the pulse-peak spectrum of EX Hya with two continuum model.

Model[a]	Thermal brem.			Soft comp.		Iron line		χ^2_ν
	Norm.[b]	Temp.[c]	$\log N_H^d$	Norm.[b]	α or Temp.[c]	Int.[e]	Energy[c]	(d.o.f)
PL	2.15±0.15	9.08±0.56	<21.6	1.56±0.76	3.16±1.37	6.3±0.5	6.81±0.06	0.44(27)
						0.9±0.4	8.47±0.36	
BB	2.32±0.04	8.75±0.22	<21.6	8.37±2.70	0.37±0.02	6.0±0.4	6.81±0.06	0.51(27)
						0.8±0.4	8.48±0.41	
TB	2.33±0.04	8.68±0.22	<21.9	3.31±1.25	0.68±0.09	6.1±0.5	6.82±0.04	0.46(27)
						0.7±0.3	8.48±0.37	

a: Models for the soft component. PL = Power-Law; TB = Thermal Bremsstrahlung; BB = Black Body. b: In unit of 10^{-4} photons $s^{-1}cm^{-2}keV^{-1}$. c: In unit of keV. d: In unit of cm^{-2}. e: In unit of 10^{-2} photons $s^{-1}cm^{-2}$.

energies. Therefore, although modulation amplitude of EX Hya shown in figure 5.3 and 5.4 is qualitatively similar to the other intermediate polars, its spin modulation properties are completely different from the other Group-1 intermediate polars. Taking this point into account, we will discuss the accretion pole geometry of EX Hya in detail in chapter 6.

5.3.4   Spin-modulated Components of Group-2 Sources

Group-2 sources are composed of H0538+608, E1405–451, FO Aqr, AO Psc and RE0751+14 whose spin-phase average spectra cannot be fitted with Model-1. A clue to understanding the spectra of these sources exists in the SC-ratio. As seen in figure 5.9, the SC-ratio of the Group-2 sources becomes flatter in higher energies as in the Group-1 sources, which indicates the existence of a hard component invariant in shape with spin phase as found in the Group-1 sources. This is consitent with the fact that the residuals of the fits to the spin-phase average spectra of Group-2 sources with Model-1 exist mainly in lower energy bands (subsection 5.2.3). According to the results in subsection 5.2.4, this component can naturally be identified with the optically thin thermal bremsstrahlung component above 10keV.

The SC-ratio of Group-1 sources monotonically increases in polars or decreases in intermediate polars with decreasing energy, especially for EF Eri and 3A0729+103, corresponding to the difference in hydrogen column density. This is the same in the Group-2 sources down to at least ∼5keV. It is, however, clearly seen that their SC-ratios flattens below ∼5keV, particularly in E1405–451, FO Aqr and AO Psc, which suggests the existence of another component in lower energies.

Therefore, we have attempted to fit the observed spectra of the Group-2 sources with a spectral model composed of two continua. We temporally exclude AM Her since its SC-ratio decreases monotonously in higher energy band, significantly different from other sources. It will be treated separately in section 5.6. As have already been established, the hard compo-

nent is represented by thermal bremsstrahlung. On the other hand, we have no information about the shape of the soft component. Therefore, we temporarily adopt Boltzmann function as representing the spectrum of the soft component. We take the photoelectric absorption into account only for the hard component since Boltzmann function itself have enough degree of freedom. As before, we include a Gaussian line representing the iron emission line. In order to attain stable fitting, we fix the temperature of thermal bremsstrahlung to that determined in subsection 5.2.4 using the data above 10keV.

From the statistical point of view, we have first fitted the pulse-peak spectra with this two continuum model. Results are summarized in table 5.7. The fits are on the average good with

Table 5.7: Spectral fit parameters with thermal bremsstrahlung plus Boltzmann function for the pulse-peak spectra of the Group-2 sources.

Source	Continuum				Iron line		χ^2_ν
	Norm.[a]	α^b	Temp.[c]	$\log N_H^{\ d}$	Int.[e]	Energy[c]	(d.o.f)
	Norm.[a]		Temp.[c]				
H0538+608	0.56±0.01		39.6[f]	22.21±0.03	1.5±0.1	6.57±0.06	1.50
	0.09±0.01	1.58±0.11	28.1±16.3				(24)
E1405–451	0.23±0.02		16.9[f]	23.21±0.07	1.5±0.21	6.71±0.08	1.11
	0.18±0.01	1.28±0.04	25.9±6.2				(29)
FO Aqr	0.87±0.02		33.9[f]	23.11±0.03	2.0±0.2	6.48±0.09	0.67
	0.31±0.02	1.72±0.10	13.9±5.7				(30)
AO Psc	0.75±0.15		13.9[f]	22.66±0.11	2.5±0.3	6.73±0.07	0.65
	0.41±0.17	1.60±0.67	12.4±13.7				(25)
RE0751+14	0.48±0.21		20.4[f]	23.60±0.10	1.7±0.3	6.70±0.10	1.06
	0.46±0.17	1.42±0.32	19.3±21.1				(19)

Parameters of the continuum listed in the first row and the second row represents those of thermal bremsstrahlung (hard component) and Boltzmann (soft component), respectively. Each superfix means that;

a: In unit of 10^{-4} photons s^{-1} cm^{-2} keV^{-1}.
b: Photon index.
c: In unit of keV.
d: In unit of cm^{-2}.
e: In unit of 10^{-2} photons s^{-1} cm^{-2}.
f: Fixed at the values in table 5.4.

resultant photon index ranging from 1.3 to 1.7 for the Boltzmann component, although its temperature is not constrained well. This photon index suggests that the soft component also has a shape similar to thermal bremsstrahlung spectrum. Therefore, we substitute another thermal bremsstrahlung model for Boltzmann function and perform spectral fitting for pulse-peak spectra again with this two component model. This time we take the photoelectric absorption also for the soft component. Results are summarized in table 5.8, where we find that the fits remain reasonablly good. As the temperature of the newly introduced thermal

Table 5.8: Spectral fit parameters with two thermal bremsstrahlung continuum model for the pulse-peak spectra of the Group-2 sources.

Source	Continuum Norm. Norm.	Continuum Temp. Temp.	$\log N_H$	Iron line Int.	Iron line Energy	χ^2_ν (d.o.f.)
H0538+608	0.33±0.10	39.6[a]	22.50±0.18	1.5±0.2	6.57±0.07	1.41
	0.30±0.10	29.6±6.6	< 22.3			(24)
E1405−451	0.20±0.02	15.9[a]	23.19±0.09	1.5±0.2	6.71±0.08	1.13
	0.20±0.01	33.4±10.5	<23.5			(29)
FO Aqr	0.75±0.03	33.9[a]	23.18±0.03	2.0±0.3	6.46±0.09	0.72
	0.25±0.02	17.3±4.9	<21.9			(30)
AO Psc	0.55±0.21	13.9[a]	22.74±0.18	2.5±0.3	6.72±0.07	0.63
	0.44±0.21	11.3±2.5	<22.4			(25)
RE0751+14	0.44±0.21	20.4[a]	23.63±0.15	1.7±0.3	6.69±0.09	1.02
	0.39±0.03	18.0±16.3	20.0[b]			(19)

Parameters of the continuum listed in the first row and the second row represents those of the hard component (more-absorbed) and the soft component (less-absorbed), respectively. As for the label of each column, refer to table 5.7.

a: Fixed at the values listed in table 5.4.

b: Fixed since energy band below 4keV is discarded because of solar X-ray contamination.

bremsstrahlung component, though not constrained very well, does not differ drastically from that of the hard component, we have no strong reason to distinguish temperatures of the two continuum components if we take into account also the error of the temperature of the primary component listed in table 5.4. We have thus attempted to fit both the pulse-peak and the pulse-bottom spectra with a model including two thermal bremsstrahlung continua with common temperature but their normalizations set free. We take the photoelectric absorption into account only for one component since we have obtained only the upper limit of N_H for the soft component in table 5.8. We also include a Gaussian line represinting the iron line emission. This model is so-called "leaky absorber model". The best fit parameters with leaky absorber model are summarized in table 5.9.

It should be remarked that the pulse-bottom spectrum of H0538+608 and E1405−451 can be fitted with Model-1; that is, the spectra does not require two separate values of N_H. The best fit parameters with Model-1 are also listed in table 5.9. Among them, it is likely that the fit to E1405−451 with Model-1 becomes acceptable simply due to poor statistics, for the best fit temperature obtained with Model-1 is higher than that obtained with leaky absorber model, which is due to the flattening of the spectrum caused by the coexistence of absorbed and non-absorbed components. On the contrary, we believe that it is not necessary to introduce leaky absorber model for the pulse-bottom spectrum of H0538+608 since the

Table 5.9: Best fit parameters with Leaky absorber model for pulse-peak and pulse-bottom spectra.

Source	Continuum Norm.-1[a] Norm.-2[b]	Continuum Temp.[c] CF [g]	$\log N_H$ [d]	Int.[e]	Iron line Energy[c]	E.W. [f]	χ^2_ν (d.o.f)
H0538+608							
peak	0.36±0.06	34.6± 3.4	22.46±0.16	1.5±0.2	6.56±0.07	360± 60	1.36
	0.27±0.07	57± 8					(25)
bottom	0.11±0.10	24.9± 5.4	22.40±0.85	0.4±0.2	6.55±0.27	210±110	1.03
	0.18±0.11	38±26					(25)
(Model-1)	0.29±0.01	26.1± 4.1	21.82±0.16	0.4±0.2	6.54±0.25		0.99
							(26)
E1405−451							
peak	0.22±0.06	20.9± 6.0	23.19±0.16	1.5±0.2	6.71±0.09	660±130	1.08
	0.19±0.01	54± 7					(30)
bottom	0.08±0.06	17.2± 5.3	23.81±0.29	0.5±0.2	6.79±0.26	530±240	0.94
	0.14±0.08	36±22					(23)
(Model-1)	0.15±0.01	32.5±13.3	< 22.0	0.6±0.2	6.77±0.26		0.85
							(24)
FO Aqr							
peak	0.77±0.07	27.4± 4.5	23.17±0.06	2.0±0.4	6.47±0.10	350± 70	0.67
	0.23±0.02	77± 2					(31)
bottom	0.59±0.09	35.2±13.7	23.50±0.07	1.6±0.3	6.62±0.10	490±110	1.18
	0.12±0.01	83± 2					(31)
AO Psc							
peak	0.65±0.06	12.8± 1.0	22.67±0.13	2.5±0.3	6.72±0.07	510± 80	0.61
	0.33±0.08	66± 6					(26)
bottom	0.51±0.07	16.7± 3.7	23.04±0.11	1.9±0.4	6.64±0.11	600±140	0.93
	0.12±0.03	81± 4					(26)
RE0751+14							
peak	0.41±0.18	20.1± 7.7	23.62±0.18	1.7±0.3	6.68±0.09	460±110	1.01
	0.39±0.03	51±11					(20)
bottom	1.04±0.70	8.9±2.7	23.89±0.10	0.6±0.3	6.50±0.29	190±130	0.93
	0.38±0.04	73±13					(20)

a: Normalization of the component with photoelectric absorption in unit of 10^{-2}photons s^{-1} cm^{-2} keV^{-1}. b: Normalization of the component without photoelectric absorption in unit of 10^{-2}photons s^{-1} cm^{-2} keV^{-1}. c: Temperature in unit of keV. d: Hydrogen column density in unit of cm^{-2}. e: Line intensity in unit of photons s^{-1} cm^{-2}. f: Line equivalent width in unit of eV. g: Covering Fraction in units of %. See text for definition.

best fit temperature obtained with Model-1 is almost the same as that obtained with leaky absorber model.

We also summarize spectral parameters, which characterize spin modulations of the hard
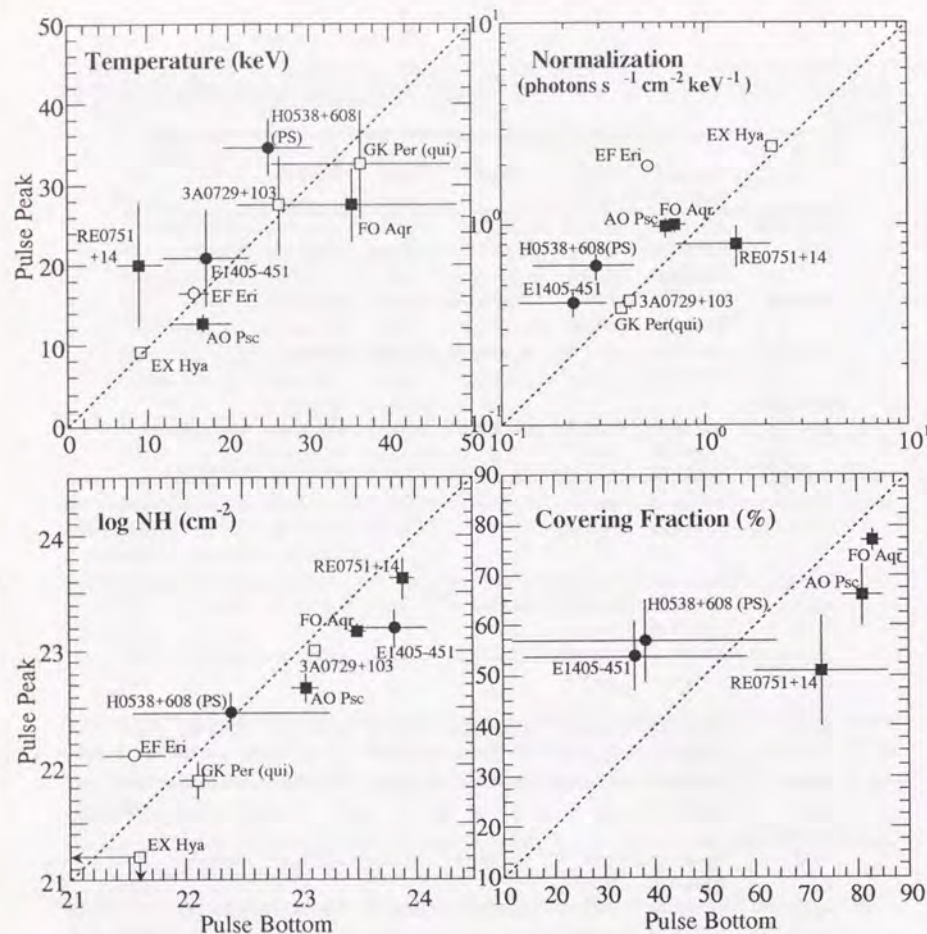
Figure 5.12: Comparison of spectral parameters between the pulse-peak and the pulse-bottom. Polars and intermediate polars are indicated with circles and squares, respectively, and Group-1 sources and Group-2 sources are represented with open and filled symbols, respectively.

X-ray intensity, in the pulse-peak and the pulse-bottom of both Group-1 and Group-2 sources in figure 5.12. Polars and intermediate polars are indicated with circles and squares, respectively, and Group-1 and Group-2 are represented with open and filled symbols, respectively.

From table 5.9 and figure 5.12, we see that the temperature does not differ significantly

between the pulse-peak and the pulse-bottom for E1405–451, FO Aqr and AO Psc, in agreement with the properties of the Group-1 sources. The temperature of the pulse-peak and the pulse-bottom are, however, different at the 90% confidence level for H0538+608 and RE0751+14. We have fitted their pulse-bottom spectra with the leaky absorber model with temperature fixed at the value of pulse-peak spectrum. Resultant reduced χ^2 values are between 1.2 and 1.3 for both spectra, which means marginally acceptable. Therefore, the temperatures may be different between the pulse-peak and the pulse-bottom in H0538+608 and RE0751+14, although not conclusive. Notice that this difference is difficult to be recognized in SC-ratio (figure 5.9) for H0538+608 since temperatures in the pulse-peak and the pulse-bottom are more than 20keV. The temperature difference of RE0751+14 is marginally revealed in SC-ratio as a slight decline in higher energies, although statistics are poor.

For the other three sources, E1405–451 (polar), FO Aqr and AO Psc (intermediate polar), the temperature does not change between the pulse-peak and the pulse-bottom as is the case for all the Group-1 sources. We have again tried to fit the pulse-bottom spectra of them with leaky absorber model with the pulse-peak temperature. Reduced χ^2 values of them are between 0.8 and 1.0.

To discuss the amount of absorption for Group-2 sources, we have to examine "Covering Fraction" (CF), defined as the ratio of the normalization of the absorbed component to the sum of the normalizations, as well as hydrogen column density. Both CF and hydrogen column density are larger in the pulse-bottom in two intermediate polars, FO Aqr and AO Psc, as indicated from table 5.9. Even for the sources in which these parameters are not well constrained, SC-ratio in lower energies shown in figure 5.9 now indicates the amount of absorption, since no extra soft component is found from spectral fitting. Therefore, the amount of absorption is larger in the pulse-peak phase in two polars, H0538+608 and E1405–451.

Sum of normalizations of the two continua, which is proportional to the emission measure as described in subsection 5.2.2, is modulated in H0538+608 and E1405–451 like in the Group-1 polar, EF Eri. It is, however, modulated also in FO Aqr and AO Psc in such a way as it is larger in the pulse-peak, which is unlike in Group-1 intermediate polars. Although it is not so large as in polars, there is energy-independent modulation in Group-2 intermediate polars.

We conclude that characteristics of intensity spin modulation of Group-2 sources are essentially the same as those of Group-1 sources, except that the absorption characteristics of the Group-2 sources require more than a single value of N_H. In addition, a temperature difference between the pulse-peak and the pulse-bottom was detected from H0538+608 and RE0751+14, and there is a change in normalization between the pulse-peak and the pulse-bottom in two intermediate polars, FO Aqr and AO Psc.

Finally we remark on the pulse-peak spectrum of H0538+608. As shown in table 5.9, the fit to the pulse-peak spectrum of H0538+608 with the leaky absorber model is marginally acceptable. The fit is, however, significantly improved by introducing ionization of iron,

which will be described in detail in section 5.4.

5.3.5 Summary of Spin-modulation Properties

As seen from figure 5.12, characteristics of hard X-ray spin modulation in polars and intermediate polars are summarized as follows.

1. Spin modulation of the hard X-ray intensity in polar is caused mainly by the change of normalization of the continuum, which is proportional to the emission measure (EM) as mentioned in subsection 5.2.2, and a little decrease in the modulation amplitude in lower energies is due to larger photoelectric absorption in the pulse-peak phase.

2. Spin modulation of the hard X-ray intensity in intermediate polar is caused mostly by the change in photoelectric absorption with spin phase. Although there is a change also in continuum normalization in EX Hya and Group-2 intermediate polars, the fractional change is smaller than that for polars.

3. We have detected an evidence of temperature variation between the pulse-peak and the pulse-bottom phase from two Group-2 sources, H0538+608 and RE0751+14. In H0538+608 modulation amplitude in higher energies may be enhanced a little because the temperature is higher in the pulse-peak phase.

4. In RE0751+14, although the temperature is different between the pulse-peak and the pulse-bottom, behaviour of N_H and CF is the same as the other two Group-2 intermediate polars, FO Aqr and AO Psc. The sum of normalizations is not constrained well in RE0751+14.

5. The spin modulation of the X-ray intensity in EX Hya is caused by considerablly different mechanism from the other intermediate polars. The larger modulation amplitude in lower energies is caused by a soft component visible in the pulse-peak phase, not by photoelectric absorption. In addition, unlike other Group-1 intermediate polars, there is a significant change in the continuum normalization.

As noticed from this summary, there is very little difference between the Group-1 and the Group-2 sources about the spin modulation characteristics. We conclude that Group-1, in which there is no, or very small, if any, distribution in the absorbing matter, is classified as a special case of Group-2. In chapter 6, we discuss the accretion pole geometry of MCVs with these observational fact.

5.4 Re-examination of Spin-phase Average Spectra

Given the results of spin-phase resolved spectroscopy presented in section 5.3, in this section, we return to the spin-phase average spectra of the Group-2 sources. In the beginning, we

evaluate them with leaky absorber model. We take into account photoelectric absorption due to matter of solar abundances for both components, and we assume that the absorber is neutral. The best fit parameters are summarized in table 5.10. The fits are on the

Table 5.10: Best fit parameters of the spin-phase average spectra of the Group-2 sources with leaky absorber model.

| Source | Continuum | | | | Iron line | | | |
	Norm.-1[a] Norm.-2[b]	Temp.[c]	$\log N_H$ [d] $\log N_H$ [d]	Int.[e]	Energy[c]	E.W.[f]	χ_ν^2 (d.o.f)
AM Her	0.65±0.02 1.11±0.02	18.1±0.4	23.20±0.03 < 20.9	5.1±0.2	6.70±0.03	520± 30	2.62 (30)
H0538+608(PS)	0.06±0.01 0.48±0.01	29.4±2.4	22.92±0.24 < 22.0	0.9±0.1	6.66±0.10	250± 40	1.32 (29)
E1405−451	0.17±0.02 0.19±0.01	14.7±1.3	23.41±0.08 < 21.8	1.0±0.1	6.78±0.08	620± 90	1.02 (29)
GK Per(Outb.)	15.7±10.8 6.8 ± 1.2	15.5±9.5	24.25±0.14 22.99±0.09	23 ± 7	6.61±0.17	580±320	1.16 (27)
TV Col	0.50±0.17 0.37±0.19	24.5±3.9	22.88±0.21 < 22.1	2.2±0.3	6.62±0.08	430±140	1.90 (27)
FO Aqr	0.73±0.05 0.13±0.03	31.5±5.0	23.34±0.06 < 22.1	1.8±0.2	6.55±0.06	410± 60	1.13 (30)
AO Psc	0.54±0.02 0.29±0.01	13.7±0.6	22.91±0.03 < 21.8	2.2±0.2	6.64±0.05	520± 50	0.68 (25)
RE0751+14	0.30±0.15 0.37±0.04	20.0±8.5	23.66±0.22 22.22±0.13	1.2±0.3	6.70±0.11	380±100	1.13 (29)

a: Normalization of the component with photoelectric absorption in unit of 10^{-2}photons s^{-1} cm^{-2} keV^{-1}.
b: Normalization of the component without photoelectric absorption in unit of 10^{-2}photons s^{-1} keV^{-1}.
c: Temperature in unit of keV.
d: Hydrogen column density in unit of cm^{-2}.
e: Line intensity in unit of photons s^{-1} cm^{-2}.
f: Line equivalent width in unit of eV.

average acceptable, indicating that the spin-phase average spectra are basically explained with leaky absorber model. Hydrogen column densities of the less-absorbed component of all the sources are so small that we have obtained only the upper limits on them except GK Per and RE0751+14.

Resultant reduced χ^2 values indicates, however, that the fits are unacceptable for AM Her and TV Col, and marginally acceptable for H0538+608. Figure 5.13 shows the results of the fits for AM Her and TV Col. As clearly seen from this figure, there is a clear dip-like structure around 7–10 keV especially for AM Her, which roughly corresponds to the iron K-edge absorption energy. The iron K-edge absorption can be identified in the raw spectra of E1405−451 (pulse-peak), FO Aqr, AO Psc, 3A0729+103, and RE0751+14 (pulse-bottom) shown in figure 5.9 as a spectral dip around 8–10keV. Also it is revealed that the dip
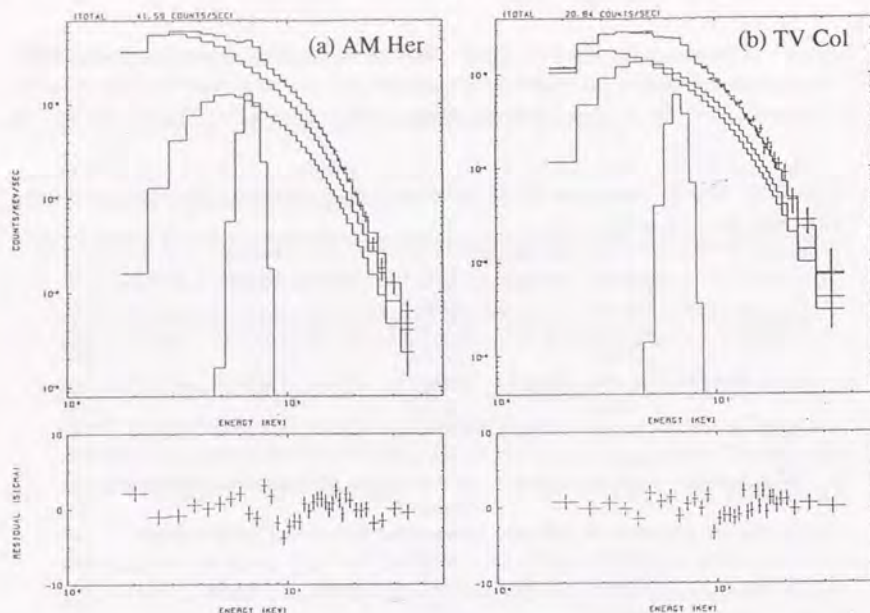
Figure 5.13: Spectral fit of the spin-phase average spectra of AM Her and TV Col with leaky absorber model (cold absorber).

becomes deeper when photoelectric absorption becomes stronger as shown in the SC-ratios of H0538+608, FO Aqr and RE0751+14 in figure 5.9. Therefore, this spectral structure is likely to be attributed to the K-edge absorption of iron. The depth of K-edge absorption is affected by the abundances and the degree of ionization of iron. In the case of ionization, the position of K-edge absorption shifts to higher energies. It is thus possible that the cold matter of solar abundance cannot reproduce the iron K-edge absorption structure in individual spectra.

Therefore, we have attempted to treat photoelectric absorption due to iron and that due to the other light elements separately. The model of photoelectric absorption used in leaky absorber model is modified as follows

$$N_H \sigma(E) \longrightarrow N'_H \sigma'(E) + N_{Fe}\sigma_{Fe}(E_{edge}; E), \tag{5.11}$$

where $\sigma'(E)$ represents the cross section of photoelectric absorption due to matter of solar abundance, but only the abundance of iron is set equal to zero. $\sigma_{Fe}(E)$ means the cross section of photoelectric absorption due to iron K-shell. N'_H and N_{Fe} mean column density of the light elements other than iron, and that of iron, respectively, converted into equiva-

lent hydrogen column densities under the assumption of solar abundances. E_{edge} means the energy of the iron K-edge absorption. Hereafter we use notation N'_H and N_H as representing the hydrogen column density of matter of solar abundance without and with iron, respectively. As a result, free parameters of this new absorption model is N'_H, N_{Fe} and E_{edge}. The difference between N'_H and N_{Fe}, if any, represents either the partial ionization of the absorber or the abundance anomaly compared with that of the sun, and the value of E_{edge} represents the degree of ionization of the absorber. We apply this treatment for photoelectric absorption of the more-absorbed component only, since the optical depth of the iron K-edge absorption is so small for N_H of the less-absorbed component of RE0751+14 ($\sim 10^{22}\mathrm{cm}^{-2}$). Even for GK Per ($N_H \sim 10^{23}\mathrm{cm}^{-2}$), major improvement of the fit, if any, is expected to come from photoelectric absorption of the more-absorbed component ($N_H \sim 10^{24}\mathrm{cm}^2$). We remove photoelectric absorption from the less-absorbed component for the sources from which we obtain only the upper limit (see table 5.10).

We have fitted the spin-phase average spectra with the leaky absorber model with modified photoelectric absorption represented with eq(5.11). The best fits are obtained with the $E_{edge} = 7.1\mathrm{keV}$ (neutral iron) for E1405–451 and GK Per (outburst), and the upper limit to E_{edge} of them are 7.9keV and 7.4keV, respectively. For RE0751+14, almost the same reduced χ^2 values are obtained for all the values of E_{edge} in the physically meaningful energy range— from 7.1keV for neutral iron to 9.3 keV for hydrogen-like iron. Thus evidence for the ionization of the absorbing matter is not found from these three sources. We have, however, obtained iron K-edge energy significantly deviated from that of the neutral iron from the fitting of the other 5 sources. (We would like to remark that the evidence of the ionization of iron is not so strong for FO Aqr and AO Psc as for AM Her, H0538+608 and TV Col since the acceptable fits have already obtained with leaky absorber model and N'_H/N_{Fe} is consistent with unity). The best fit parameters of them are summarized in table 5.11. Resultant reduced χ^2 values now become less than 1.2 for all the sources. It is concluded from $E_{edge} \geq 8\mathrm{keV}$ and $N'_H/N_{Fe} \leq 1.0$ for most sources listed in table 5.11 that the absorber is significantly ionized in these sources. Results of the fits of the spin-phase average spectra of the Group-2 sources either with leaky absorber model or leaky absorber model with modified absorption are shown in figure 5.14.

However, although we have obtained acceptable fits with leaky absorber model with modified photoelectric absorption, resultant iron edge energies of most sources listed in table 5.11 exceed $\sim 8\mathrm{keV}$. Light elements up to silicon coexisting with such an iron should be almost fully ionized (Kallman & McCray 1982), and $N'_H/N_{Fe} \ll 0.1$ is expected, in contradiction to table 5.11. Therefore, it is more natural to consider that the emission region is covered with another ionized absorber in which the elements other than iron is completely ionized as well as the neutral leaky absorber. From this point of view, we have tried leaky absorber model with additional ionized iron K-edge absorption. Here, cold absorber is composed of matter with solar abundances including iron also. On the other hand, we have assumed that CF of ionized iron K-edge absorption is 100%. Therefore, in

Table 5.11: Best fit parameters of the spin-phase average spectra of the Group-2 sources with leaky absorber model with photoelectric absorption of iron and the other elements separately.

Source	Continuum				Int.[e]	Iron line		χ^2_ν
	Norm.-1[a] Norm.-2[b]	Temp.[c]	$\log N'_H$ [d] N'_H/N_{Fe}	$\log N_{Fe}$ [d] E_{edge} [g]		Energy[c]	E.W.[f]	(d.o.f)
AM Her	0.88±0.10	16.9±0.9	23.39±0.05	23.72±0.08	4.1±0.4	6.64±0.04	400± 40	0.79
	1.12±0.02		$0.47^{+0.11}_{-0.09}$	8.25±0.17	.			(29)
H0538+608 (PS)	0.17±0.03	30.7±4.5	22.88±0.26	23.65±0.29	0.7±0.2	6.65±0.15	190± 60	1.03
	0.40±0.03		$0.17^{+0.34}_{-0.09}$	8.05±0.55				(28)
TV Col	0.54±0.05	30.0±5.5	22.96±0.11	23.68±0.17	1.9±0.3	6.54±0.09	350± 70	1.20
	0.34±0.04		$0.19^{+0.12}_{-0.07}$	8.85±0.35				(26)
FO Aqr	0.87±0.02	26.2±4.0	23.45±0.04	23.43±0.11	1.4±0.3	6.49±0.07	320± 70	0.91
	0.12±0.01		$1.05^{+0.33}_{-0.25}$	7.55±0.22				(29)
AO Psc	0.59±0.04	14.0±1.3	22.97±0.08	23.09±0.40	2.1±0.3	6.60±0.06	485± 60	0.58
	0.25±0.03		$0.76^{+1.26}_{-0.46}$	8.25±0.70				(24)

a: Normalization of the component with photoelectric absorption in units of 10^{-2}photons s^{-1} cm^{-2} keV^{-1}.
b: Normalization of the component without photoelectric absorption in units of 10^{-2}photons s^{-1} cm^{-2} keV^{-1}.
c: Temperature in units of keV.
d: Hydrogen column density in units of cm^{-2}.
e: Line intensity in units of 10^{-4}photons s^{-1} cm^{-2}.
f: Line equivalent width in units of eV.
g: Iron K-edge energy in units of keV.

this treatment, the K-edge absorptions of both the ionized and neutral iron are included in the model. Results are summarized in table 5.12. As seen from this table, leaky absorber model with additional iron K-edge absorption gives acceptable fits to the observed spectra. The column densities of ionized iron of all the sources are significantly smaller that those listed in table 5.11. This is because part of the iron K-edge absorption is attributed to neutral iron included in the leaky absorbing matter in this model. Although the iron edge energies are not confined very well, they are mostly above 8keV. Therefore, we believe that leaky absorber with ionized iron K-edge absorption is more appropriate for the spin-phase average spectra of at least 4 sources, AM Her, H0538+608, TV Col, and AO Psc, and possibly also for FO Aqr. As the K-edge absorption energies are very high, the additional iron absorption probably occurs in the emission region itself or in the vicinity of the emission region.

Table 5.12: Best fit parameters of the spin-phase average spectra of the Group-2 sources with leaky absorber model and additional ionized iron K-edge absorption with Covering Fraction of 100%.

Source	Continuum				Int.	Iron line		χ^2_ν
	Norm.-1 Norm.-2[b]	Temp.	$\log N_H$	$\log N_{Fe}$ E_{edge}		Energy	E.W.	(d.o.f)
AM Her	0.85±0.10	17.0±1.0	23.32±0.05	23.16±0.10	4.2±0.4	6.70±0.04	410± 40	0.91
	1.13±0.01			8.6±0.2				(29)
H0538+608 (PS)	0.16±0.03	31.9±4.6	22.73±0.29	23.04±0.24	0.7±0.2	6.65±0.14	200± 60	1.02
	0.39±0.04			8.4±0.6				(28)
TV Col	0.53±0.04	30.7±5.8	22.89±0.12	23.43±0.16	1.9±0.3	6.59±0.10	340± 70	1.14
	0.34±0.04			9.1±0.4				(26)
FO Aqr	0.80±0.07	29.0±4.5	23.37±0.04	22.90±0.29	1.5±0.3	6.56±0.07	330± 70	0.96
	0.13±0.01			8.1±0.5				(29)
AO Psc	0.57±0.04	14.3±1.3	22.88±0.08	22.63±0.75	2.2±0.3	6.64±0.06	500± 60	0.70
	0.25±0.03			$8.5^{+1.2}_{-1.7}$				(24)

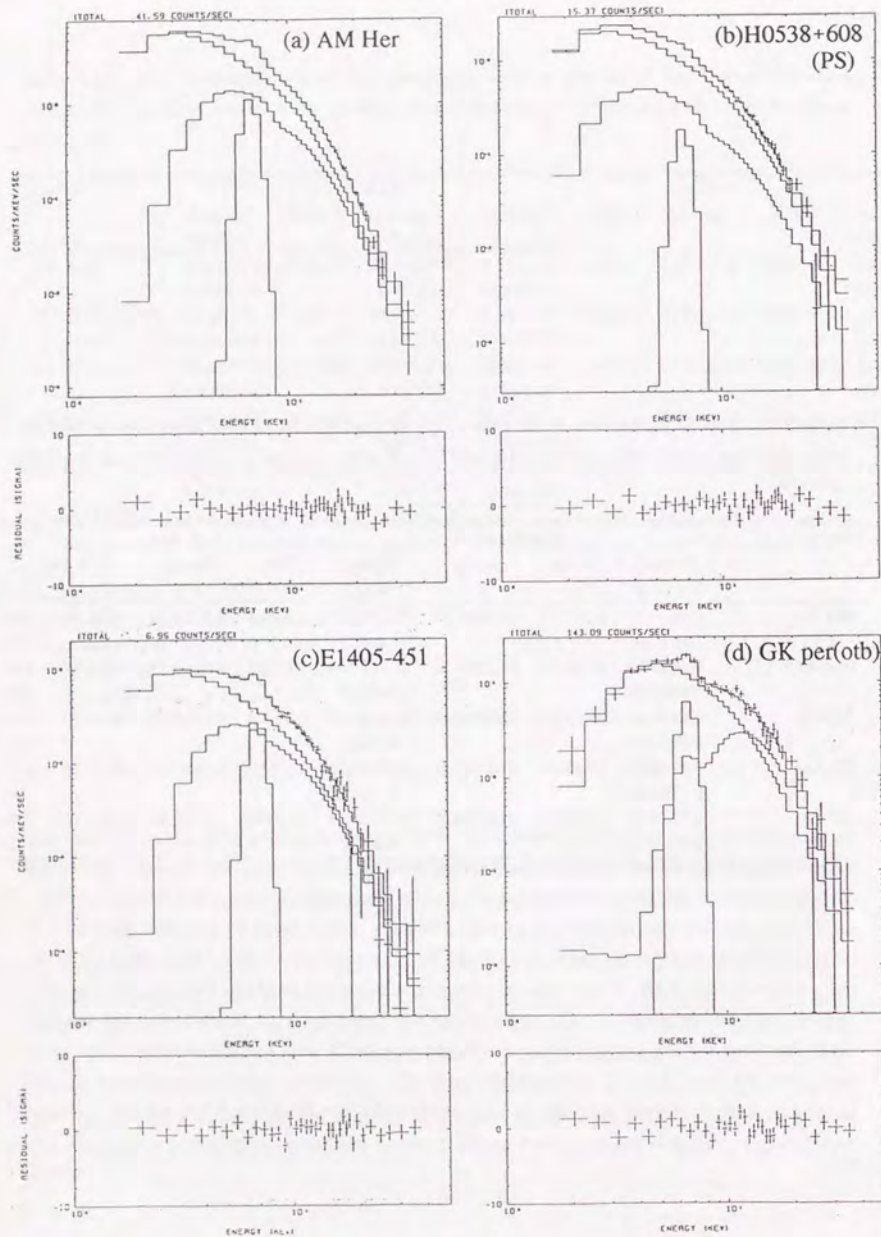The meaning of each column is the same as that of table 5.11.

Figure 5.14: Results of the spectral fit of the spin-phase average spectra of the Group-2 sources either with leaky absorber model (E1405–451 and GK Per) or leaky absorber model with the absorption modified with eq(5.11) (AM Her and H0538+608).
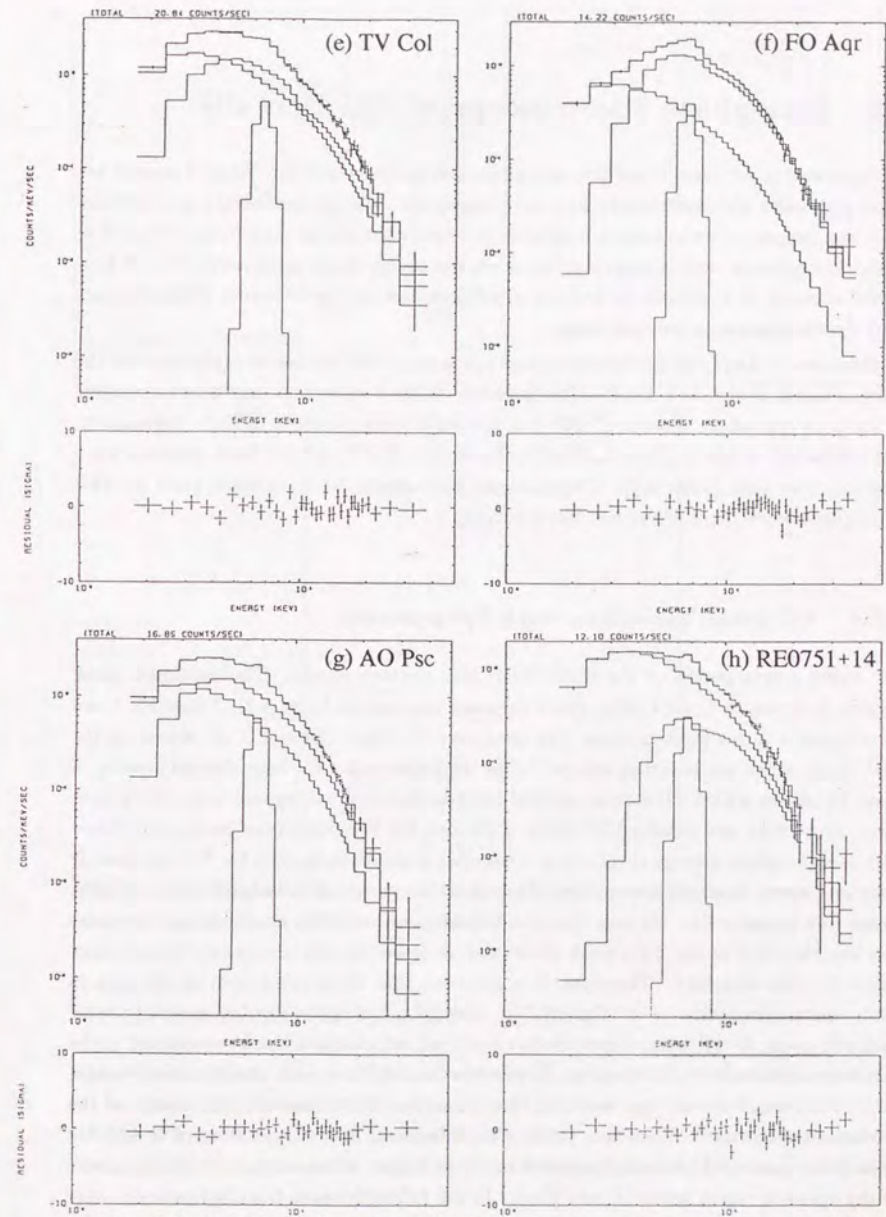
Figure 5.14: Results of the spectral fit of the spin-phase average spectra of the Group-2 sources either with leaky absorber model (RE0751+14) or leaky absorber model with the absorption modified with eq(5.11) (TV Col, FO Aqr and AO Psc).

5.5   Spin-phase Spectroscopy of AM Herculis

As mentioned in section 5.3 and 5.4, spin-phase average spectra of the Group-2 sources are
fitted with leaky absorber model. The two components —the more-absorbed and the less-
absorbed component with common temperature— form a flat part in the SC-ratio (figure 5.9)
in high energy range, and in some sources, also in low energy range, respectively. In AM Her,
on the contrary, it is difficult to find out any flat portions in the SC-ratio, which suggests
more drastic changes in the continuum.

On the other hand, the spin-phase average spectrum of AM Her can be explained with the
leaky absorber model, as is the case for the other Group-2 sources. It may thus be possible
to evaluate spin-phase spectra of AM Her also with leaky absorber model. Fortunately,
AM Her is one of the brightest sources among known MCVs and has been observed for a
long exposure time (table 4.1). Therefore, we have attempted to examine more detailed
pulse-phase dependence of the AM Her spectrum.

5.5.1   SC-ratio Variations with Spin-phases

We divide a spin period of the white dwarf into thirteen phases. The employed phase
division is shown in figure 5.16(a) (with the same phasings as figure 5.2). Phase 13, 1 and
2 corresponds to the pulse-bottom. The intensities of phase 6 through 9 are almost at the
peak level, which are hereafter referred to as the pulse-peak. We have derived spectra of
these 13 phases with SUD-sorting method for a background subtraction and with proper
aspect correction, and obtained SC-ratios of the rise, the decline and the pulse-peak phases
with the spin-phase average spectrum as a reference as shown in figure 5.15. We can identify
a dip or a hump structure centered on $\sim$7keV in all the panels, which is probably attributed
to the iron emission line. As seen from the bottom panel, the SC-ratio is almost flat above
this line structure in the pulse-peak phase, and it decreases with decreasing X-ray energy
below the line structure. Therefore, it is expected that there exists spin modulation in
photoelectric absorption as in other MCVs. The SC-ratios in the top two panels increase
with decreasing X-ray energy below the line structure, which might also be attributed to the
variation of photoelectric absorption. However in the top two panels, the SC-ratio decrease
with increasing X-ray energy above the line structure, which suggests the change of the
continuum shape itself. Therefore, the spin modulation of hard X-ray intensity of AM Her
is probably generated via variations of both photoelectric absorption and the temperature
of the emission region with the spin phase. In the following subsections, we perform more
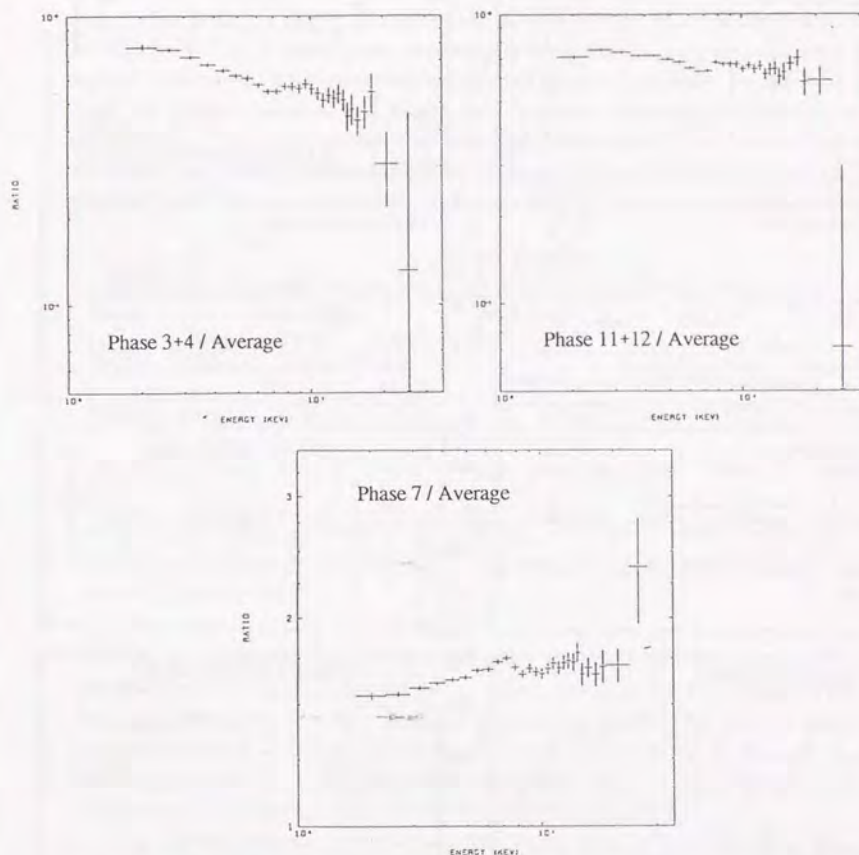detailed analysis.

Figure 5.15: SC-ratios of the spectra of the rise, the decline, and the pulse-peak phases with
the spin-phase average spectrum as a reference.

5.5.2   Evaluation of Spin-phase Spectra

To evaluate spectral change of AM Her with the spin-phase, we have first attempted to fit
these 13 spectra with Model-1. Resultant reduced χ^2 values are shown in figure 5.16(b). The
degree of freedom is 31 for all the spectra. The fit can be regarded as acceptable at 90%
confidence level if χ_ν^2 is smaller than 1.33. From this figure, Model-1 gives acceptable fits to
the spectra of phase 2, 3 and 12.

Leaky absorber model with photoelectric absorption represented with eq(5.11) was also
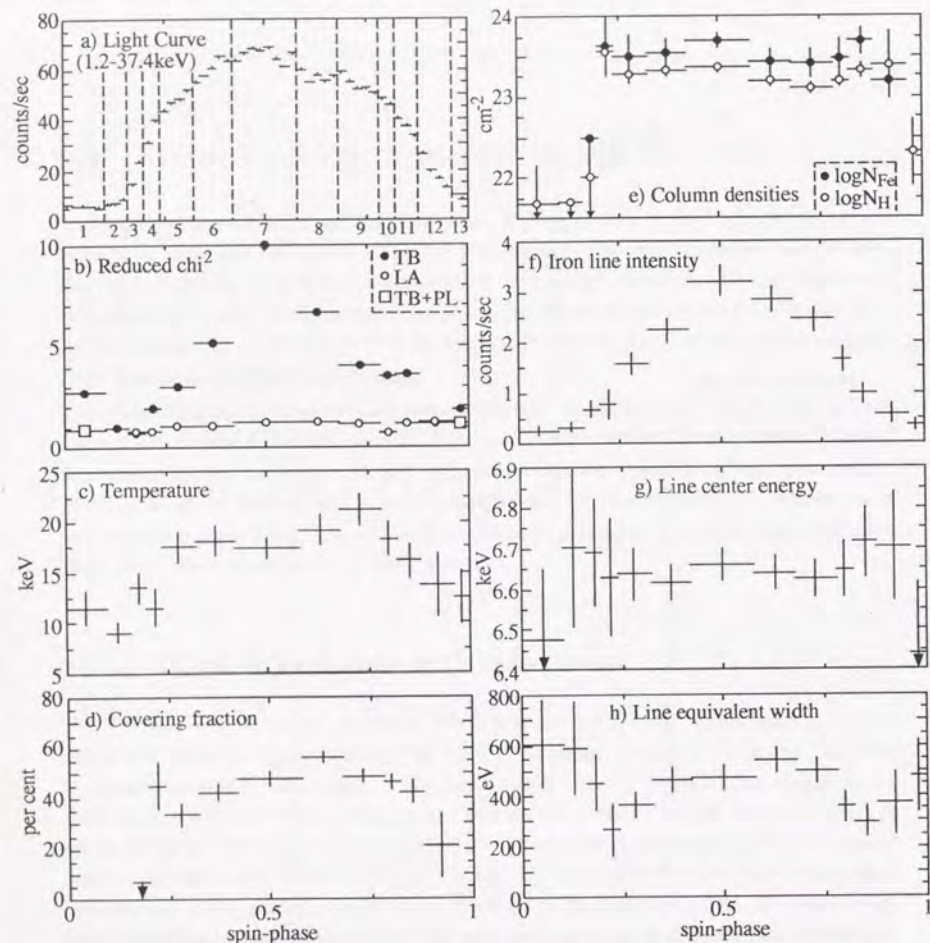
Figure 5.16: Variation of the spectral parameters of AM Her with the spin-phase.

tried for all the phases. We fixed the iron K-edge absorption energy at $E_{edge} = 8.25$keV which is obtained from the fit of the spin-phase average spectrum (section 5.4), and N'_H and N_{Fe} are set free to vary independently. We omit photoelectric absorption of the less-absorbed component since we have obtained only the upper limit from the spin-phase average spectrum. As seen from figure 5.16(b), leaky absorber model has been successful for most phases including the rise, the pulse-peak and the decline phases.

However, the fits are not improved significantly for phase 1 and 13 which correspond to the

pulse-bottom phase. Figure 5.17(a) shows the result of Model-1 fit to the summed spectrum of phase 1 and 13. As clearly seen, there remains systematic residual in energy band below ~5keV, reminiscent of the pulse-peak spectrum of EX Hya. Therefore, we have attempted to fit the summed spectrum with Model-1 plus either power-law, thermal bremsstrahrung, or blackbody. The result of the fit with thermal bremsstrahlung as a soft component is shown in figure 5.16(b), and obtained best fit parameters with all these models are listed in table 5.13.   The summed pulse-bottom spectrum can, as in the pulse-peak spectrum of

Table 5.13: The best fit parameters of the pulse-bottom phase spectrum of AM Her.

Model	Thermal Brem.			Soft Comp.		Iron line		χ^2_ν (d.o.f.)
	Norm.[a]	Temp.[b]	$\log N_H$ [c]	Norm.[a]	α [d]	Int.[e]	Energy[b]	
Model-1	0.32±0.01	8.0±0.5	< 21			0.8±0.2	6.59±0.13	5.01(31)
TB+PL	0.26±0.01	11.8±1.0	21.7±0.3	3.0±0.5	5.3±0.2	0.8±0.1	6.51±0.12	1.02(29)
TB+BB	0.28±0.04	10.8±1.9	21.8±1.2	20±10	0.29±0.06	0.8±0.2	6.53±0.14	0.99(29)
TB+TB	0.27±0.01	11.2±0.9	21.6±0.4	4.4±0.8	0.51±0.03	0.8±0.1	6.52±0.12	1.00(29)

a: In unit of 10^{-4}photons s^{-1} cm^{-2} keV^{-1}. b: In unit of keV.c: In unit of cm^{-2}. d: Photon index. e: In unit of 10^{-2}photons s^{-1} cm^{-2}.

EX Hya, be represented with Model-1 plus either blackbody, thermal bremsstrahlung, or power-law with almost the same reduced χ^2 values, and resultant temperature of the hard component is unaffected by the selection of the soft component model. The soft component is visible in phase 1 and 13, and we obtain no evidence of its existence, for example, in phase 2 with almost the same source intensity level as phase 1 (figure 5.16(a)). Origin of the soft component is discussed together with that of EX Hya in chapter 6.

Based on the discussion above, we use leaky warm absorber model for phase 4 through 12, Model-1 for phase 2 and 3, and Model-1 plus thermal bremsstrahlung for phase 1 and 13. Temperature of the soft thermal bremsstrahlung is fixed at the value obtained from the fit of the summed spectrum, 0.51keV. Resultant best fit parameters with these models are illustrated in figure 5.16(c)–(h). Hydrogen and iron column densities at the phases for which leaky absorber model is applied are those of the absorbed component, and hydrogen column densities at the other phases are those of thermal bremsstrahlung continuum.

5.5.3   Spin-modulated Components

As shown in figure 5.3, the intensity spin modulation of AM Her is characterized by the large energy independent modulation amplitude. In addition as seen from figure 5.16, hydrogen column density and CF are larger in the pulse-peak, which reduces the modulation amplitude a little in lower energies. Therefore, AM Her shares the common properties of the intensity
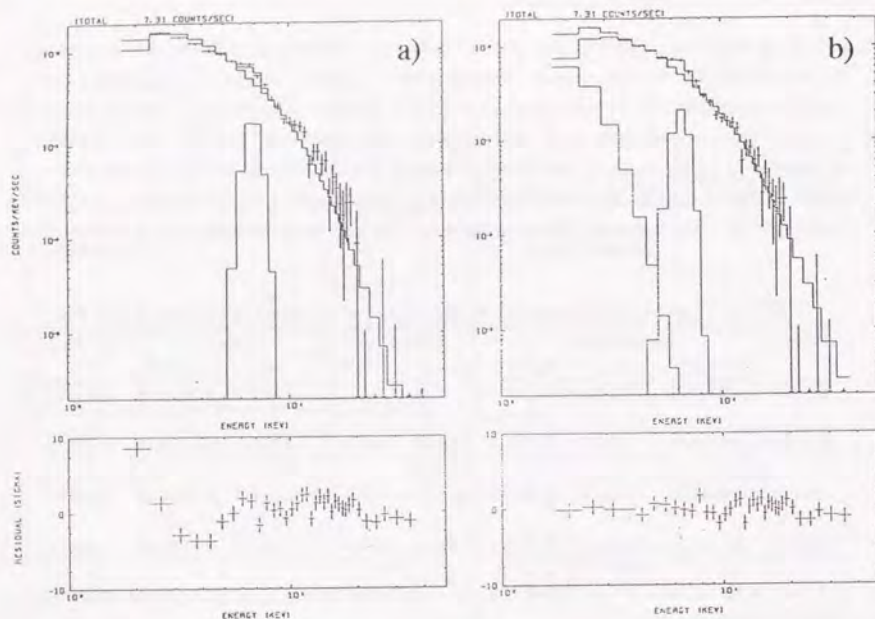
Figure 5.17: Spectral fit of the pulse-bottom spectrum of AM Her. (a) Model-1 ($\chi^2_\nu = 5.01$). (b) Two thermal bremsstrahlung continua with iron line ($\chi^2_\nu = 1.00$).

spin modulation among polars. The small dip around $\phi = 0.6$ is, as pointed out in section 5.1, attributable to photoelectric absorption since CF shown in figure 5.16(d) takes the largest value at the phase of the dip.

Nevertheless, there are following reasons which make SC-ratio of AM Her significantly different from that of the other polars; (1) as explained in the previous subsection in detail, there is a soft component in the pulse-bottom phase, which reduces modulation amplitude in lower energies; (2) temperature is higher in the pulse-peak, which enhances the modulation amplitude in higher energies. We would like to remark on the second point. As the magnetic field of the white dwarf is phase-locked in the binary system in polar, accretiong matter is expected to favour the pole pointing to the secondary star. Therefore, it is possible that temperature modulation in figure 5.16(c) is generated through partial eclipse of a single accreting pole, and therefore, the observed temperature modulation may suggest the inhomogeneity of the single emission region. If this is the case, it can be used to test various theoretical models of the hard X-ray emission region so far presented (chapter 2). In chapter 6, this point is further investigated by taking the geometrical constraint into consideration.

5.6   Iron Line Emission from MCVs

5.6.1   Iron Line Emission Processes

The electron transitions between K-shell and the other shells in iron are the most predominant line emission process in hard X-ray energy band above 2keV, which is observed from various kind of sources— normal star binaries, neutron star binaries, supernova remnants, clusters of galaxies, Seyfert galaxies *etc.*— as well as CVs. Among various lines, the strongest emission line is generated through the electron transition from L to K-shell, which is usually referred to as K_α line, followed by K_β line due to the transition from M to K-shell. In figure 5.18, we show the center energies of K_α and K_β lines of iron as a function of the ionization state. As noticed from this figure, we can infer the degree of ionization of the
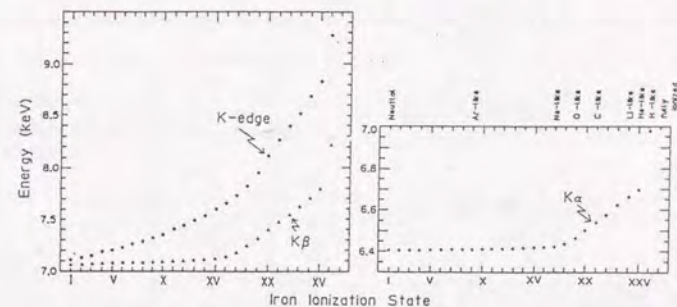

Figure 5.18: Iron line center energies as a function of the ionization state (Makishima 1986).

iron line emitter by measuring the line center energy. Another important information comes from the equivalent width of the line, which is defined as the ratio of the line intensity to the continuum intensity per unit energy interval at the line center energy. Equivalent width is more useful than the line intensity itself since it is independent of the distance to the source which sometimes contains a large uncertainty.

K-shell ionization of iron is caused by the collision with high energy particles or the X-ray irradiation. The iron line emissions from an optically thin plasma in thermal collisional equilibrium have been presented by a number of authors (for example Masai 1984, 1991, Makishima 1986, Tsunemi *et al.* 1986, Okumura *et al.* 1988). In figure 5.19, we show the degree of ionization of iron and expected equivalent width of the emission line as a function of plasma temperature. As shown in figure 5.19 (left panel), the most dominant ionization species is FeXXV, the helium-like iron, for plasmas with temperatures of a few keV. For hotter plasma, FeXXVI, the hydrogen-like iron cannot be neglected. FeXXV and FeXXVI emit $K\alpha$ lines with energies 6.70keV and 6.97keV, respectively.

On the other hand, K-shell ionization with the X-ray irradiation is investigated by Kallman & McCray (1982) (see also Krolik & Kallman 1984). Assuming thermal bremsstrahlung with temperature of 10keV as the illuminating X-ray source, they concluded that the ionization state of optically thin irradiated gass is determined solely with so-called ξ parameter defined as $\xi = L_X/n_H r^2$, where L_X/r^2 means the X-ray flux at the position of the irradiated matter, and n_H is the number density of hydrogen of the irradiated gass. In figure 5.20(a), we show the ionization state of iron as a function of ξ (Kallman & McCray 1982). If we take a typical condition around a MCV, *i.e.* $L_X \sim 10^{33}$erg s^{-1}, $n_H \sim 10^{15}$cm^{-3}, and $r \geq 10^8$cm, we obtain $\xi \leq 10^2$. Therefore, the ionization state of iron atoms in the X-ray irradiated gas is expected to be less that FeXX from figure 5.20, and hence the fluorescent iron lines should appear at $\sim$6.4keV (from figure 5.18). This energy can be distinguished with the LAC from the $\sim$6.7–6.9keV iron line from thermal plasmas with $kT > 10$keV. Inoue (1986) have calculated expected equivalent width of iron K_α line emission via fluorescence from cold gas irradiated by X-ray as a function of hydrogen column density of irradiated gass. Results are shown in figure 5.20(b).   He has assumed a power-law spectrum with photon index of
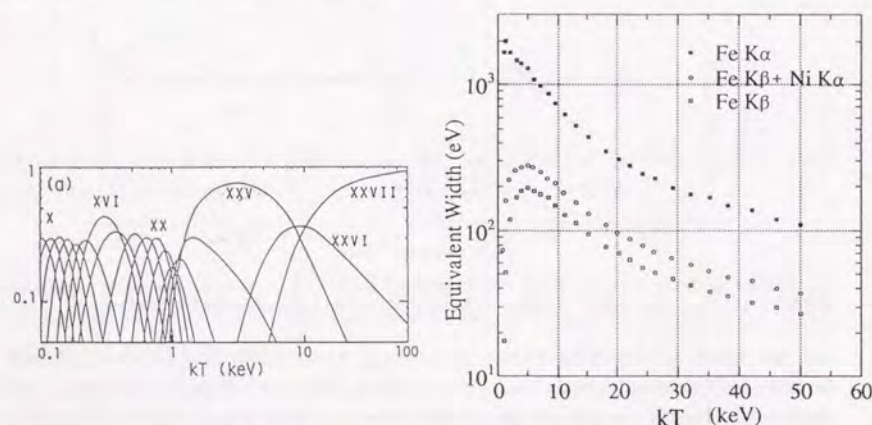

Figure 5.19: Ionization state distribution as a function of plasma temperature (Makishima 1986), and expected equivalent width of iron line (Masai 1991) from thermal collisional equilibrium plasma with solar abundances.

1.1 as an incident X-ray spectrum, and derived equivalent width in various geometries of irradiated matter as shown in figure 5.20. One general consequence is that the equivalent width should be strongly correlated with the column density of the absorber, N_H, since the fluorescing matter is also expected to take part in photoelectric absorption.

Therefore, we can investigate physical state of the iron line emitter, its site, and even more, its geometry by measuring the line center energy and equivalent width.
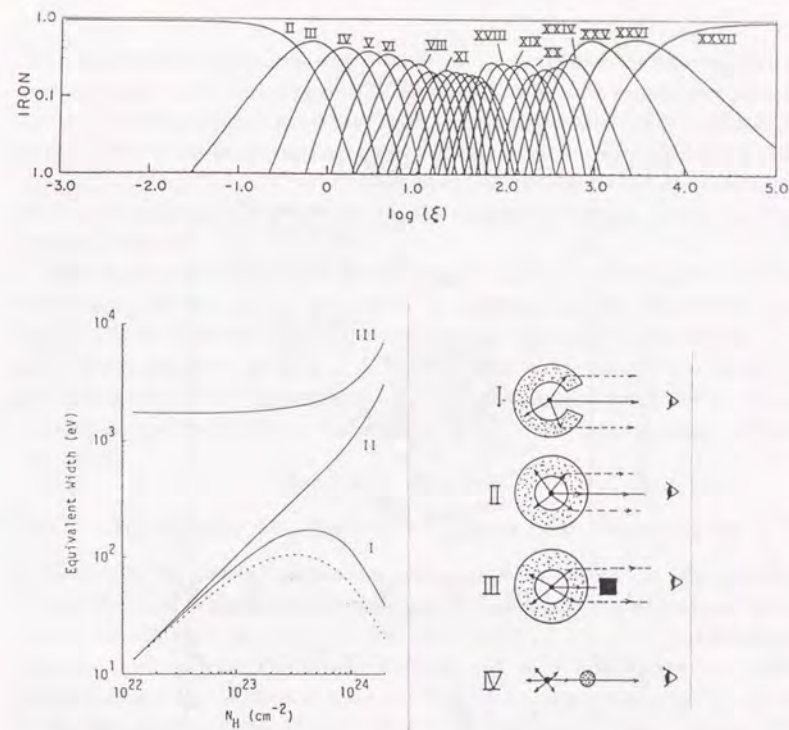
Figure 5.20: Ionization state distribution of iron as a function of so-called ξ parameter (Kallman & McCray 1982), and expected equivalent width of iron line from matter irradiated by X-ray (Inoue 1986).

5.6.2   Equivalent Width and Center Energy of the Iron Line

In figure 5.21, the equivalent widths and center energies of the iron line emission obtained from spin-phase average spectra are plotted against the plasma temperatures. The lines indicate the equivalent width (Masai 1991) and line center energy (Okumura *et al.* 1988) expected for plasma of solar abundance in an ionization equilibrium. As clearly seen from this figure, observed equivalent widths tend to decrease with increasing plasma temperature, which indicates that a significant amount of iron line emission comes from optically thin hot plasma. In addition, spectra undergoing stronger photoelectric absorption generally show larger equivalent widths than those with smaller absorption with almost the same continuum temperature. This fact suggests that the iron line emission via fluorescence from matter irradiated by X-ray also contributes significantly to the observed iron line emission.
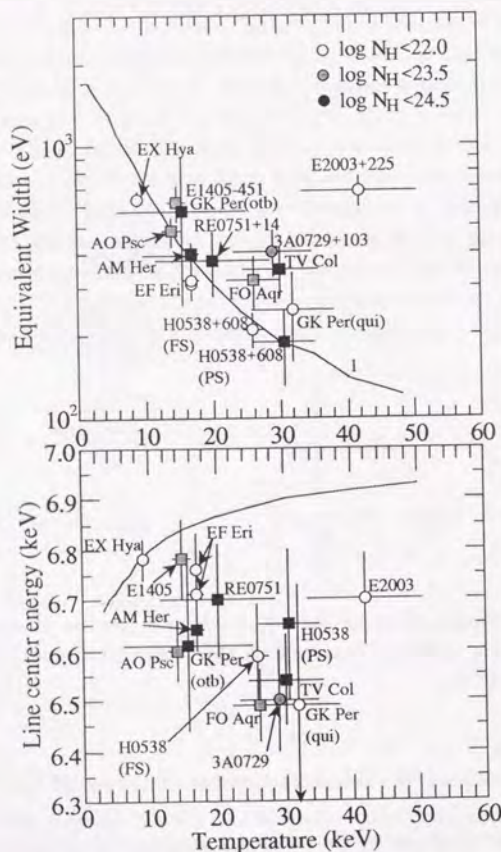
Figure 5.21:
(a) Observed iron line equivalent width and (b) line center energy derived from the model fitting of the spin-phase average spectra. Circle and square represent the spectra fitted well with Model-1 and leaky absorber model, respectively. Equivalent width and line center energy expected for plasma in collisional ionization equiliblium are shown in each panel.

The contribution from cold fluoresing matter is also suggested from the following facts. First, as shown in the lower panel of figure 5.21, the observed line center energies are between that expected from hot plasma (6.8–6.9keV) and that expected from X-ray irradiated matter (6.4keV). In addtion, some sources show significantly larger line equivalent width than that expected only from plasma in collisional ionization equilibrium. Therefore, we conclude that the iron line emission from MCVs are a mixture of that from thermal plasma and that from fluorescing matter.

We remark that equivalent width of EX Hya is significantly below the line of collisional ionization equilibrium plasma, although its line center energy is consistent with that from thermal plasma in collisional ionization equilibrium. As the spectrum of EX Hya undergoes photoelectric absorption with $N_H \leq 10^{22}$, the observed iron line emission is expected to be purely of thermal plasma origin (figure 5.20). Therefore, it is suggested that the abundance of heavy elements is deficient in the accreting matter of EX Hya compared with the solar abundance.

5.6.3   Spin-phase Dependences of Iron Line Parameters

In figure 5.22, we have plotted line intensities, equivalent widths and line center energies of the pulse-peak and the pulse-bottom phases. In polar, the line intensity is appearently modulated with the white dwarf rotation, whereas EW is not. In intermediate polar, on the other hand, both the line intensity itself and EW show approximately no modulation. This is natural since the emission measure ($\propto$ continuum normalization) shows no, or little if any, spin modulation (section 5.3). In the three intermediate polar systems, EX Hya, FO Aqr and AO Psc, the line intensity is a little larger in the pulse-peak phases. However in these sources, the continuum normalization is also larger in the pulse-peak by 10–30% (subsection 5.3.3 and 5.3.4). Therefore, EW becomes almost the same between the pulse-peak and the pulse-bottom. Although not constrained very well, the equivalent width of intermediate polars except RE0751+14 tend to be larger in the pulse-bottom phases. This is probably caused by the increase of contribution from fluorescing iron line emission due to the increase of N_H in the pulse-bottom phases (subsection 5.3.5). Line center energies are not constrained very well for a large number of MCVs.

We remark that the line intensity and equivalent width of RE0751+14, an intermediate polar, show different behaviour from the other intermediate polars. As described in subsection 5.3.3, temperatures of RE0751+14 in the pulse-peak and in the pulse-bottom are significantly different, which is like AM Her and H0538+608 (polars). The behaviour of the iron line parameters shown in figure 5.22 also resembles those of H0538+608.

5.6.4   Search for Iron K_β Emission

As mentioned in section 5.2.3, a clear iron K_β emission line is found in the spin-phase average spectrum of EX Hya, whereas acceptable fits are obtained without K_β emission for the other
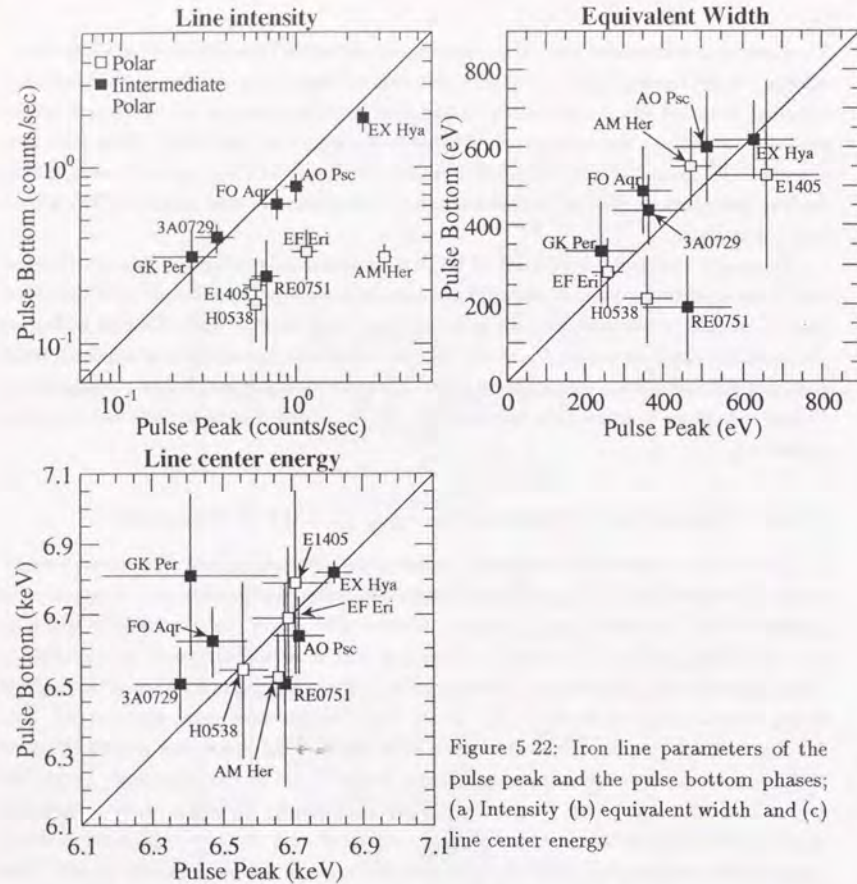
Figure 5 22: Iron line parameters of the pulse peak and the pulse bottom phases; (a) Intensity (b) equivalent width and (c) line center energy

sources In this subsection we search for iron K_β emission line from the other sources

We have attempted to fit the observed spin phase average spectra with the best fit contin uum model of each spectrum (either with Model 1 leaky absorber model or leaky absorber model with modified absorption according to eq(5 11)) including two Gaussian lines As no ticed from figure 5 18 the ratio of the center energies of K_β to K lines vary from 1 10 for the neutral iron to 1 19 to the hydrogen like iron In this analysis the ratio of the center energies of K and K_β lines is fixed at 1 15 since K_β emission line is expected to be significantly weaker than K line and its line center energy is probably not constrained well We assume that both lines are narrow As a result the intensity and the center energy of K line and the intensity ratio of K_β to K lines are set free to vary as for the iron line parameters In table 5 14 we summarize the results of two line fits to the observed spin phase average spec-

tra. For comparison, we also show the results of single line fits. We have obtained evidence

Table 5.14: Results of the fits including iron K_β emission line.

Source	Model[a]	Single line			Two lines			
		Int.[b]	Energy[c]	χ^2_ν	Int.[d]	Energy[e]	K_β/K_α [f]	χ^2_ν
AM Her	LWA	4.1±0.4	6.64±0.04	0.77(30)	4.2±0.4	6.65±0.06	0.12±0.07	0.85(29)
EF Eri('88)	MD1	2.1±0.2	6.76±0.07	1.06(32)	2.1±0.2	6.72±0.09	<0.22	1.04(31)
EF Eri('91)	MD1	1.6±0.2	6.71±0.09	1.06(32)	1.4±0.3	6.55±0.14	0.37±0.20	0.78(31)
H0538+608(PS)	LWA	0.7±0.2	6.65±0.15	0.99(29)	0.7±0.2	6.56±0.25	<0.63	0.90(28)
H0538+608(FS)	MD1	1.1±0.2	6.59±0.10	0.81(26)	1.1±0.2	6.59±0.10	< 0.20	0.81(25)
E1405−451	LCA	1.1±0.2	6.78±0.08	0.96(30)	1.1±0.2	6.77±0.08	<0.08	0.97(29)
GK Per(Qui)	MD1	0.7±0.2	6.49±0.24	0.74(29)	0.6±0.3	6.42±0.41	<0.79	0.90(28)
GK Per(Otb)	LCA	23± 7	6.61±0.17	1.16(27)	23± 6	6.61±0.17	<0.07	1.16(26)
TV Col	LWA	1.9±0.3	6.54±0.09	1.16(27)	1.9±0.1	6.58±0.05	<0.08	1.16(26)
EX Hya	MD1	5.6±0.1	6.82±0.04	1.77(32)	5.4±0.3	6.75±0.05	0.15±0.07	1.15(31)
FO Aqr	LWA	1.4±0.3	6.49±0.07	0.87(30)	1.5±0.3	6.53±0.11	<0.29	0.96(29)
AO Psc	LWA	2.1±0.3	6.60±0.06	0.56(25)	2.1±0.3	6.57±0.10	<0.27	0.58(24)
3A0729+103	MD1	1.0±0.2	6.50±0.10	1.12(32)	0.9±0.2	6.34±0.17	<0.51	1.10(31)
RE0751+14	LCA	1.2±0.3	6.70±0.11	1.13(29)	1.2±0.4	6.66±0.16	<0.35	1.15(28)

a: Best fit model for each spectrum. MD1 = Model-1; LCA = Leaky Cold Absorber; LWA = Leaky Warm Absorber. b: Line intensity of the iron line in unit of 10^{-4}photons s^{-1} cm^{-2}. c: Line center energy of the iron line in unit of keV. d: Line intensity of the iron K_α line in unit of 10^{-4}photons s^{-1} cm^{-2}. e: Line center energy of the iron K_α line in unit of keV. f: Intensity ratio of K_β to K_α lines.

of K_β emission line from AM Her and EF Eri('91) as well as EX Hya. The obtained K_β line intensity of EX Hya is $(0.8 \pm 0.4) \times 10^{-4}$phs s^{-1}cm^{-2}, in agreement with the value listed in table 5.3. According to Okumura *et al.* (1998), the intensity ratio of K_β to K_α emission lines from plasma in collisional ionization equilibrium with temperature above 10keV is expected to be 0.15–0.2. On the other hand, in the case of K-shell ionization of cold iron by X-ray irradiation, the ratio becomes $\sim$ 0.12. Therefore, the intensity ratios obtained for AM Her and EF Eri as well as for EX Hya are reasonable. For the other sources, we have obtained crude upper limits for K_β emission line, and they are mostly consistent with the theoretical prediction. Observations with detectors with a sufficient energy resolution is necessary to further investigate K_β emission line from MCVs.

Finally we remark that the center energies, intensities, and resultant equivalent width obtained with single line fits can be regarded as those of iron K_α emission line except EX Hya, since the line center energies and the intensities are not different between the two models within statistical errors as seen from table 5.14.

Chapter 6

Physics Interpretations of MCVs

6.1   Continuum Emission

6.1.1   Origin of the Hard X-ray Emission

As described in section 5.2.3, spin-phase-average spectra of Group-1 sources are fitted well with the thermal bremsstrahlung model with iron line emissions. Even for Group-2 sources, the continuum spectrum favors the thermal bremsstrahlung as an underlying process rather than the non-thermal power-law model. Also, as mentioned in section 5.2.4, the spin-phase spectra of AM Her and H0538+608(FS) above 10keV can be fitted with thermal bremsstrahlung model, but not with the power-law model. These results imply that the hard X-ray emission of MCVs originates from a hot, optically thin thermal plasma. Observed plasma temperatures (10–40keV) roughly correspond to the gravitatinal energy accreting matter made of solar abundance gains on the surface of the white dwarf surface. This strongly suggests that the plasma is formed through the standing shock wave in the accretion column near the white dwarf surface. This picture has been, as mentioned in chapter 2, proposed by a number of authors (Hoshi 1973; Aizu 1973; Fabian, Pringle & Rees 1976; Katz 1977; Frank, King & Lasota 1983; Imamura & Durisen 1983; see also Lamb 1985 and reference therein). Observationally, evidence of optically thin thermal spectra was obtained only from AM Her (Rothschild *et al.* 1981) and EF Eri (White 1981) with the *HEAO*-A2 and A4 experiments. *Ginga* observations strongly suggest that the optically thin thermal emission is a common feature among MCVs.

In table 6.1, we summarize observed flux and luminosity for each source in 1.2–37.4keV band. The hard X-ray luminosity is calculated with the following equation.

$$L = \frac{64\pi}{3}\sqrt{\frac{1}{2}}\frac{e^6}{m_e c^2 h}\sqrt{\frac{kT}{m_e c^2}}\left(\sum_Z n_e Z^2 n_Z V\right), \tag{6.1}$$

where V is the volumn of the emission region and n_e and n_Z are the densities of electron and ion with the electric charge of Z, respectively. The quantity in the parenthesis is so-called the "emission measure (EM)". EM is calculated with the observed flux if the distance to the source is known.

Table 6.1: Parameters necessary to determine the size and density of the emission region.

Source	distance[a]	flux[b]	luminosity[c]	Source	distance[a]	flux[b]	luminosity[c]
Polars				Intermediate Polars			
AM Her	75	1.94	1.32 ± 0.26	GK Per(Qui)	525	0.56	18.4 ± 3.7
EF Eri('88)	>100	1.25	>1.50	(Otb)	525	10.5	350 ± 160
('91)		0.93	>1.12	TV Col	160-500	1.13	3.48-34.0
H0538+608(PS)		0.80	(0.96)	EX Hya	60-190	1.43	6.19-62.1
(FS)		1.02	(1.22)	FO Aqr	200-640	0.97	4.68-47.9
E1405–451	86	0.32	0.28 ± 0.06	AO Psc	100-750	0.72	0.86-48.5
E2003+225	>400	0.23	>4.47	3A0729+103	800^{+240}_{-120}	0.46	$35.0^{+22.4}_{-9.7}$
				RE0751+14		0.64	(0.76)

Quantities in parentheses are derived by assuming a distance of 100pc.

a: In units of pc.

b: In units of 10^{-10}erg s^{-1}cm^{-2} in 1.2–37.4keV.

c: In units of 10^{32} erg s^{-1} in 1.2–37.4keV.

6.1.2 Masses of the White Dwarfs

Since we have established the existence of hot plasma generated by a standing shock near the white dwarf surface, it is now possible to estimate the mass-to-radius ratio of the white dwarf from the plasma temperature. The state of gass below and above the shock is related with Rankine-Hugoniot relations. Under the assumption of the strong shock and $T = 0$ in the preshock region, the postshock temperature T_S is expressed with the pre-shock velocity as

$$kT_S = \frac{3}{16}\mu m_H v^2.$$

Assuming free fall accretion onto the white dwarf, we obtain

$$kT_S = \frac{3}{8}\frac{GM}{R}\mu m_H. \tag{6.2}$$

Here, we have assumed that the shock occurs just on the surface of the white dwarf. M and R mean the mass and the radius of the white dwarf, and m_H means the mass of hydrogen. μ represents the mean molecular weight, 0.62, for matter with the solar abundance. Furthermore if we employ the standard mass-radius relation of the white dwarf

$$R = 5.5\times10^8\left(\frac{M}{M_\odot}\right)^{-1/3}, \tag{6.3}$$

the mass of the white dwarf is estimated as

$$M = 0.45\left(\frac{kT_S}{20\text{keV}}\right)^{3/4} M_\odot. \tag{6.4}$$

In table 6.2, we summarize the mass of the white dwarfs derived from this equation. For the

Table 6.2: Masses of the white dwarfs determined with eq(6.4).

Source	Used[a] spectrum	Temperature (keV)	Mass ($M_\odot$)	Source	Used[a] spectrum	Temperature (keV)	Mass ($M_\odot$)
Polars				Intermediate polars			
AM Her	P	21.2 ± 1.6	0.44	GK Per	A	32.0 ± 6.1	0.55
EF Eri	A	16.9 ± 0.6	0.39	TV Col	A	30.0 ± 5.5	0.52
H0538+608	P	34.6 ± 3.4	0.63	EX Hya	A	8.9 ± 0.2	0.24
E1405–451	A	14.7 ± 1.3	0.33	FO Aqr	A	26.2 ± 4.0	0.49
E2003+225	A	41.9 ± 8.4	0.66	AO Psc	A	14.0 ± 1.3	0.32
				3A0729+103	A	28.9 ± 5.8	0.50
				RE0751+14	P	20.1 ± 7.7	0.31

a: P = pulse-peak spectrum; A = spin-phase average spectrum.

sources which show different temperature between the pulse-peak and the pulse-bottom in spin-phase spectral analysis, we have adopted the higher temperature.

It should be remarked, however, that the masses obtained with this method give only the lower limits since,

(a) the shock may not always occur just on the surface of the white dwarf. According to the standard model for the hard X-ray emission region (for example Aizu 1973) the shock height is estimated to be of order $0.1R$.

(b) the post shock plasma may cool down as it descends the accretion column via radiation, electron conduction etc. It is possible that we observe somewhat cooled part of the emission region.

As noted in subsection 2.2.2, Mukai & Charles (1987) derived the mass of the white dwarf in AM Her and E2003+225 as $0.99M_\odot$ and $0.58M_\odot$, respectively with typical error of $0.2M_\odot$. Our mass lower limits are consistent with their values.

6.1.3 Scale and Density of the X-ray Emission Region

Since we have obtained the temperature of the emission region, we can evaluate the emission measure (EM) (see eq(6.1)) if the distance to the source is known. This gives a constraint between the size and the density of the hard X-ray emission region. Another constraint comes from iron column density estimated from the depth of K-edge absorption.

$$N_{Fe} = n_{Fe}l, \tag{6.5}$$

Table 6.3: Parameters necessary to determine the size and density of the emission region.

Source	EM [a]	$\log N_{Fe}$ [b]
Polars		
AM Her	0.81±0.16	23.16±0.10
H0538+608(PS)	(0.40)	23.04±0.24
Intermediate Polars		
TV Col	1.61-15.7	23.43±0.16
FO Aqr	2.84-29.1	22.90±0.29
AO Psc	0.60-33.9	22.63±0.75

Quantities in parentheses are derived by assuming
a distance of 100pc.

a: Emission Measure in units of 10^{55} cm^{-3}.

b: Iron column density but converted to equivalent
hydrogen column density under the assumption of
solar abundances. In units of cm^{-2}.

where n_{Fe} is the density of iron and l represents the length of the absorbing region along the line of sight. As described in section 5.4, K-edge absorption due to highly ionized iron is detected from five sources. Since the best fit K-edge absorption energies exceed 8keV for all the 5 sources, light elements such as oxygen, neon, silicon which significantly contribute to the low energy photoelectric absorption are completely ionized, whereas the K-shell electron of iron still remains (Kallman & McCray 1982). Therefore, observed K-edge absorption is considered to be caused by iron in the hard X-ray emission region itself, and thus l in eq(6.5) is equal to the length of the emission region along the line of sight. In table 6.3, we summarize the emission measure and the iron column density.

The spin-phase average spectra is related to the average of l over various lines of sight. Therefore we may as well assume that $V \sim l^3$. We obtain, after converting n_{Fe} into n_H assuming the solar abundance, the following relations.

$$EM = n_H^2 l^3. \tag{6.6}$$
$$N_{Fe} = n_H l. \tag{6.7}$$

Apart from H0538+608 the distance to which is uncertain, we obtain relations of the density, n_H, and the dimension, l, of the emission region (see figure 6.1). Although densities and dimensions scatter in a wide range, it should be remarked that the dimension is generally believed to be less that the white dwarf radius, namely $\leq 10^8$cm. In figure 6.1, we have

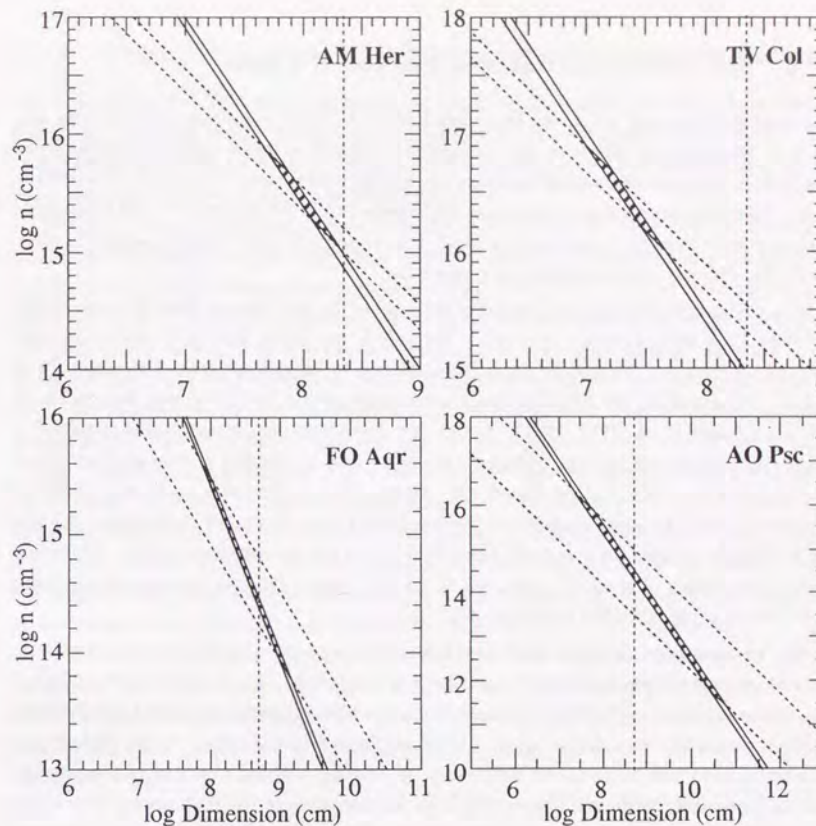Figure 6.1: The density and the dimension of the emission region of MCVs.

also indicated the radius corresponding to $1M_\odot$ white dwarf by the dotted vertical line. The hydrogen number density of the hard X-ray emission region is inferred to be 10^{15-16}cm^{-3} for the four MCVs. Finally, in the regime of $n = 10^{15-16}$cm^{-2} and $l \leq 10^8$cm, Thomson optical depth is of order 0.1, and the free-free optical depth is of order 10^{-12} for the temperature of ~10keV. These are consistent with the fact that the continuum spectrum has the shape of optically thin thermal bremsstrahlung.

6.1.4   Soft Component of AM Her and EX Hya

In subsection 5.3.2 and 5.5.1, we have found the soft X-ray component in EX Hya and AM Her. Since its intensity is clearly modulated by the white dwarf rotation, it is regarded with high cirtainty as originating from near the white dwarf surface. As already described in those subsections, estimation of the true spectral shape is difficult because the soft component dominates only in a few lowest energy bins. It is consistent with various spectral models: blackbody, thermal bremsstrahlung and power-law.

It is well-known that polars are generally brighter in soft X-rays than in hard X-rays (Osborne 1988 and references therein). The soft X-ray has a blackbody spectrum with temperature of a few tens of eV, and is considered to be emitted from the white dwarf surface. For example, the soft blackbody component with $kT \sim 40eV$ was detected from AM Her (Tuohy *et al.* 1979, 1981). Notice that the blackbody temperatures obtained in *Ginga* observations are an order of magnitude higher than the typical temperature of polars. This problem may, however, be resolved by invoking inverse Compton scattering of soft X-ray photons by high energy electrons in the postshock region. It should be remarked that the soft blackbody component has never been found from any intermediate polars. Therefore, further observation of the soft component of EX Hya with a detector with sensitivity below 2keV (for example, *ROSAT*) is meaningful.

On the other hand, since we have established that the hard component is expressed with thermal bremsstrahlung spectum, the soft component may be so, too. If this is the case, the implication is that an optically thin thermal plasma with temperature lower than the main emission region by two orders of magnitude is also formed on the surface of the white dwarf. This component will be useful to investigate the relation between the plasma temperature and the luminosity without being troubled by uncertainties in the distance to the sources or in the white dwarf masses. Anyway, further observations with a detector with good low-energy sensitivity is necessary to determine the spectral shape of this soft component.

6.2   Origin of the Spin Modulation

In this section, we attempt to understand the accretion-pole geometry of polars and intermediate polars using the properties of spin modulations of the X-ray intensity. The spin modulation of the X-ray intensity of polars is characterized by the large energy-independent modulation amplitude. That of intermediate polars, on the other hand, strongly depends upon the X-ray energy, and is caused by the variation of the amount of the photoelectric absorption along the line of sight. In the first two subsections, origins of these two properties will be understood in relation with the geometry. Based on these understandings, possible accretion geometries of polars and intermediate polars will be presented in the following two subsections.

6.2.1   Origin of the Energy-independent Modulation in Polars

The spin-modulated light curve of polars, as described in section 5.1 and 5.3, is characterized by the large energy-independent modulation amplitude (greater than 50%). The energy-independent modulation can be generated either by the electron scattering or by the occultation of the emission region by the white dwarf.

In the Thomson scattering regime, inhomogeneity in the electron column density of $\sim 10^{24} cm^{-2}$ is needed around the white dwarf in order to modulate the light curve by $\sim$50%. The hydrogen column density is, however, far short of $10^{24} cm^{-2}$ in the pulse-bottom spectra of polars. Notice that, however, the hydrogen column density can be far short of the electron column density if ions in the absorbing matter are highly ionized. As pointed out in section 5.6, there are two ways to cause the ionization; collision and photoionization by the X-ray irradiation. For the ionization to occur with collisions, plasma with temperature greater than 10keV is required. This temperature is comparable with that of the emission region. Therefore, one possibility is that the electron scattering occurs within the emission region itself. As already noted in section 5.4, however, the iron column density of the hard X-ray emission region deduced from the iron K-edge feature is at most $10^{23.4} cm^{-2}$, which is far short of that required. For the ionization to occur with the X-ray irradiation, on the other hand, hard X-ray luminosity of order 10^{35} erg s^{-1} is necessary for significant ionization of accreting matter (Kallman & McCray 1982), which is also unlikely (table 6.1).

As a result, the energy-independent modulation of polars cannot be caused by the electron scattering. We conclude that the energy-independent modulation of polar is generated by the occultion of the emission region by the white dwarf itself. This picture is consistent with that derived from comparision of the linear polarization light curves and the hard X-ray light curves as described in subsection 2.5.2.

6.2.2   Origin of Photoelectric Absorption

As the energy-independent modulation of polars is caused by the occultation of the emission region by the white dwarf, the accreting pole most probablly points to the observer in the pulse-peak phase. As already pointed out by Norton & Watson (1989), the spectra of most intermediate polars observed with *EXOSAT* undergo photoelectric absorption with the hydrogen column density of order of $10^{23} cm^{-2}$. We have found that this is also the case in polars with *Ginga* observations, and the absorption is stronger in the pulse-peak phase than in the pulse-bottom phase. Therefore, photoelectric absorption in polars is naturally interpreted as due to the matter in the accretion column, and its optical depth is larger along the accretion column.

As the geometry of mass accretion is expected to be essentially the same between polars and intermediate polars, it is natural to consider that the photoelectric absorption in intermediate polars occurs also in the accretion column, and the accreting pole points to the observer in the pulse-bottom phase, for the photoelectric absorption is stronger in the

pulse-bottom phases. This picture is consistent with that drawn originally by Rosen, Mason & Córdova (1988) (see also Hellier *et al.* 1989, 1990, 1991), and not with King & Shaviv (1984); see subsection 2.5.2. We conclude that it is natural to consider that the photoelectric absorption of both polars and intermediate polars occurs in the accretion column, and its optical depth is larger along the accretion column than across it.

6.2.3   Accretion-pole Geometry of Polars

In polars, the mass is expected to accrete mainly a magnetic pole pointing to the secondary star as the magnetic field of the white dwarf is phase-locked in the binary system. As the hard X-ray intensity monotonically increases with the visible fraction of the volumn of the emission region, the spin modulation of the X-ray intensity is caused by the eclipse of this mainly accreting pole. Even when mass accretion is shared almost evenly between the two magnetic poles, it probably proceeds along common magnetic field lines of force connecting the two poles. Therefore, the eclipse of the emission regions still plays an important role on the spin modulation of the hard X-ray intensity because two emission regions on the white dwarf surface are in general separated by an angle less than 180°.

As described in section 5.3, temperature modulation is not significant in EF Eri and E1405–451. This can be interpreted that the mass accretes onto a single pole, or only one accreting pole is visible from the observer in EF Eri and E1405–451. On the other hand, as presented in section 5.3 and 5.5, significant temperature difference between the pulse-peak and the pulse-bottom is detected from H0538+608 and AM Her. This may be suggest the accretion proceeds onto the two magnetic poles or a significant inhomogeneity in a single emission region. The spin modulation of the temperature is further examined for H0538+608 and AM Her separately in the next section.

6.2.4   Accretion-pole Geometry of Intermediate Polars

In intermediate polars, the magnetic field of the white dwarf is not phase-locked in the binary system. Because of this asynchronism, accreting matter is expected to be distributed almost evenly between two magnetic poles, and to form two equivalent emission regions which are separated by an angle 180° on the surface of the white dwarf. If so, the eclipse of the emission region(s) by the white dwarf is expected to have rather minor effect on the spin modulation of the X-ray intensity since the eclipse of one emission region is followed by the appearence of the other emission region. Alternatively, the spin modulation of the X-ray intensity is mainly caused by the photoelectric absorption due to matter in the accretion column. This naturally explains the stronger photoelectric absorption in the pulse-bottom phases in intermediate polars.

As shown in table 5.5, the spin modulation of the X-ray intensity of the two intermediate polars, GK Per and 3A0729+103, is consistent with this picture; the normalization of the thermal bremsstrahlung model spectrum, which is proportional to EM, and is the measure

of the amount of the energy-independent modulation, is not different between the pulse-peak and the pulse-bottom spectra. The difference in the normalization (sum of the normalizations for Group-2 sources), however, amounts to 20–40% in the four intermediate polars, EX Hya, FO Aqr, AO Psc and RE0751+14 (table 5.5, 5.6 and 5.9). In the next section, we will examine the energy-independent modulation separately for these four intermediate polars. Here we present some possibilities to cause energy-independent intensity modulation in intermediate polars.

First, since spectra of most intermediate polars show photoelectric absorption with hydrogen column densities of order $10^{23} \mathrm{cm}^{-2}$, Thomson scattering by electrons included in the photoelectric absorber may contribute significantly to the spin modulation of the light curve (Thomson optical depth becomes of order 0.1). Second, even if two emission regions with almost the same mass accretion rate are separated by 180°, the total volumn of the emission regions becomes significanty larger when we observe the emission regions from the side because both emission regions are visible in this phase provided that the emission regions have non-negligibe height compared with the white dwarf radius. This will be referred to as "IP-type modulation" in the next section (IP means Intermediate Polar). Finally, if the mass distribution between two magnetic poles is not completely even, the eclipse of the mainly accreting pole causes the energy-independent modulation. This will be referred to as "P-type modulation" in the next section (P means Polar).

6.3   Accretion-pole Geometry of Individual Sources

6.3.1   H0538+608

Mason *et al.* (1990) performed extensive optical polarimetric observations of H0538+608 for more than 3 years. They found that, in some spin cycles, the sign of circular polarization changes abruptly, whereas it is unchanged in other cycles throughout. Ishida *et al.* (1991a) found that the rise of the hard X-ray light curve occurred simultaneously with the change of the sign of circular polarization. This result confirms the suggestion made by Mason *et al.* (1990) that there are two accretion spots on the white dwarf; one is visible throughout the spin cycle and radiates circularly polarized optical emission with the sign unchanged throughout a spin period; the other is eclipsed during a part of a spin period and radiates polarized emission with the opposite polarity. Mass continuously accretes onto the non-eclipsing spot, and the sign of polarization changes only when mass accretes also onto the eclipsing spot. As seen from figure 4.3, the spin modulation of H0538+608 is not persistent, in agreement with impersistence of alternation of the sign of the circular polarization. Also the observed temperature in FS (table 5.3) when mass accretes onto the non-eclipsing pole only, agrees with that of the pulse-bottom in PS (table 5.9) when mass accretes on the eclipsing spot but it is behind the white dwarf.

From the optical polarimetry and the hard X-ray observations, and the analyses thereon,

we can conclude that mass accretes onto both magnetic poles in H0538+608, and the spin-modulation in hard X-rays is caused by the eclipse of the eclipsing pole only. The non-eclipsing pole continuously emits the hard X-ray.

6.3.2   AM Her

The temperature of AM Her appears to be modulated with the white dwarf rotation (figure 5.15 and 5.16(c)).

One possible interpretation is that all the hard X-ray emission of AM Her originates from a single emission region, and a part of it is visible even during the pulse-bottom phase due to partial eclipse by the white dwarf. In this case, figure 5.16(c) means that there is a significant temperature inhomogeneity in the emission region. Note that along this interpretation, the temperature shown in figure 5.16(c) is that averaged over the visible part of the emission region at a given spin phase.

Alternatively, it is also possible that there are two accretion poles with different temperatures as in H0538+608, and mixture of emissions from the two poles changes with spin phase. As a matter of fact, behaviour of hydrogen column density, CF, and temperature of the pulse-peak and the pulse-bottom resembles those of H0538+608 in PS, in which mass from the secondary accretes onto two magnetic poles (see previous subsection).

In AM Her, it is difficult to discriminate these two possibilities with the observation. We have, however, detected the soft X-ray component in the pulse-bottom phase. In the *EXOSAT*-LE observation (Heise *et al.* 1985), strong soft X-ray component was detected around the hard X-ray pulse-bottom phase when AM Her was in so-called "reverse mode", in which the hard and the soft X-ray intensity modulations are anti-phased by half a white dwarf rotation period. This *EXOSAT* result can be interpreted that the magnetic field configuration is approximately dipolar, and the soft component is most likely emitted from the second accreting pole. As the soft X-ray component appears also in the hard X-ray pulse-bottom phase in the *Ginga* observation, its intensity can be regarded as the indicator of the visibility of the second emission region. If so, the hard X-ray intensity of the second emission region is maximally ~10% of that of the main emission region, and may be negligible in the phases other than 1 and 13. As a result, it is concluded that the observed temperature gradient is generated solely in the main emission region.

Although we have found the temperature gradient in the emission region, however, the direction of it is still unclear since we do not know the shape of the emission region. For example, we show schematic view of two different types of emission regions in shape and the direction of the gradient in figure 6.2(a); one is a tall cylinder type emission region with Aizu-type temperature gradient (subsection 2.3.2), and the other is a flat, coin-shaped emission region with the highest temperature in the center. From geometirical considerations, it will be easily noticed that the expected spin modulation profile of the temperature is the same between these two types of the temperature gradient as shown in figure 6.2(b).
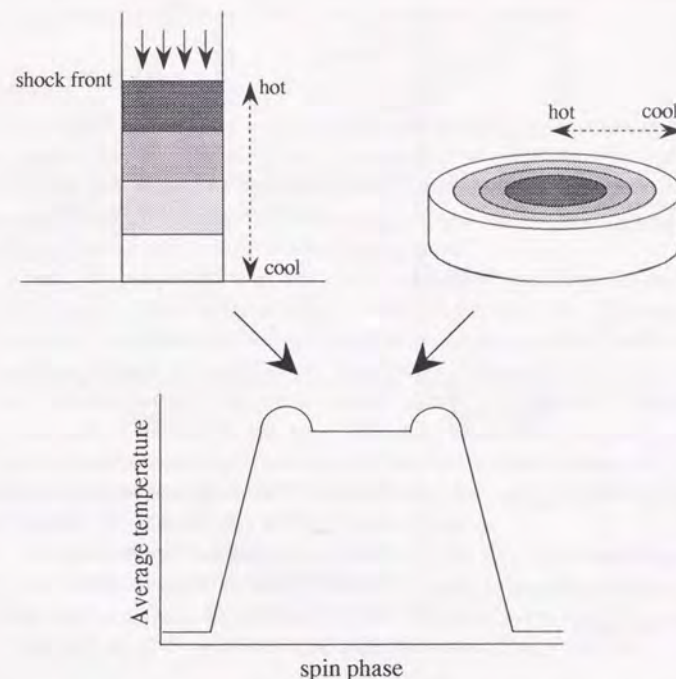
Figure 6.2: (a) Schematic view of the two emission regions with different temperature gradient and (b) the expected behaviour of the observed temperature with spin phase.

As described in section 5.4, we have observed the K-edge absorption feature of the highly ionized iron from 5 MCVs including AM Her. It may be possible to infer the shape of the emission region by utilizing the spin-phase-dependence of the column density of this highly ionized iron.

6.3.3   FO Aqr

Detailed spin-phase-resolved analysis was performed taking advantage of our high statistic observation of FO Aqr. Note that AO Psc shows the change of spectral parameters between the pulse-peak and the pulse-bottom similar to FO Aqr, as shown in table 5.9 and figure 5.12. Therefore, this analysis will give hints to understand the geometry also of AO Psc.
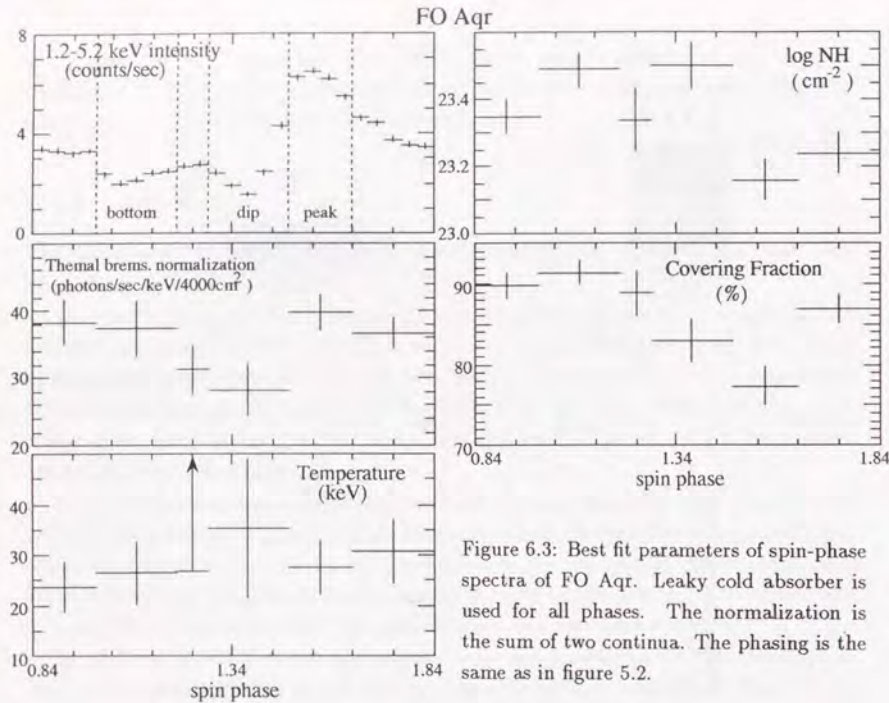
FO Aqr

Figure 6.3: Best fit parameters of spin-phase spectra of FO Aqr. Leaky cold absorber is used for all phases. The normalization is the sum of two continua. The phasing is the same as in figure 5.2.

We have divided one spin period of FO Aqr into 6 phases, and fitted each spectrum with leaky absorber model. Results are shown in figure 6.3. The phase divisions are shown in the upper left panel with vertical dotted lines. Notice that the 'dip' and the 'peak' phases are identical with the pulse-bottom and the pulse-peak phase used in the spin-phase spectral analysis in section 5.3, respectively. From this figure, it is easily understood that the energy independent modulation of the hard X-ray intensity cannot be explained by the electron scattering due to matter responsible for the photoelectric absorption, for the largest change of the normalization of the thermal bremsstrahlung due to the electron scattering is expected between the 'peak' and the 'bottom' phase since the differences of both N_H and CF are the largest between these two phases. The flux deficit in 1.2–5.2keV is, however, larger in the 'dip' phase than in the 'bottom' phase. Therefore, either P-type or IP-type modulations (see previous section) works at least around the 'dip' phase.

As the photoelectric absorption is generally stronger when we observe the emission region along the accretion column than from the side in intermediate polars, CF shown in figure 6.3 suggests that the emission region comes nearest to the limb of the white dwarf around the spin phase of 1.5–1.6. Therefore, IP-type modulation is unlikely since the 'dip' occurs near the phase of minimum CF. Alternatively, we believe that accreting mass is not evenly

distributed between two magnetic poles, and the 'dip' occurs when at least a part of the mainly accreting pole moves behind the limb of the white dwarf.

6.3.4   EX Hya

As mentioned in section 5.3.2, larger modulation amplitude in lower energy bands of EX Hya is, unlike other intermediate polars, attributed to the existence of the soft component in the pulse-peak phase. As hydrogen column density is small throughout a spin cycle, the modulation amplitude of order 10% in higher energies can not be accounted for the electron scattering associated with preshock accreting matter.

As in the case of FO Aqr, this energy-independent modulation is attributable to the self-eclipse of a single emission region from the X-ray data only. Hellier & Mason (1990) found from their phase-resolved optical spectroscopy, however, that, unlike other intermediate polars, the width (not the velocity itself) of $H\gamma$ line is modulated at the rotational period of the white dwarf in EX Hya, which indicates that mass accretion occurs onto to magnetic poles, and it is broadest in the X-ray pulse-peak phase. They conclude that the X-ray is emitted from both maginetic poles, and its intensity maximum occurs when we observe the emission regions from the side. This suggests that the energy-independent spin modulation of the hard X-ray in EX Hya is the IP-type modulation.

It is well known that hard X-ray intensity of EX Hya periodically drops at the orbital period of 98min (figure 4.3), which is interpreted as due to the eclipse of the emission region(s) by the secondary star. Characteristics of this orbital eclipse in hard X-rays are investigated by Rosen *et al.* (1991) with *EXOSAT* and *Ginga* data. They found that

(a) the hard X-ray orbital eclipse is grazing with the eclipse fraction is ∼40% above 6keV (Rosen, Mason & Cordova 1988).

(b) the eclipse deficit in the light curve is larger when the eclipse occurs at the pulse-peak spin-phase,

(c) averaged eclipse depth above 6keV is constant at about 40% and it decreases with decreasing X-ray energy.

To explain these behaviours, they thought that there are two poles separated by 180° onto which mass accretes almost evenly, and only the pole on the lower hemisphere is eclipsed by the secondary star (point (a)). Therefore, as shown in figure 6.4, the count deficit due to the orbital eclipse is larger in the pulse-peak phase since the contribution of the pole in the lower hemisphere to the X-ray flux is maximum in this phase (point (b)). In addtion, the small energy dependece of the eclipse deficit is attributed to photoelectric absorption and the scattering of the soft X-ray from the lower pole by accretion disk (point (c)).

As we have discovered the extra soft component, this model needs to be modified a little. As the soft emission component appeciable only below ∼4keV in the pulse-peak spectrum, the energy dependence of the orbital eclipse (point (c)) is probably attributed to this soft
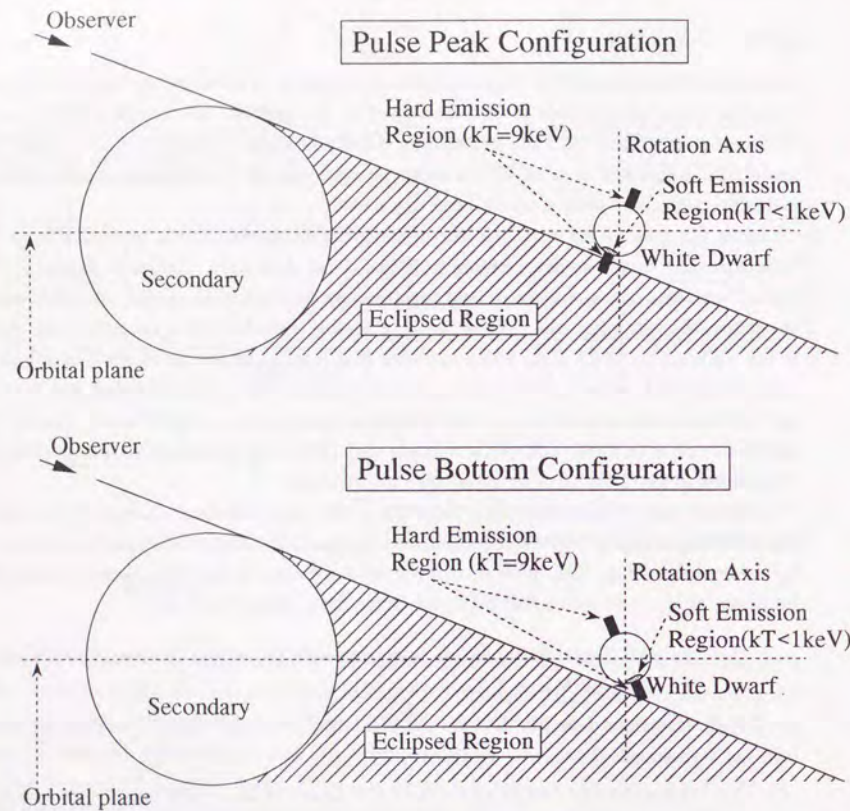
Observer

Pulse Peak Configuration

Hard Emission
Region (kT=9keV)

Rotation Axis

Soft Emission
Region(kT<1keV)

White Dwarf

Secondary

Eclipsed Region

Orbital plane

Observer

Pulse Bottom Configuration

Hard Emission
Region (kT=9keV)

Rotation Axis

Soft Emission
Region(kT<1keV)

Secondary

White Dwarf

Eclipsed Region

Orbital plane

Figure 6.4: Accretion pole geometry of EX Hya during the eclipse.

component on behalf of the accretion disk, which may be difficult to be formed in the shorter period system like EX Hya (Hameury, King & Lasota 1986). The soft component emitter is inferred to be near the accretion pole in the lower hemisphere, since the soft component is visible only during the pulse-peak phase. In order to explain the energy dependence of orbital eclipse, the soft component should not be eclipsed by the secondary. Therefore, it should locate near the surface of the white dwarf, reminiscent of the soft blackbody emitter in polar.

6.3.5   RE0751+14

Unlike other intermediate polars, RE0751+14 shows the modulation amplitude which is, like polars, almost independent of the incident X-ray energy (figure 5.3). The temperature of the emission region is significantly different between the pulse-peak and the pulse-bottom (table 5.9). The iron line intensity is also modulated with the white dwarf rotation (figure 5.22). These characteristics are common with AM Her and H0538+608 in which the self-eclipse of the emission region plays an important role on the spin modulation of the light curve. Especially, the latter two characteristics indicates that we observe different emission regions between the pulse-peak and the pulse-bottom. Therefore, we conclude that the spin modulation of the light curve in RE0751+14 is due to the eclipse of the emission region like polar.

6.4   Iron Line Emissions

6.4.1   Comparison of Line Parameters with Models

As we have pointed out in subsection 5.6.2, the iron line emission of MCVs originates both from iron ionized by collisions in the hot plasma and from iron ionized by X-ray irradiation in the cold matter surrounding the emission region. In this subsection, we compare observed line equivalent widths and the line center energies with theoretical predictions.

To begin with, we assume that the hard X-ray-emitting plasma is in collisional ionization equilibrium, and we adopt the line equivalent width calculated for hot plasma shown in figure 5.20 in our model building. When hard X-ray-irradiated cold matter surrounds the emission region with 4π solid angle (the case II in figure 5.21), the expected fluorescent line equivalent width is represented by

$$EW = \frac{N_H}{10^{21} \mathrm{cm}^{-2}} \quad \text{(eV)} \quad .$$

The accuracy of this formula is around 5% for values of N_H in the range of 10^{22} to $10^{24}\mathrm{cm}^{-2}$. If cold matter surrounds the emission region with solid angle of Ω, expected equivalent width becomes

$$EW = \frac{\Omega}{4\pi} \frac{N_H}{10^{21} \mathrm{cm}^{-2}} \quad \text{(eV)} \quad . \tag{6.8}$$

The expected line equivalent width is represented with the sum of these two. Estimation of Ω is, howeve, difficult, and the contribution of the white dwarf surface behind the continuum emission region may have also to be taken into account. For simplicity, we first neglect the contribution of the white dwarf surface to the line emission, and estimate Ω from the covering fraction obtained from the spin-phase average spectra. This is because the spin-phase average spectra is regarded as an average over observations from various directions.

We obtain a formula representing "expected" equivalent width as a sum of those of

thermal plasma origin and fluorescence origin as

$$
\begin{aligned}
EW &= EW_{th}(kT) + EW_{fl}(N_H, \Omega) \\
&= EW_{th}(kT) + \frac{\Omega}{4\pi} \frac{N_H}{10^{21}\text{cm}^{-2}} \\
&= EW_{th}(kT) + \frac{1}{2} CF \frac{N_H}{10^{21}\text{cm}^{-2}} \quad \text{(eV)} \quad .
\end{aligned}
\tag{6.9}
$$

Here we have used the relation $CF = \Omega/2\pi$. The expected line center energy is caluculated as a mean of those of thermal plasma origin and fluorescence origin weighted by the expected equivalent width.

The observed equivalent width and the line center energy are compared with those "expected" in figure 6.5. The observed equivalent widths show reasonable agreement with the them, whereas the observed line center energies are systematically below the expected values. There are two ways to resolve this discrepancy in the center energy. One possibility is to discard the assumption of collisional ionization equilibrium. In this case, the center energies of iron in the hot plasma become significantly lower than the equilibrium value of 6.8–6.9keV. Alternatively, it is also possible that CF does not give the true coverage of cold matter Ω well. For example, we have neglected the contribution to the iron line from the white dwarf surface. In the following subsections, we further examine these two possibilities.

6.4.2 Collisional Ionization Non-equilibrium

Once iron elements are placed in electrons abruptly heated up in the shock wave, electrons are stripped off from the outer shell, and iron elements gradually approaches the equilibrium ionization distribution shown in figure 5.19. The ionization state of non-equilibrium iron is determined by the parameter $n_e t$, where n_e is the number density of electron and t is the time iron atoms spend in the hot electrons (Masai 1984). Although we have derived $n_e \sim 10^{15-16}\text{cm}^{-3}$ in subsection 6.1.3, it is difficult to determine t because t strongly depends upon the height of the shock front from the white dwarf surface. Therefore, here we make the following assumption: iron spends relatively long time in the state of Fe^{+24} (helium-like). This assumption is quite natural since electrons form a closed shell and there is a large gap between the binding energy of K-shell (~ 8.8keV; see figure 5.19) and L-shell ($\sim$1keV). This means the hydrogen-like irons known to exist in the equilibrium are assumed to be in the helium-like state. The emissivity of the K_α line emission from non-equilibrium helium-like iron is approximately twice as large as that of hydrogen-like iron in equilibrium at a given temperature (Masai 1984). We can then estimate the line equivalent width for emission from plasma in collisional ionization non-equilibrium. The expected line center energy is again caluculated as the mean weighted by equivalent widths of that of plasma origin and that of fluorescence origin.

The observed line equivalent width and center energy are compared with those estimated with the method above in figure 6.6. The observed line center energies are now in good agreement with those expected compared with figure 6.5. The observed equivalent widths,

on the other hand, are substantially smaller than those expected from gass with solar abundances. However, this may be attributed to the abundance deficit. In the case of collisional ionization non-equilibrium, abundance of iron should be in the range of 0.5–1.0.

However, collisional ionization non-equilibrium raises a serious problem related with the shape of the emission region. Masai (1984) have pointed out that the collisional ionization equilibrium is attained almost irrespective of the plasma temperature if the following relation is satisfied.

$$
n_e t \geq 10^{12} \quad (\text{cm}^{-3}\text{s}),
\tag{6.10}
$$

where n_e means the electron number density and t represents the time spent by iron, which is at first neutral, in the hot plasma. As we have derived the density of the emission region to be of order 10^{15-16} cm^{-3}, this relation poses an upper limit on the height of the emission region. Assuming accretion with free fall velocity, we obtain the post shock velocity of the flow as

$$
\begin{aligned}
v &= \frac{1}{4}\sqrt{\frac{2GM}{R}} \\
&= 1.7 \times 10^8 \left(\frac{M}{M_\odot}\right)^{1/2} \left(\frac{R}{5.5 \times 10^8}\right)^{-1/2} \quad (\text{cm s}^{-1}).
\end{aligned}
\tag{6.11}
$$

From this equation, we obtain the height of the emission region as

$$
\begin{aligned}
h &= vt \\
&\leq v\left(\frac{10^{12}}{n_e}\right) \\
&= 1.7 \times 10^4 \left(\frac{M}{M_\odot}\right)^{1/2} \left(\frac{R}{5.5 \times 10^8}\right)^{-1/2} \left(\frac{n_e}{10^{16}}\right)^{-1} \quad (\text{cm}).
\end{aligned}
\tag{6.12}
$$

Therefore, the height of the emission region is of order 10^{-5} of the white dwarf radius. With this height, the iron column density becomes only of order 10^{20} cm^{-2}, and it is difficult to generate the observed K-edge absorption corresponding to highly-ionized iron atoms. The area A of the white dwarf over which mass accretion occurs poses a much more serious problem.

$$
\begin{aligned}
A &= \frac{E.M.}{n_e^2 h} \\
&\geq 5.8 \times 10^{18} \left(\frac{E.M.}{10^{55}}\right) \left(\frac{n_e}{10^{16}}\right)^{-1} \left(\frac{M}{M_\odot}\right)^{-1/2} \left(\frac{R}{5.5 \times 10^8}\right)^{1/2} \quad (\text{cm}^2).
\end{aligned}
\tag{6.13}
$$

Then so-called fractional area, which is defined as

$$
f = \frac{A}{4\pi R^2},
\tag{6.14}
$$

becomes more than 1.5 for a white dwarf of $1M_\odot$. We conclude that collisional ionization non-equilibrium is unlikely.
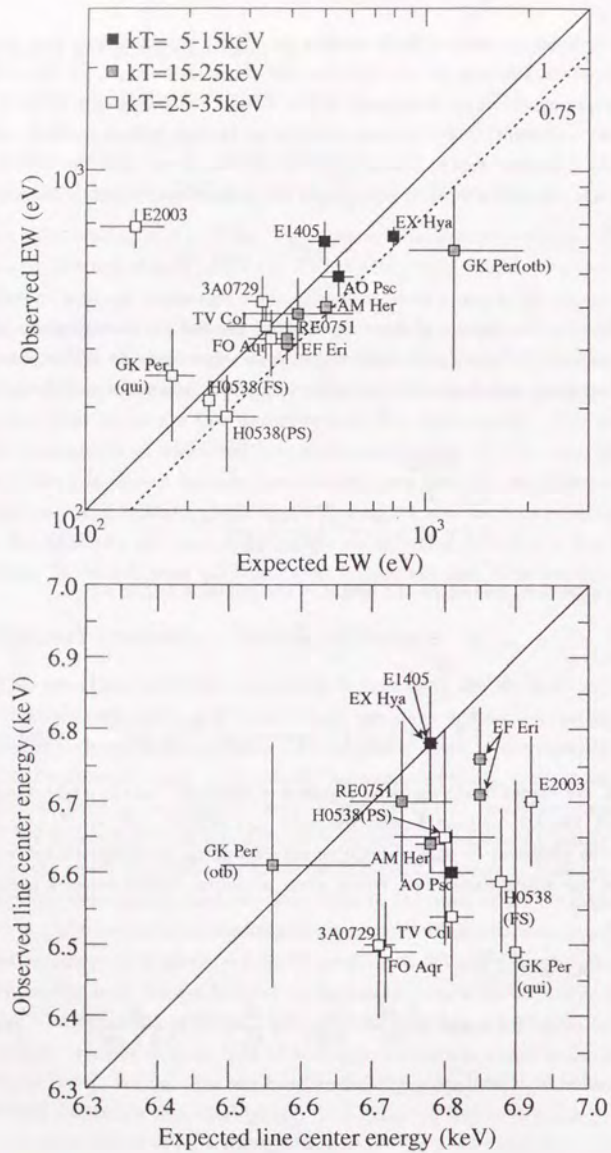
Figure 6.5: Comparison of the expected line equivalent width and center energy with those expected from kT, N_H, and Ω.
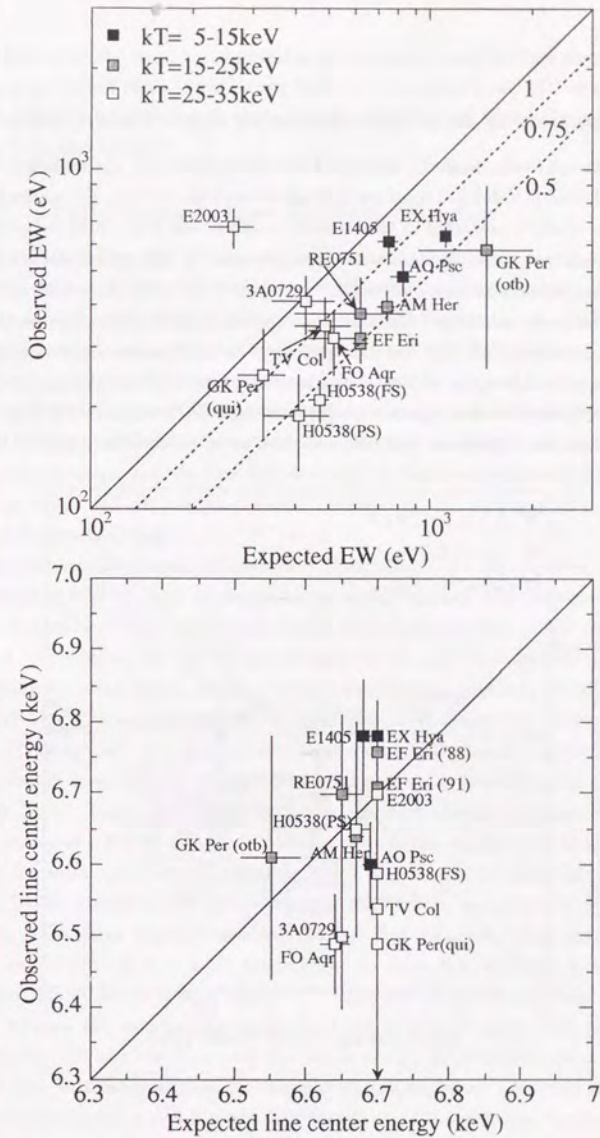
Figure 6.6: Observed line equivalent widths and center energies compared with those expected from fluorescence and plasma in collisional ionization non-equilibrium.

6.4.3   Contribution to Iron Line Emission from Cold Matter

It is also possible that the solid angle Ω subtended by cold matter over the emission region cannot be estimated with CF derived from the spin-phase average spectra. For example, the white dwarf surface, which is neglected in the analysis in subsection 6.4.1, may substantially contribute to the observed iron line emission. Here we assume the collisional ionization equilibrium in the hot plasma and adopt the line equivalent width and the center energy in equilibrium value. We have caluculated the expected equivalent width of the fluorescent iron line emission under the condition that the expected line center energies, which is obtained by the mean of the center energies of the line of plasma origin and of fluorescence origin weighted by their equivalent widths, agree with those observed. The results are depicted in figure 6.7. In this case, the abundance deficit of iron scatters in much wider range of 0.2–1.0
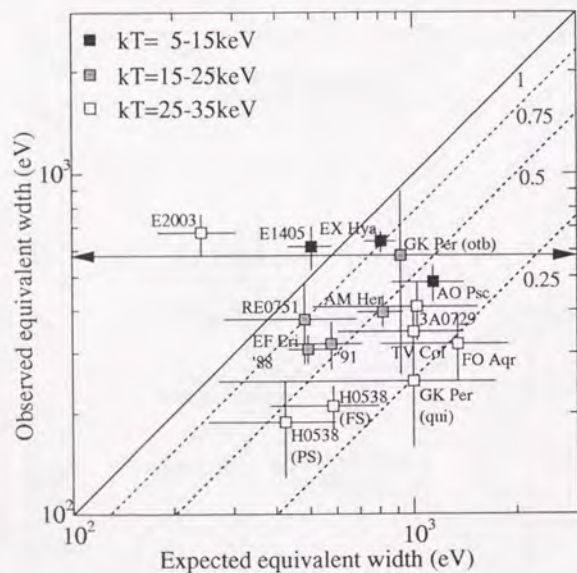
Figure 6.7: Observed equivalent width compared with those expected from plasma in collisional ionization equilibrium and cold matter surrounding the emission region.

compared with in the collisional ionization non-equilibrium case.

A problem inherent in this picuture is, however, that a continuum component due to

the reflection of the hard X-ray emission by the white dwarf surface should be visible in the observed spectra if there is such a big deficit in iron abundance. We therefore conclude that the contribution of cold matter to the iron emission line via fluorescence more than expected from CF is also unlikely.

6.4.4   Multi-temperature Emission Region

In the discussions so far, we have assumed that the hot plasma in the postshock region is uniform. Although all the spectra of MCVs can be fitted with the thermal bremsstrahlung model spectrum with a single temperature, we have found that the temperature varies significantly with the spin phase of the white dwarf in AM Her (section 5.5). Therefore, it is possible that the plasma temperature obtained by the spectral fitting with the single temperature thermal bremsstrahlung represents an average over the multi-temperature emission region. If so, as shown in figure 5.19, the iron line is emitted mainly from a region with lower temperature, and the line center energy becomes substantially lower than the value expected from the plasma temperature obtained by the fitting with a single temperature thermal bremsstrahlung.

To examine this possibility, we have attempted to fit the observed spin-phase average spectra with two thermal bremsstrahlung model spectra with different temperatures. In doing this, we deal only with Group-1 sources since the spectral model adequate for Group-2 sources (leaky absorber model) are already so complex that further detailed modeling of them may be meaningless. If we introduce two thermal bremsstrahlung components in the spectral fitting, the temperatures of these two components may not be constrained very well. Therefore, we adopt as a lower temperature component a spectral model describing the emission from plasma composed of matter of solar abundance in thermal equilibrium (Masai 1984). This model includes thermal bremsstrahlung continuum plus line emissions from matter of solar abundance in collisional ionization equilibrium at a given temperature. For higher temperature component, we adopt the thermal bremsstrahlung model spectrum. Photoelectric absorption is taken into account for both components. Note that we do not include a Gaussian line representing the iron line emission. The results of the fits with this two component model are summarized in table 6.4, and two examples are depicted in figure 6.8.   As seen from figure 6.8, behaviour of the fit residuals is qualitatively the same between the two spectra especially below 10keV. It seems that the observed spectra require the iron line emission with the center energy substantially lower than that obtained by the best fit temperature of the thermal plasma emission. This may suggest that the two temperature model is still a rough approximation of the observed spectra.

The fits are, however, acceptable on the average, and the line center energy discrepancy is probably resolved by introducing multi-temperature emission region. This result suggests that the multi-temperature is a common feature of the hard X-ray emission region among MCVs.

Table 6.4: Results of the spectral fitting with the thermal plasma emission and the thermal bremsstrahlung for Group-1 sources.

Source	Thermal plasma emission		Thermal bremsstrahlung			
	Norm.[a]	Temp.[b]	Norm.[a]	Temp.[b]	$\log N_H$ [c]	χ_ν^2 (d.o.f.)
EF Eri ('88)	0.20 ± 0.02	7.6 ± 1.5	0.72 ± 0.06	28.8 ± 4.2	21.8 ± 0.1	1.00 (32)
EF Eri ('91)	0.16 ± 0.02	10.6 ± 2.5	0.49 ± 0.05	23.9 ± 5.4	21.6 ± 0.1	1.16 (32)
H0538+608 (FS)	0.09 ± 0.02	7.5 ± 2.8	0.61 ± 0.05	38.9 ± 6.4	21.9 ± 0.1	1.79 (26)
E2003+225	0.06 ± 0.02	5.6 ± 5.0	0.67 ± 0.47	>40	23.0 ± 0.2	0.86 (21)
GK Per (Qui.)	0.05 ± 0.02	7.3 ± 5.3	0.30 ± 0.05	>27	22.1 ± 0.2	0.92 (29)
3A0729+103	0.12 ± 0.07	3.8 ± 1.8	0.34 ± 0.05	>28	23.2 ± 0.1	1.64 (32)

a: Normalization in unit of 10^{-2} photons s^{-1} cm^{-2} keV^{-1}.

b: Plasma temperature in unit of keV.

c: Hydrogen column density in unit of cm^{-2}.
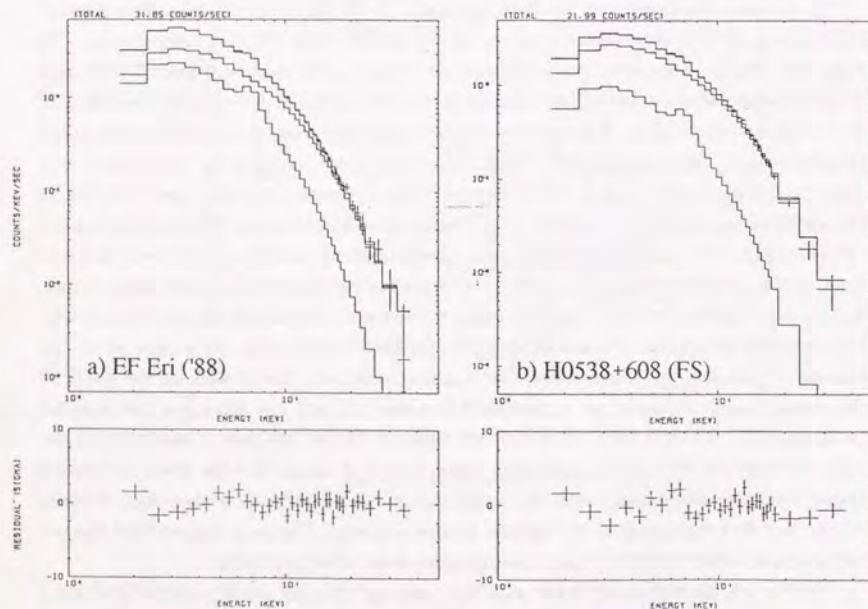
Figure 6.8: Results of the spectral fitting with the thermal plasma emission and the thermal bremsstrahlung for (a) EF Eri ('88) (χ_ν^2=1.00) and (b) H0538+608 in FS (χ_ν^2=1.79).

Chapter 7

Conclusions and Future Prospects

7.1   Conclusions

1. The hard X-ray emission of all the 13 MCVs observed with *Ginga* can be interpreted as that from optically thin hot plasma with temperature of 10–40keV. This result confirms the optically thin thermal emission of MCVs proposed by the *HEAO*-A2, and A4 observations of AM Her (Rothschild *et al.* 1981) and EF Eri (White 1981) with much larger number of samples. The hot plasma is formed probably by the standing shock wave above the white dwarf surface, in which the free fall energy of supersonic accretion flow is converted into thermal energy.

2. Since plasma temperatures reflect the depth of the gravitational potential of the white dwarf, we have derived lower limits of the white dwarf masses to be $0.3 - 0.7 M_\odot$ with the aid of the mass-radius relation of the white dwarf. The masses thus obtained are consistent with those derived by Mukai & Charles (1987).

3. We have obtained the hydrogen number density in the hard X-ray emission region to be 10^{15-16}cm^{-3} with the depth of K-edge absorption of highly ionized iron and with the emission measure.

4. We have found that the spectra of all the MCVs in 1.2–37.4keV range are completely explained by optically thin thermal bremsstrahlung model spectrum with photoelectric absorption represented by at most two different hydrogen column densities, plus narrow iron line emission. It has already been revealed by *EXOSAT* observations that the photoelectric absorption of a large number of intermediate polars can never be represented with a single hydrogen column density (Norton & Watson 1989). *Ginga* observations have revealed that this is also the case for polars.

5. The spin modulation of hard X-ray intensity of polars is caused by the eclispe of the emission region by the white dwarf. Since *Ginga* observations of polars have revealed that the photoelectric absorption is stronger in the pulse-peak phases, we believe that

the photoelectric absorption occurs in the accretion column, and the optical depth of it is larger along the accretion column.

We have found that the photoelectric absorption of intermediate polars is, on the other hand, stronger in the pulse-bottom phases. If the optical depth of the photoelectric absorption is larger along the accretion column also in intermediate polars, the accreting pole points to the observer in the pulse-bottom phases. This picture is probably reasonable since the mass from the secondary accretes onto two magnetic poles separated by an angle of $\sim 180°$ almost evenly because of asynchronism between the orbital revolution and the rotation of the white dwarf. In this case, the eclipse of the emission regions by the white dwarf is not effective for the spin modulation of the hard X-ray intensity since the two emission regions alternatively come into view of the observer. Alternatively, variation of the amount of the photoelectric absorption with the rotation of the white dwarf mainly cause the modulation of the hard X-ray intensity.

6. Strong iron K_α emission lines are observed from all the MCVs observed with *Ginga*, which confirms the *EXOSAT* observations of intermediate polars (Norton & Watson 1989). The LAC, however, enables us to investigate the iron line emission from MCVs qualitatively for the first time. We have found that the iron line emission of MCVs originates both from postshock hot plasma in collisional ionization equilibrium and from cold matter surrounding the emission region irradiated by the X-ray via fluorescence. The observed line center energies are, however, significantly lower than those calculated by a weighted mean of these two components with a mixture predicted by the theoretical models. Although continuum spectra of MCVs are explained by the optically thin thermal bremsstrahlung spectrum with a single temperature, this result strongly suggests that the hard X-ray emission region is not uniform, and a part with relatively lower temperature makes greater contribution to the observed iron line emissions.

7. We have discovered a significant temperature gradient in the hard X-ray emission region of AM Her. This result, together with the result of the iron line center energy mentioned above, indicates that the emission region of MCVs is generally inhomogeneous, as has been pointed out by a number of theoretical predictions. Further analysis of the current *Ginga* data probably provides us with a unique chance to evaluate the theoretical models so far presented (Lamb 1985 and references therein) quantitatively.

7.2 Future Prospects

7.2.1 Temperature Gradient in AM Her

As described in section 5.5 and subsection 6.3.2, we have found that there is the temperature inhomogeneity in the single emission region of AM Her. It is highly important to determine the direction of this temperature gradient; either along the accretion column or along the white dwarf surface. We expect that the depth of the K-edge absorption due to highly ionized iron can be utilized for this purpose. As described in section 5.4, this absorption is caused by the iron in the postshock hot plasma. Therefore, the length of the emission region along the line of sight at a given spin phase of the white dwarf is estimated by the column density of the highly ionized iron.

If the temperature gradient in the emission region of AM Her is found to be along the accretion column through the analysis, the observed spectra of AM Her provides us with a unique chance to examine a number of theoretical models on the hard X-ray emission region. For example, we show expected energy spectrum of the hard X-ray emission from the postshock region calculated by Aizu (1973) in figure 7.1, together with a single temperature thermal bremsstrahlung spectrum. It is easily be noted that they resemble each other, and may not be discriminated if the column density of the photoelectric absorber is adjusted appropriately. Although we have so far fitted the observed spectra of MCVs with a single temperature thermal bremsstrahlung, the Aizu spectrum may also give acceptable fits.

7.2.2 Iron Line Measurements with ASTRO-D

As described in subsection 6.4.4, both the observed equivalent widths and the center energies of the iron line are probably explained by introducing the hard X-ray emission region with multi-temperature. To establish this picture, it is necessary to measure the shape of the iron emission lines. As shown in figure 5.21, the line center energy varies with the plasma temperature. Therefore, the distribution of the temperatures and the emission measures in the emission region will be evaluated by measuring the shape of the line. It is difficult to measure the shape of the iron line with the LAC because of poor energy resolution (18% at 6keV). It will, however, be possible with the SIS (Solid-state Imaging Spectrometer) on board the ASTRO-D satellite which will be launched in 1993. The energy resolution of the SIS is $\sim 2\%$ at 6keV.
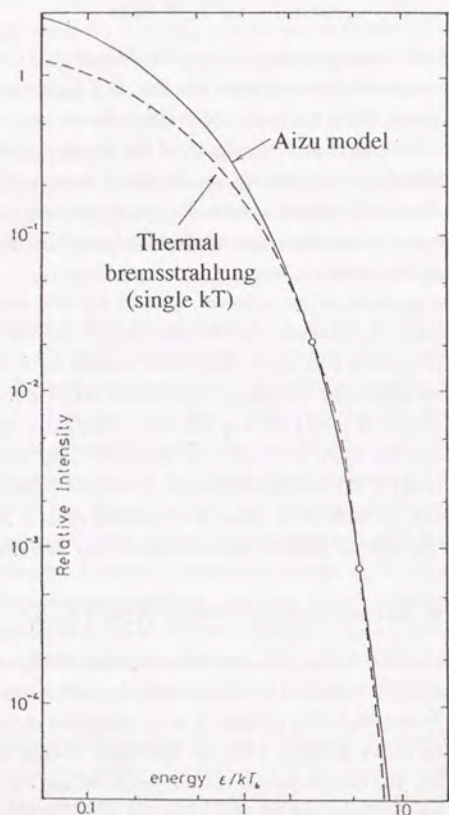
Figure 7.1: Energy spectrum expected from the emission region calculated by Aizu (1973) together with a single temperature thermal bremsstrahlung.

Appendix A

Notes on the Period Determination

In this chapter, we briefly summarize the precision of the period determination and possibilities of the detection of spurious periodicities with the *Ginga* data. When we observe a source which shows intensity modulation at period P_S during a time span of T, the number of pulse included in the observation is

$$n = \frac{T}{P_S}. \tag{A.1}$$

Therefore the precision of the period determination is formally denoted as

$$\frac{\Delta P}{P_S} = \frac{\Delta n}{n} = \frac{P_S}{T} \Delta n, \tag{A.2}$$

where Δn is the error of phase determination. The value of Δn depends on the source intensity, depth of modulation, pulse profile and its stablity *etc.* Empirically, $\Delta n \sim 0.2$ is a reasonable estimate for a few days *Ginga* observation of a source with an intensity of a few mC. The above formula is thus evaluated as

$$\frac{\Delta P}{P_S} = 0.02 \left(\frac{P_S}{10^4 \mathrm{s}}\right) \left(\frac{T}{1 \mathrm{day}}\right)^{-1} \qquad \text{for polars,} \tag{A.3}$$

$$= 0.002 \left(\frac{P_S}{10^3 \mathrm{s}}\right) \left(\frac{T}{1 \mathrm{day}}\right)^{-1} \qquad \text{for intermediate polars.} \tag{A.4}$$

The observed flux $F(t)$ can sometimes be represented as the intrinsic source intensity $I(P_S, t)$ multiplied by a kind of window function with another period, P, such as

$$F(t) = h(P, t) I(P_S, t), \tag{A.5}$$

where $h(P, t)$ means the window function, which causes spurious periodicities. Defining $\Omega = 2\pi/P$ and $\Omega_S = 2\pi/P_S$, $F(t)$ shows beat periodicities at $P' = 2\pi/\Omega' = 2\pi/(m\Omega_S + n\Omega)$ $(m, n = \pm 1, \pm 2, \cdots, \Omega' > 0)$ as well as at nP and nP_S $(n = 1, 2, \cdots)$.

There are two origins of periodic window function, $h(P, t)$. One is related to the way of *Ginga* observation, which is interrupted recurrently by the passage of the satellite through high background regions at the orbital period of *Ginga*, $P = 96$min (chapter 3). The difference between P_S and its nearest neighbor is

$$\Delta P = \frac{2\pi}{\Omega_S} - \frac{2\pi}{\Omega_S + \Omega}.$$

127

Therefore,

$$\frac{\Delta P}{P_S} = 1 - \frac{\Omega_S}{\Omega_S + \Omega} \sim 0.5, \qquad (A.6)$$

where $\Omega_S \sim \Omega$ for most MCVs. Comparing this with eq(A.3) and (A.4), the beat period related with the *Ginga* sampling is easily distinguished from the true period. In addition to the beat periodicity, it sometimes occurs for polars that P_S becomes very similar to nP. For example, $\Delta P/P_S = |P_S - 2P|/P_S = 0.06$ and 0.04 for AM Her ($P_S=3.09$h) and H0538+608 ($P_S=3.33$h), respectively ($n=2$), which are of the same order of magnitude as the accuracy of period determination (eq(A.3)).

The other origin of periodic window function is the orbital motion of intermediate polars. Intermediate polars typically have $P_S \sim 10^3$s and $P = P_{orb} \sim 10^4$s. With these estimates,

$$\Delta P = \frac{2\pi}{\Omega_S} - \frac{2\pi}{\Omega_S + \Omega} \simeq \frac{2\pi}{\Omega_S}\frac{\Omega}{\Omega_S}.$$

Hence,

$$\frac{\Delta P}{P_S} = \frac{\Omega}{\Omega_S} \simeq 0.1. \qquad (A.7)$$

Therefore, these period aliases can be discriminated out, too.

Finally, let us check the Doppler effects of the orbital motion of the white dwarf, and the earth. The orbital velocity of the white dwarf, v is estimated with Kepler's third law, and the mass of the components as

$$v = 8.7 \times 10^6 \left(\frac{P_{orb}}{10^4 \text{s}}\right)^{-1/3}\left(\frac{M_2}{0.2 M_\odot}\right)\left(\frac{M_1 + M_2}{M_\odot}\right)^{-2/3} \qquad \text{cm s}^{-1}$$

(as for the estimates of component masses, see chapter 2). From this equation,

$$\frac{\Delta P}{P_S} \sim \frac{v_{WD}}{c} \sim 10^{-4}, \qquad (A.8)$$

which is of the same order as that expected from the revolution of the earth. Therefore, the Doppler effect of the orbital motion of the white dwarf and the earth is negligibly small compared with the precision of the present period determination.

Acknowledgment

References

Aizu, K., 1973, *Prog. Theoret. Phys.*, **49**, 1184.

Barrett, P. E. & Chanmugam, G., 1985, *Astrophys. J.*, **298**, 743.

Berriman, G., 1987, *Astron & Astrophys. Suppl.*, **68**, 41.

Berriman, G., Szcody, P. & Capps, R. W., 1985, *Mon. Not. Roy. Astr. Soc.*, **217**, 327.

Beuermann, K. & Stella, L., 1985, *Sp. Sci. Rev.*, **40**, 139.

Beuermann, K., Thomas, H. -C., Giommi, P & Tagliaferri, G., 1986, *IAU Circ.*, No. 4289.

Beuermann, K., Thomas, H. -C., Giommi, P & Tagliaferri, G., 1988a, *IAU Circ.*, No. 4671.

Beuermann, K., Thomas, H. -C. & Schwope, A., 1988b, *Astron & Astrophys.*, **195**, L15.

Beuermann, K., Thomas, H. -C. & Schwope, A., 1989, *IAU Circ.*, 4775.

Biermann, P., Kühr, H., Liebert, J., Stockman, H. S., Strittmatter, P. A. & Tapia, S, 1982, *IAU Circ.*, No.3680.

Biermann, P., Schmidt, G. D., Liebert, J., Stockman, H. S., Tapia, S., Kühr, H., Strittmatter, P. A., West, S. & Lamb, D. Q., 1985, *Astrophys. J.*, **293**, 303.

Bonnet-Bidaud, J. M., Mouchet, M. & Motch, C., 1982, In *Proc. of the third IUE conference, Madrid, Spain*, ed. Rolfe, E., Heck, A. & Battrick, B., ESA SP-176, 241.

Bonnet-Bidaud, J. M., Motch, C. & Mouchet, M., 1985, *Astron & Astrophys.*, **143**, 313.

Bradt, H. V., Remillard, R. A., Tuohy, I. R., Buckley, D. A. H., Brissenden, R., Schwartz, D. A. & Roberts, W., 1988, *Proc. of the symposium on the Physics of Neutron Star and Black Holes*, Tokyo, ed.Tanaka, Y., Universal Academic Press Inc., Tokyo.

Buckley, D. A. H. & Tuohy, I. R., 1987, *Proc. Astron. Soc. Australia*, **7**, 2.

Chanmugam, G., & Dulk, G. A., 1981, *Astrophys. J.*, **244**, 569.

Crampton, D., Cowley, A. P. & Hutchings, J. B., 1983, In *Cataclysmic Variables & Related Objects*, ed. Livio, M. & Shaviv, G., Reidel, IAU Colloq. No.72, 25.

Crosa, L., Szcody, P., Stokes, G., Swank, J. & Wallerstein, G., 1981, *Astrophys. J.*, **247**, 984.

Cropper, M., 1982, *Inf. Bull. Var. Stars.*, 2096.

Cropper, M., 1988, *Mon. Not. Roy. Astr. Soc.*, **231**, 597.

Cropper, M., 1990, *Sp. Sci. Rev.*.

Cropper, M., Mason, K. O., Allington-Smith, J. R., Branduardi-Raymont, G., Charles, P. A., Mittaz, J. P. D., Mukai, K, Murdin, P. G. & Smale, A. P., 1989, *Mon. Not. Roy. Astr. Soc.*, **236**, p29.

Cropper, M., Mason, K. O. & Mukai, K., 1990, *Mon. Not. Roy. Astr. Soc.*, **243**, 565.

Duerbeck, H. W., 1981, *Publ. Astr. Soc. Pac.*, **93**, 165.

Fabbiano, G., Hartmann, L., Raymond, J., Steiner, J., Branduardi-Raymont, G. & Matilsky, T., 1981, *Astrophys. J.*, **243**, 911.

Fabian, A. C., Pringle, J. E. & Rees, M. J., 1976, *Mon. Not. Roy. Astr. Soc.*, **175**, 43.

Feigelson, E., Dexter, L. & Liller, W., 1978, *Astrophys. J.*, **222**, 263.

Ferrario, L., Wickramasinghe, D. T., Bailey, J. A., Tuohy, I. R. & Hough, J. H., 1989, *Astrophys. J.*, **337**, 832.

Frank, J., King, A. R. & Lasota, J. P., 1983, *Mon. Not. Roy. Astr. Soc.*, **202**, 183.

Frank, J., King, A. R. & Raine, D. J., 1985, *Accretion Power in Astrophysics*, Cambridge University Press.

Giommi, P., Angelini, L., Osborne, J. P., Stella, L. & Tagliaferri, G., 1987, *IAU Circ.*, No.4486.

Gilliland, R. L., 1982, *Astrophys. J.*, **258**, 576.

Gould, R. J., 1980, *Astrophys. J.*, **238**, 1026.

Griffis, R. E., Ward, M. J., Blades, J. C., Wilson, A. S., Chaisson, L. & Johnston, M. D., 1979, *Astrophys. J.*, **232**, L27.

Hassall, B. J. M., Pringle, J. E., Ward, M. J., Whelan, J. A. J., Mayo, S. K., Echevarria, J., Jones, D. H. P., Wallis, R. E., Allen, D. A. & Hyland, A. R., 1981, *Mon. Not. Roy. Astr. Soc.*, **197**, 275.

Hayashida, K. *et al.*, 1989, *Publ. Astr. Soc. Japan*, **41**, 373.

Heise, J., Kruszewski, A., Chlebowski, T., Mewe, R., Kahn, S. & Seward, F. D., 1984, *Phys. Scrip.*, **T7**, 115.

Hellier, C., Mason, K. O., Rosen, S. R. & Córdova, F. A., 1989, *Mon. Not. Roy. Astr. Soc.*, **228**, 463.

Hellier, C., Mason, K. O. & Cropper, M. S., 1990, *Mon. Not. Roy. Astr. Soc.*, **242**, 250.

Hellier, C. & Mason, K. O., 1990, in *Accretion-Powered Compact Binaries*, ed. Mauche, C. W., Cambridge University Press, p185.

Hellier, C., Cropper, M. S. & Mason, K. O., 1991, *Mon. Not. Roy. Astr. Soc.*, **248**, 233.

Hoshi, R., 1973, *Prog. Theoret. Phys.*, **49**, 776.

Hutchings, J. B., 1987, *Pub. Astr. Soc. Pac.*, **99**, 57.

Hutchings, J. B., Crampton, D., Cowley, A. P., Thorstensen, J. R. & Charles. P. A., 1981, *Astrophys. J.*, **249**, 680.

Imamura, J. N. & Durisen, R. H., 1983, *Astrophys. J.*, **268**, 291.

Imamura, J. N., Durisen, R. H., Lamb, D. Q. & Weast, G. J., 1987, *Astrophys. J.*, **313**, 298.

Inoue, H., 1985, *Sp. Sci. Rev.*, **40**, 317.

Ishida, M., Silber, A., Bradt, H. V., Remillard, R. A., Makishima, K. & Ohashi, T., 1991a, *Astrophys. J.*, **367**, 270.

Ishida, M., Sakao, T., Makishima, K., Ohashi, T., Watson, M. G., Norton, A. J., Kawada, N., & Koyama, K., 1991b, *Mon. Not. Roy. Astr. Soc., in press*.

Kallman, T. R. & McCray, R., 1982, *Astrophys. J. Suppl.*, **50**, 263.

King, A. R. & Lasota, 1980, *Mon. Not. Roy. Astr. Soc.*, **191**, 721.

King, A. R. & Shaviv, G., 1984, *Mon. Not. Roy. Astr. Soc.*, **211**, 883.

Krolik, J. H. & Kallman, T. R., 1984, *Astrophys. J.*, **286**, 366.

Krzeminski, W. & Serkowski, K., 1977, *Astrophys. J.*, **216**, L45.

Kuijpers, J. & Pringle, J. E., 1982, *Astron & Astrophys.*, **114**, L4.

Lamb, D. Q., 1985, In *Cataclysmic Variables and Low-Mass X-ray Binraries*, ed. Lamb, D. Q. & Patterson, J., Reidel, p179.

Lamb, D. Q. & Masters, A. R., 1979, *Astrophys. J.*, **234**, L117.

Lance, C. M., McCall, M. L. & Uomoto, A. K., 1988, *Astrophys. J. Suppl.*, **66**, 151.

Latham, D. W., Liebert, J. & Steiner, J. E., 1981, *Astrophys. J.*, **246**, 919.

Liebert, J. & Stockman, H. S., 1985, In *Cataclysmic Variables and Low-Mass X-ray Binraries*, ed. Lamb, D. Q. & Patterson, J., Reidel, p151.

Makishima, K., 1986, in *Lecture Notes in Physics*, Vol.**266**, *The Physics of Accretion onto Compact Objects*, ed. Mason, K. O., Watson, M. G. & White, N. E., Springer-Verlag, p249.

Makino, F & the ASTRO-C team, 1987, *Astrophys. Let. Com.*, **25**, 223.

Mason, K. O., 1985, *Sp. Sci. Rev.*, **40**, 99.

Mason, K. O., Middleditch, J., Córdova, F. A., Jensen, K. A., Reichert, G., Murdin, P. G. & Clarke, D., 1982, *IAU Circ.*, No.3684.

Mason, P. A., Liebert, J. & Schmidt, G. D., 1989, *Astrophys. J.*, **346**, 941.

Masai, K., 1984, *Astrophys. Sp. Sci.*, **98**, 367.

Masai, K., 1991, *private communication*.

Masters, A. R., 1978, Ph.D. thesis, University of Illinois.

McCardy, I. M., Pye, J. P., Fairall, A. P., Warner, B., Cropper, M. & Allen, S., 1984, *Mon. Not. Roy. Astr. Soc.*, **210**, 663.

McCardy, I. M., Pye, J. P., Fairall, A. P. & Menzies, J. W., 1987, *Mon. Not. Roy. Astr. Soc.*, **225**, 335.

Meggitt, S. M. A. & Wickramasinghe, D. T., 1989, *Mon. Not. Roy. Astr. Soc.*, **236**, 31.

Morrison, R. M. & McCammon, D., 1983, *Astrophys. J.*, **270**, 119.

Mukai, K. & Charles, P. A., 1986, *Mon. Not. Roy. Astr. Soc.*, **222**, 1p.

Mukai, K. & Charles, P. A., 1987, *Mon. Not. Roy. Astr. Soc.*, **226**, 209.

Mukai, K., Charles, P. A. & Smale, A. P., 1988, *Astron & Astrophys.*, **194**, 153.

Morris, S. L., Schmidt, G. D., Liebert, J., Stocke, J., Gioia, I. & Maccacaro, T., 1987, *Astrophys. J.*, **314**, 641.

Mumford, G. S., 1976, *Inf. Bull. Var. Stars*, 1133.

Nousek, J., Luppino, G., Gajar, S., Bond, H. E., Grauer, A. D., Schmidt, G. D., Hill, G. J. & Tapia, S., 1982, *IAU Circ.*, No.3733.

Norton, A. J. & Watson, M. G., 1989, *Mon. Not. Roy. Astr. Soc.*, **237**, 853.

Norton, A. J., Watson, M. G., King, A. R., McHardy, I. M. & Letho, H., 1990, In *Accretion-Powered Compact Binaries*, ed. Mauche, C. W., Cambridge University Press, p209.

Norton, A. J., Watson, M. G., King, A. R., Letho, H. J. & McHardy, I. M., 1991, *Mon. Not. Roy. Astr. Soc., in press*.

Okumura, Y., Tsunemi, H., Yamashita, K., Matsuoka, M., Koyama, K., Hayakawa, S., Masai, K. & Hughes, J., 1988, *Publ. Astr. Soc. Japan*, **40**, 639.

Osborne, J. P., Beuermann, K., Rosen, S. R. & Mason, K. O., 1985, *Sp. Sci. Rev.*, **40**, 143.

Osborne, J. P., Bonnet-Bidaud, J. -M., Bowyer, S., Charles, P. A., Chiapetti, L., Clarke, J. T., Henry, J. P., Hill, G. J., Kahn, S., Maraschi, L., Mukai, K., Treves, A. & Vrtilek, S., 1986, *Mon. Not. Roy. Astr. Soc.*, **221**, 823.

Osborne, J. P., Beuermann, K., Charles, P. A., Maraschi, L., Mukai, K. & Treves, A., 1987, *Astrophys. J.*, **315**, L123.

Osborne, J. P. & Mukai, K., 1988, *IAU Circ.*, 4657.

Patterson, J., 1979, *Astrophys. J.*, **231**, 789.

Patterson, J., 1979, *Astrophys. J.*, **233**, L13.

Patterson, J., 1979, *Astrophys. J.*, **234**, 978.

Patterson, J., Williams, G. & Hiltner, W. A., 1981, *Astrophys. J.*, **245**, 618.

Patterson, J., 1984, *Astrophys. J. Suppl.*, **54**, 443.

Patterson, J. & Price, C., 1980, *IAU Circ.*, 3511.

Patterson, J. & Steiner, J. E., 1983, *Astrophys. J.*, **264**, L61.

Payne-Gaposhkin, C., 1969, *Astrophys. J.*, **158**, 429.

Penning, W. R., Schmidt, G. D. & Liebert, J., 1986, *Astrophys. J.*, **301**, 885.

Ritter,H. 1990, *Astron & Astrophys. Suppl.* **85**, 1179.

Rosen, S. R., Mason, K. O. & Córdova, F. A., 1988, *Mon. Not. Roy. Astr. Soc.*, **231**, 549.

Rosen, S. R., Mason, K. O., Mukai, K. & Williams, O. R., 1991, *Mon. Not. Roy. Astr. Soc.*, **249**, 417.

Rothschild, R. E., Gruber, D. E., Knight, F. K., Matteson, J. L., Nolan, P. L., Swank, J. H., Holt, S. S., Serlemitsos, P. J., Mason, K. O. & Tuohy, I. R., 1981, *Astrophys. J.*, **250**, 723.

Schmidt, G. D., Stockman, H. S. & Grandi, S. A., 1983, *Astrophys. J.*, **271**, 735.

Schmidt, G. D., Stockman, H. S. & Margon, B., 1981, *Astrophys. J.*, **243**, L157.

Shafter, A. W. & Targon, D. M., 1982, *Astron. J.*, **87**, 655.

Shafter, A. W., Szcody, P. & Thorstensen, J. R., 1986, *Astrophys. J.*, **308**, 765.

Sherrington, M. R., Lawson, P. A., King, A. R. & Jameson, R. F., 1980, *Mon. Not. Roy. Astr. Soc.*, **191**, 185.

Shrijver, J., Brinkman, A. C. & van der Woerd, H., 1987, *Astrophys. & Sp. Sci.*, **130**, 261.

Singh, K. P., Agrawall, P. C. & Riegler, G. R., 1984, *Mon. Not. Roy. Astr. Soc.*, **208**, 679.

Silber, A., Bradt, H. V., Remillard, R. A., Ishida, M. & Ohashi, T., 1990, In *Accretion-Powered Compact Binaries*, ed. Mauche, C. W., Cambridge University Press., p289.

Stockman, H. S., Liebert. J., Tapia, S., Green, R. F., Williams, R. E., Ferguson, D. H. & Szcody, P., 1981, *IAU Circ.*, 3616.

Stockman, H. S., Foltz, C. B., Tapia, S., Schmidt, G. D. & Grandi, S. 1982, *IAU Circ.*, 3696.

Tapia, S., 1976, *IAU Circ.*, No.2987.

Tapia, S., 1977, *IAU Circ.*, No.3054.

Tapia, S., 1977, *Astrophys. J.*, **212**, L125.

Tapia, S., 1979, *IAU Circ.*, No.3327.

Tsunemi, H., Yamashita, K., Masai, K., Hayakawa, S. & Koyama, K., 1986, *Astrophys. J.*, **306**, 248.

Tuohy, I. R., Lamb, F. K., Garmire, G. P. & Mason, K. O., 1978, *Astrophys. J.*, **226**, L17.

Tuohy, I. R., Mason, K. O., Garmire, G. P. & Lamb, F. K., 1981, *Astrophys. J.*, **245**, 183.

Tuohy, I. R., Ferrario, L., Wickramasinghe, D. T. & Hawkins, M. R. S., 1987, *Proc. Astr. Soc. Australia*, **7**, 60.

Turner, M. J. L. *et al.* 1989, *Publ. Astr. Soc. Japan*, **41**, 345.

van Gent, H., 1931, *Bull. astr. Neth.*, **6**, 93.

Visvanathan, N. & Wickramasinghe, D. T., 1979, *Nature*, **281**, 47.

Wade, R. A., 1982, *Astron. J.*, **87**, 1558.

Walker, M. F., 1956, *Astrophys. J.*, **123**, 68.

Warner, B., 1987, *Mon. Not. Roy. Astr. Soc.*, **227**, 23.

Warner, B. & Cropper, M., 1984, *Mon. Not. Roy. Astr. Soc.*, **206**, 261.

Warner, B. & O'Doroghue, D., 1980, *IAU Circ.*, No.3252.

Watson, M. G., 1986, In *Physics of Accretion onto Compact Objects*, p97, ed. Mason, K. O., Watson, M. G. & White, N. E., Springer-Verlag.

White, N. E., 1981, *Astrophys. J.*, **244**, L85.

Wickramasinghe, D. T. & Meggitt, S. M. A., 1982, *Mon. Not. Roy. Astr. Soc.*, **198**, 975.

Wickramasinghe, D. T., Visvanathan, N. & Tuohy, I. R., 1984, *Astrophys. J.*, **286**, 328.

Wickramasinghe, D. T., Martin, B., 1985, *Mon. Not. Roy. Astr. Soc.*, **212**, 353.

Young, P. & Schneider, D. P. 1981, *Astrophys. J.*, **247**, 960.